Lidar Calibration

by

Shuki Chaw

A dissertation submitted to the Graduate Faculty in Electrical Engineering in partial fulfillment of the requirements for the degree of Doctor of Philosophy,

The City University of New York

2009

This manuscript has been read and accepted for the
Graduate Faculty in Engineering in satisfaction of the
dissertation requirement for the degree of Doctor of Philosophy.

Barry M. Gross

Date _____ _____
Chair of Examining Committee

Mumtaz K. Kassir

Date _____ _____
Executive Officer

Fred Moshary

Samir Ahmed

Yonghua Wu

Dimitrios Kokkinos

Supervisory Committee

THE CITY UNIVERSITY OF NEW YORK

Abstract

Lidar Calibration

by

Shuki Chaw

Advisers: Professor Barry Gross and Professor Fred Moshary

Owing to its inherent low gain detection of the $1064nm$ channel and a negligible molecular return from the atmosphere, a boundary condition for the retrieval of optical data by inversion cannot be assumed with high confidence as for the other channels in the multiwavelength Mie lidar. It is therefore necessary to evaluate the calibration constant for the $1064nm$ channel. Two methods of calibration are studied and compared. One method is calibration by high or low clouds. The other method is calibration by a ceilometer which is itself calibrated and co-located at the lidar site. The results are compared with the aerosol optical depth measured by a calibrated sun photometer co-located at the same site as part of the AERONET network at CCNY. In the latter method, all three instruments are located at the same site, there is no issue of atmospheric differences when comparing data but it makes calibration dependent on that of other instruments. Clouds are a natural and frequent occurrence but the lidar system may change between cloud appearances. Both methods have their merits and shortcomings.

To My Parents

Acknowledgements

I feel at times honored by my mentor, Professor Gross who expected of me competence and self direction, who at other times, not necessarily made me feel good about myself or told me that I could do anything I wanted to do. Sometimes the best mentors provide tough love by being critical as a means of teaching.

I am indebted to Professor Moshary for his encouragement and confidence in me.

I should thank Dr. Wu for making many efforts to proctor my progress in research without compromising my interests while being gracious throughout, which makes me feel undeserved.

I would like to thank Dr. Kokkinos for his participation and feedback, all the remote sensing instructors for taking my questions seriously and my peers for their collaboration and the times happily spent together.

I wish to thank Professor Ahmed, my mentors, NOAA and its administrators for the funded opportunity to complete my program.

A word of appreciation for my wife Tina who has remarkable patience for me.

CONTENTS

CHAPTER 3

Multiwavelength lidars and retrievals

CHAPTER 4

Retrieval of cloud optical depth with a Mie-Raman lidar

CHAPTER 5

The 1064*nm* channel and cloud properties

CHAPTER 6

Calibration of the 1064-nm channel using clouds and the ceilometer

LIST OF TABLES

LIST OF FIGURES

1.1 Radiation budget balance

Of all the solar radiation that reaches the earth, approximately 19% is directly absorbed by clouds and the atmosphere, 51% by the surface and 30% is reflected back to space. About 50% of the spectral energy lies in wavelengths longer than the visible, 10% in the shorter region and 40% in the visible window i.e. 0.4*nm* and 0.7*nm* These amounts are estimated by the Stefan -Boltzmann Law for the blackbody irradiance. The shortwave radiation from the sun fuels the earth by absorption while the reemitted longer infrared radiation from the surface and atmosphere exhausts the fuel.

The net radiation varies by 6% between January to July because of its elliptical orbit round the sun and must be zero for the entire year in order that long term climate change does not occur [2].

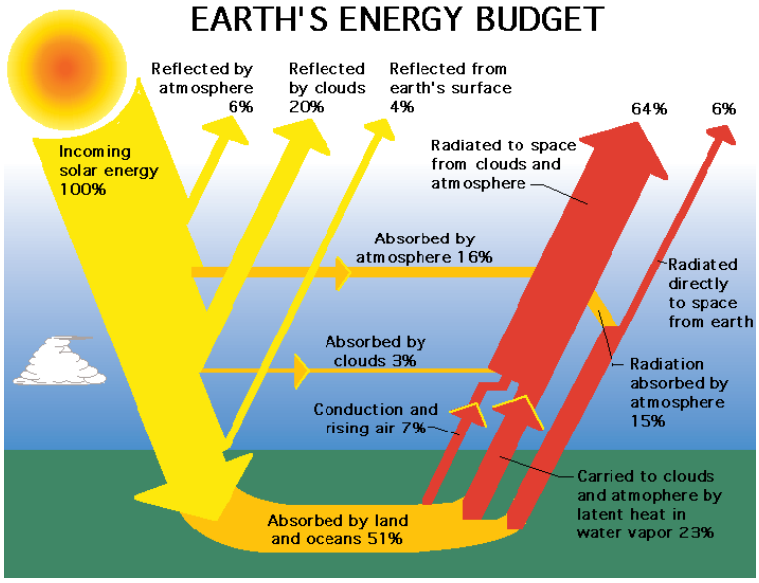

Figure 1.1: Radiation budget [1]

1.2 Aerosols

As a direct effect, aerosols absorb, reflect and scatter sunlight back to space. As an indirect effect, aerosols in the lower atmosphere influence microphysical properties, such as the critical radius at which a cloud-droplet is formed, nucleation rate, and hence the formation and lifetime of clouds. Given the same amount of water content available in the atmosphere as aerosols concentration increases, it will condense on the increased number of cloud condensation nuclei (CCN), smaller droplets will form and delayed precipitation will occur. This has an impact on cloud formation and rainfall patterns.

Reflection of solar radiation back to space cools the planet and trapping of longer reemitted radiation by clouds warms it. Clouds cool the earth by reflecting direct sunlight back to space and warms it by absorbing and reemitting thermal radiation from the surface and lower part of the atmosphere. These two competing effects make prediction of the impact of cloud on the temperature in Earth's climate system difficult. Aerosols are one of the greatest sources of uncertainty in climate modeling. Size and concentration distributions vary in time and space which lead to variations in the cloud microphysical properties that in turn have an impact on the radiative properties of cloud and climate. The physical and chemical makeup of aerosol, its concentration and size, distribution locations in the atmosphere all seem to affect the Earth's energy budget.

Various kinds of aerosol can have a significant effect on the radiative balance of the earth-atmosphere system and on the earth's climate because of their global presence. For example, sulphate aerosols are small and have a longer lifetime in the atmosphere.

They are also hygroscopic so they grow large and increase the optical depth to sunlight penetration.

Increasing concerns that aerosols of anthropogenic origins may have caused worldwide weather disturbances have prompted intensified observation and daily recording of concentrations at ground as well as in space. One of the most successful lidar experiments to retrieve global atmospheric aerosol and cloud properties was LITE flown on the space shuttle in 1994. Numerous researchers find themselves in the forefront of determining the optical properties of aerosols and their size distribution of late.

1.3 Aerosols classification and formation

Aerosols are first classified by size into the nuclei mode or Aitken particles with radius $r < 0.1\mu m$. Particles with dry radii $0.1\mu m < r < 1\mu m$ belong to the accumulation mode, and those with $r > 1\mu m$ are in the coarse mode. Dry radii are specified because some aerosols are hygroscopic in nature, absorbing water from their vicinity and grow in size, while its variance remains constant, dependent only on a source mechanism [3]. At the small end of this range, the number is limited by coagulation, and at the large end gravitational sedimentation.

Particles are injected into the atmosphere by man-made activities or from natural sources such as volcanic activities, evaporations in the sea leaving salt particles carried upwards by wind or air currents, dusts blown from desert storms etc. It is estimated that most of the total particle mass is contained in the lowest kilometer of the atmosphere. Concentrations vary greatly with locations due to airmass movements created by various mechanisms, convection, advection, turbulence, diffusions, gravity and other removal

mechanisms. The removal rate of aerosol particles by self-coagulation is proportional to the square of the particle concentration, while the removal by interaction with cloud drops and raindrops is proportional to the first power of the particle concentration [4]. There are three major mechanisms from which terrestrial aerosols are formed, gas to particle (GTP), drop to particle conversion (DPC), and bulk to particle conversion (BPC).

I. Gas to particle (GTP)

There are three ways for the GTP conversion to take place:

i. Homogeneous nucleation in supersaturated vapors with low boiling point temperatures. Examples are substances in combustion products and volcanic plumes, sulphates, carbonates, resins, oil, soot and tars. There sizes are usually small.

ii. Chemical reaction in the gas phase [4],

$$SO_2 + OH \rightarrow HOSO_2$$

(sulfur dioxide adduct $HOSO_2$ as intermediate product)

$$HOSO_2 + O_2 \rightarrow SO_3 + NO_3$$

For example, sulfur dioxide gas combines with the radical OH in the atmosphere to produce sulfate SO_3 aerosol particle.

iii. Growths of the gas vapor to the pre-existing aerosol particles. They involve dissolved species in the particle, vapor diffusion and adsorption on the surface.

II. Drop to particle conversion (DPC)

Most gases are to certain degree soluble in water. They enter the cloud and rain drops by diffusion and crystallized to form a solid mass when the drops evaporate, which has different chemical and physical characteristics than before they entered the drops. The condensation nucleus left behind may be considerably larger than it was before evaporation. This process is called cloud processing. The nucleus that has undergone the hygroscopic growth does not normally return to its previous dry state at the same relative humidity at which the nucleus was dissolved i.e. deliquescence and crystallization occur at different percentages of relative humidity, a hysteresis phenomenon. Cloud processing affects accumulation mode particles more than the larger ones due to their hygroscopic nature.

III. Bulk to particle conversion (BPC)

Through weathering rocks and minerals are broken up into smaller particles and became airborne especially during a dust storm. It is already known that they can get transported even over the oceans. Once becoming airborne, the loose silicate particles readily coagulate with other aerosol particles with mixed compositions, often with considerable amount of organic material attached from decayed plants for instance. Over the sea surface, BPC occurs thorough spray drops caused by waves. The finer drops and mists become airborne and evaporate to form aerosol particles. Bursting of bubbles at the wave crests is another important mechanism through which sea salt particles are converted into aerosol particles.

This classical view of the formation of aerosol particles in the atmosphere can be represented by the mass distribution diagram from Whitby and Cantrell, 1976.

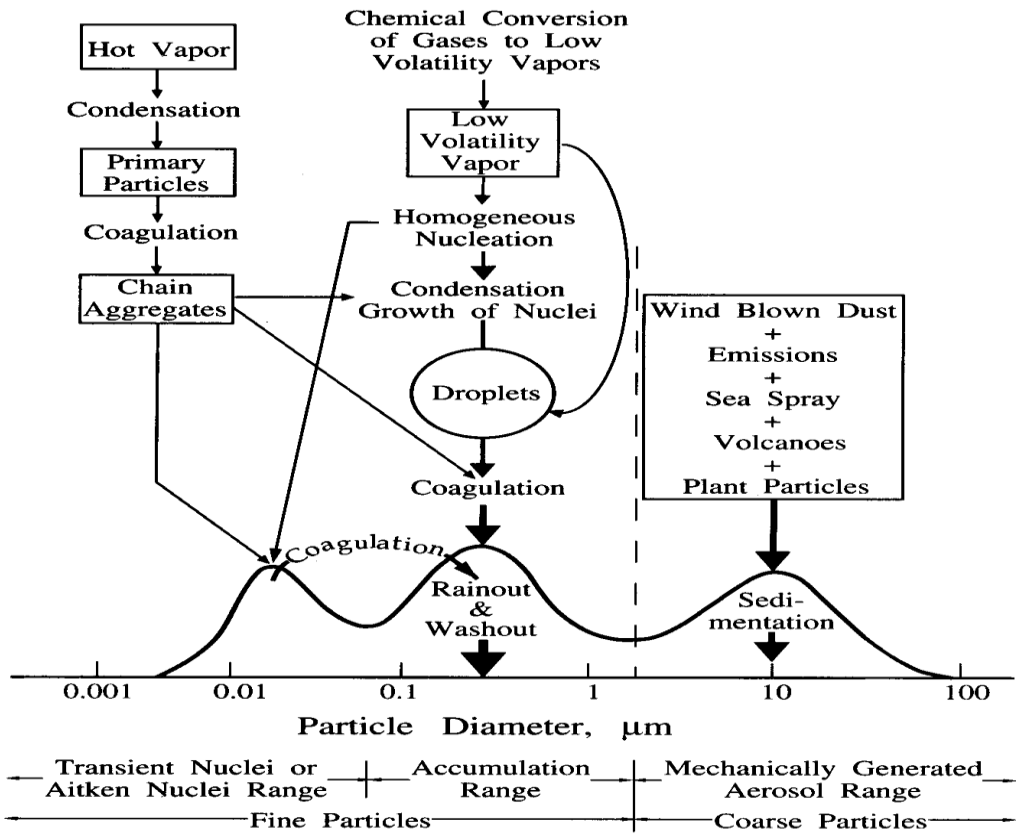

Figure 1.2: Formation of aerosols [7]

Nucleation occurs when water vapor condenses. It can occur with or without the presence of foreign material. Drops do form from water vapor alone under supersaturated but finite vapor pressure. This experimental observation is contrary to Kelvin equation which demonstrates that the saturation vapor pressure over the surface of a water drop is larger than that of a flat surface, and increasing so with a decreasing radius of the drop at a given temperature in thermodynamic equilibrium with its environment.

Kelvin Equation: $$\frac{e_a}{e_{sat}} = \exp\left(\frac{2M\sigma}{\Re T \rho a}\right) \qquad \text{Eq.(1.1)}$$

M -- the molecular weight of water

σ --surface tension on the drop

$\Re$ --universal gas constant

T --temperature

ρ --water density

a --radius of drop

The Kelvin equation indicates that the vapor pressure required to hold a microscopic sized drop in equilibrium is prohibitively large. The reason for this contradictive behavior with experience is that the homogeneous phase change does not begin in a continuous manner in practice but spontaneously as a result of fluctuations in space and time of the density and temperature in the original metastable phase. Within this phase of water vapor are small molecular clusters that grow to be embryos and at a critical vapor pressure reach a critical germ size. Nevertheless, homogeneous nucleation of water vapor only occurs in the laboratory and at a supersaturation of several hundred percent.

However, this observation in the laboratory still contradicts with that in the atmosphere where supersaturations are as low as a few or even one percent. In the presence of aerosols in the atmosphere, a change of phase is initiated by the particles acting as cloud condensation nuclei (CCN) at the these very low supersaturations. Heterogeneous nucleation has taken place.

1.4 Health impacts of aerosols

Aerosol particulates present Health hazards to us. The two principal components of the atmosphere that have been singled out as major concerns of air pollution are ozone and airborne particulate matter (PM). Ozone is a known toxic species that causes deleterious respiratory effects, particularly causing blisters in the respiratory tract, ageing of tissue and complications for older individuals and those with asthma and other respiratory problems [5]. Under the Clean Air Act in 1997, the EPA issues a new set of National Ambient Air Quality standards for fine particulate matter with a diameter less than 2.5 microns, together with ozone, they make up the most significant contribution to regional haze. The EPA routinely measures their ground levels. Pollution caused by aerosol is called particle pollution by the EPA.

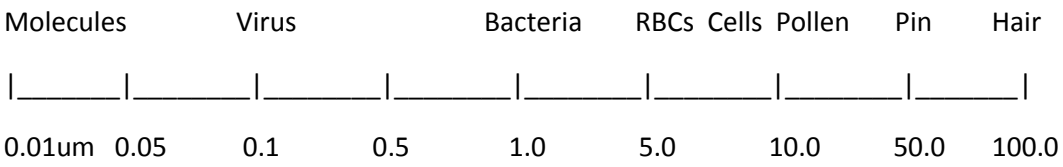

Figure 1.3: Particulates Sizes

Particulate matter consists of solid particles and liquid droplets. They come in various shapes and sizes and chemical compositions and are known as primary particles when they are emitted directly from sources such as unpaved earth surfaces and fires. There are sources where these fine particles are formed in complicated chemical reactions with sulfur dioxides and nitrogen dioxides emitted from power plants and automobile

vehicles. The latter is the major source of fine particle pollution in the country [12]. Particulate pollutants with diameters smaller than 2.5 micrometers are inhalable fine particles. They can lodge deeply into the lungs because of their small sizes which are only visible with the aid of an electron microscope. $PM_{2.5}$ lingers after weather driven events and becomes a serious concern for chronic asthma and other respiratory conditions [6]. PM_{10} settles out of the atmosphere quicker and is a better indicator of atmospheric dust events. PM_{10} deposits in the thoracic region and is often a concern for silicosis.

1.5 Health standards of $PM_{2.5}$

The bar graph below shows state-level emissions in New York grouped by major source sectors [13].

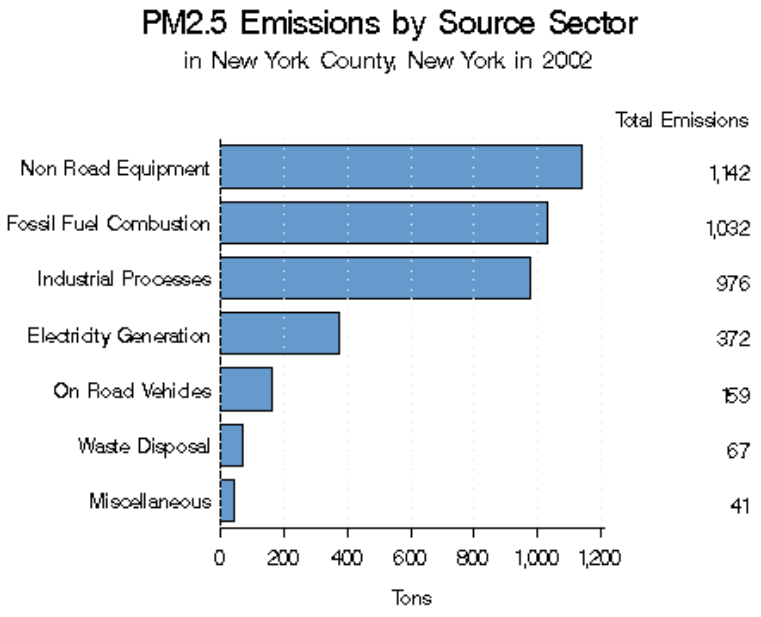

Figure 1.4: Emission sources of $PM_{2.5}$ in New York State, 2002

The Clean Air Act established two types of standards. The primary standards were established to protect public health which includes the sensitive populations such as asthmatics, children and elderly. The secondary standards were established to protect public welfare which sets limits to protect crops and buildings etc. Before the distinction of fine particles $PM_{2.5}$ was made, the nation's air quality was regulated by standards established in 1987 regarding PM_{10} , more than ten years after standards for particulate matter were first established in 1971. Ten years after the distinction of $PM_{2.5}$ was made, separate and more stringent standards were introduced in 1997 due to its links to serious health problems ranging from hospital admissions and emergency room visits to premature deaths for people who have heart and lungs diseases [8]. The table sums up current regulatory standards for particulate matter.

	Primary Standards	Averaging Times	Secondary Standards
$PM_{2.5}$	15.0 $\mu g/m^3$	Annual 3-year average of the weighted annual arithmetic mean	Same as Primary
	35 $\mu g/m^3$	24-hour 3-year average of the 98th percentile of 24-hour concentrations	
PM_{10}	Revoked	Annual (Revoked: lack of evidence linking health problems to long-term exposure)	
	150 $\mu g/m^3$	24-hour Not to be exceeded more than once per year on average over a period of 3 years	

Table 1.1: Current PM compliant standards since 2006 [9]

Instead of the particles concentration, an air quality index (AQI) is created for the public as an indicator of air quality. An AQI of 100 for particles up to 2.5 micrometers in diameter corresponds to a level of 40 micrograms per cubic meter, averaged over 24 hours [11]. An AQI of 100 for particles up to 10 micrometers in diameter corresponds to a level of 150 micrograms per cubic meter (averaged over 24 hours) [11].

Healthy threshold of the AQI borders at 100 and reaches 500 as maximum for extreme pollutions. For the precise indications of the AQI, it is best referred to the description given by the standards maker.

"AQI focuses on health effects one may experience within a few hours or days after breathing polluted air. An AQI value of 100 generally corresponds to the national air quality standard for the pollutant, which is the level EPA has set to protect public health. AQI values below 100 are generally thought of as satisfactory. When AQI values are above 100, air quality is considered to be unhealthy, at first for certain sensitive groups of people, then for everyone as AQI values get higher [11]."

The table below given by the EPA indicates various levels of health concern and their implications [11]. The levels are color coded for easy visualization on maps.

Air Quality Index (AQI): Particle Pollution

Index Values	Levels of Health Concern	Cautionary Statements
0-50 (Green)	Good	None
51-100 (Yellow)	Moderate	Unusually sensitive people should consider reducing prolonged or heavy exertion.
101-150 (Orange)	Unhealthy for Sensitive Groups	People with heart or lung disease, older adults, and children should reduce prolonged or heavy exertion.
151-200 (Red)	Unhealthy	People with heart or lung disease, older adults, and children should avoid prolonged or heavy exertion. Everyone else should reduce prolonged or heavy exertion
201-300 (Magenta)	Very Unhealthy	People with heart or lung disease, older adults, and children should avoid all physical activity outdoors. Everyone else should avoid prolonged or heavy exertion.
301-500 (Burgundy)	Hazardous	People with heart or lung disease, older adults, and children should remain indoors and keep activity levels low. Everyone else should avoid all physical activity outdoors.

Table 1.2: Air quality index (AQI) and levels of health concern

The map below shows that $PM_{2.5}$ pollution in New York City has reached an unhealthy level which corresponds to non compliance of the more than 40 micrograms of $PM_{2.5}$ in a cubic meter of air [16]. The orange color alert advises people with heart or lung disease, older adults, and children should reduce prolonged or heavy exertion.

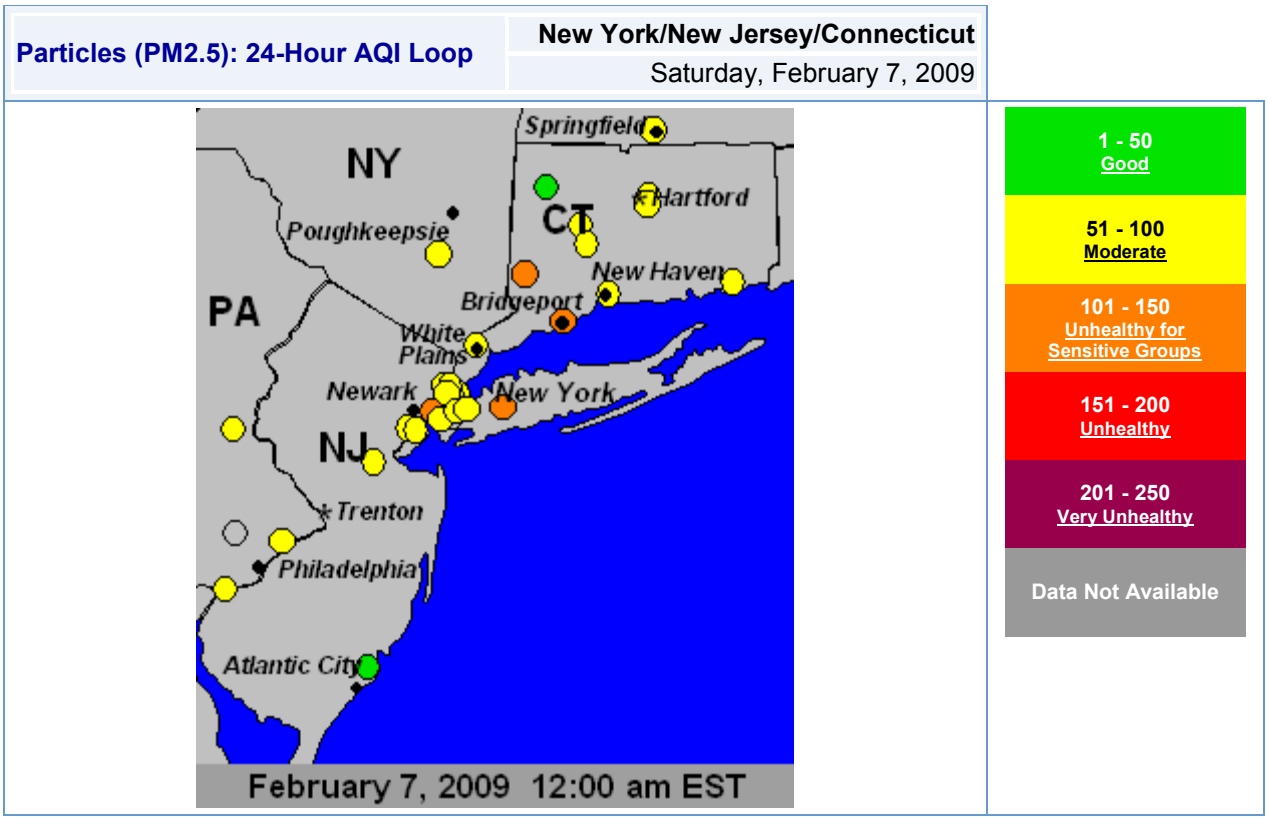

Figure 1.5: Air quality alert in New York City as opposed to the surrounding areas

The Clean Air Act requires every state to establish a network of air monitoring stations for criteria pollutants. A geographic area that meets or does better than the national ambient air quality standard is called an attainment area, an area that doesn't meet this standard is called a nonattainment area. By 2010, the EPA will have made its final designations of which areas of the country are in attainment and which are not. States would then begin the formulation of their state implementation plans, and have

until 2015 to bring their $PM_{2.5}$ concentrations into compliance with the new standard [20].

Apart from their sparsity, ground monitors are not without their problems. There are significant difficulties associated with verifying $PM_{2.5}$ forecasts, operational and instruments related. The filter-based FRM, Federal Reference Monitor collects particles over a 24-hour period. The filter is sent to an ultra-clean laboratory for weighing with final results available weeks to months after observation. Error is expected with volatile particles deposited on the filter during the sampling period. Difference in sampling frequency across the network of monitors introduces differences in the observed daily maximum $PM_{2.5}$ concentrations. The continuous $PM_{2.5}$ monitors use different analytical techniques to measure $PM_{2.5}$. This makes comparison of FRM and continuous monitors result interpretations complicated. Statistical models are required to make predictions and are "trained" on historical $PM_{2.5}$ and meteorological data. Because $PM_{2.5}$ is made up of a variety of constituents that vary by season, models must be season specific [19].

Much optimism has been placed on correlating the concentrations of $PM_{2.5}$ on the ground with the aerosol optical depth (AOD) derived from various satellite retrievals. AOD provides a direct measurement of fine PM loading over an area rather than a surrogate of emission sources. Daily correlations between AOD and $PM_{2.5}$ over time at fixed locations are reasonably high in the eastern United States except in winter [17]. This must occur when most sources are local. Empirical relationships between ground measurements and AOD can vary regionally according to the sources and compositions of aerosol. The relationship between AOD and $PM_{2.5}$ concentrations needs to be

established in order to use AOD to predict air quality. This requires intensive air pollution monitoring field campaign [21]. Improved AOD does not necessarily improve predictions of surface $PM_{2.5}$ [18], for instance, from optimal integration of retrievals from MODIS and MISR. However, improvements in the relationship was found when vertical mismatch based on vertical profile information was adjusted, not surprisingly, because it depends on the aerosol vertical profile and composition. Quantitative use of the relationship between $PM_{2.5}$ and AOD requires a stable vertical distribution of aerosol residing in the PBL, for instance [18]. A lidar profile of the vertical distribution will certainly enhance predictions of $PM_{2.5}$

REFERENCES

[1] NASA Facts, "The Balance of Power in the Earth-Sun System.", FS-2005-9-074-GSFC, 2005

[2] Paul Menzel, Lectures at CREST, Remote Sensing, March 2006

[3] Hans R. Pruppacher, James D. Klett, "Microphysics of Clouds and Precipitation.", Kluwer Academic Publishers, 1997

[4] K. Parameswaran, K. 0. Rose, and B. V. Krishna Murthy, "Relationship between backscattering and extinction coefficients of aerosols with application to turbid atmosphere.", Vol. 30, No. 21, *Applied Optics*, 3059-3071, 1991

[5] C. Russell Philbrick and Karoline R. Mulik, "Application of Raman Lidar to Air Quality Measurements.", Penn State University, Department of Electrical Engineering, University Park PA 16802

[6] Stanley Marain and William Sprigg, "Verification and Validation Report 2007 on Public Health Applications in Remote Sensing 2007.", 2007

[7] Whitby and Cantrell, 1976, http://cloudbase.phy.umist.ac.uk/people/dorsey/Aero.htm

[8] http://www.epa.gov/pmdesignations/2006standards.htm

[9] http://www.epa.gov/pm/standards.html

[10] Paul T Wentworth," Clean Air Fine Particle Implementation Rule for the 1997 PM2.5 Standards. ", P.A., EPA Region 3, 2007

[11] http://www.airnow.gov/index.cfm?action=aqibroch.aqi#aqipar

[12] http://www.epa.gov/air/particles/basic.html

[13] http://www.epa.gov/ttn/naaqs/pm/pm25_index.html

[14] http://www.epa.gov/air/emissions/pm.htm

[15] http://www.fhwa.dot.gov/environment/conformity/nonatain

[16] http://www.airnow.gov/index.cfm?action=airnow.archivescalendar

[17] Christopher J. Paciorek1 and Yang Liu,"Limitations of Remotely Sensed Aerosol as a Spatial Proxy for Fine Particulate Matter.", *Environmental Health Perspectives*, Vol.117, No.6, 2009

[18] http://www.climatescience.gov/workshop2005/posters/P-AQ1.2_Chin.pdf

[19] William F. Ryan ,"$PM_{2.5}$ Forecasting for the Philadelphia Metropolitan Area 2003-2007",Department of Meteorology The Pennsylvania State University, 2007

[20] http://www.mercatus.org/PublicationDetails.aspx?id=21216

[21] http://www.uiowa.edu/~geog/faculty/kumar/AirQualityData.shtml

2.1 Sun photometer

The sun photometer is an instrument that detects direct transmitted sunlight to infer the atmospheric turbidity. Aerosols do not only scatter but also absorb selectively incoming sun radiation. Aerosol optical depth is derived from solar intensity directly measured on the ground. The higher the number is, the more turbid is the air. It accurately infers the turbidity of air regardless of the daily variations of water vapor in the atmosphere because absorption by water vapor in these wavelengths of the visible spectrum can be neglected [5]. Ozone absorption is also small here.

From the Beer-Bouguer-Lambert law, the solar intensity measured at the ground is

$$I(\lambda) = \left(\frac{r_0}{r}\right)^2 I_0(\lambda) \exp\left[-\tau_{total}(\lambda) m(\theta_0)\right] \qquad (2.1)$$

r and $r_0 (\approx 1.5 \times 10^{11}\, m)$ are the actual and mean sun-earth distances, respectively.

$I_0 (\approx 1380\ Wm^{-2})$ is the known solar intensity at top of atmosphere (TOP) corresponding to r_0

θ_0 is the solar zenith angle.

$m(\theta_0) = 1/\cos\theta_0$ is the air mass factor traversed by the sun beam.

Solving for $\tau(\lambda) = \tau_{total}(\lambda) - \tau_R(\lambda)$, the aerosol components,

$$\tau(\lambda) = \frac{1}{m(\theta_0)} \left\{ \ln \left[I_0 \left(\frac{r_0}{r} \right)^2 \right] - \ln I(\lambda) \right\} - \tau_R(\lambda) \tag{2.2}$$

The molecular component $\tau_R(\lambda)$ can be calculated to accuracy on the order of 0.5%

$\left(\frac{r_0}{r} \right) I_0(\lambda)$ can be evaluated from the Langley plot as the intercept or from the known solar spectral data taking the celestial geometry into consideration.

In addition to the optical depth of aerosols, size distribution can also be retrieved. To facilitate remote sensing of aerosols, a number of analytical expressions have been developed to model their size distributions. The widely used ones are the log-normal, gamma distributions and Junge power law.

The aerosol optical depth for the air column can be expressed in terms of the extinction coefficient,

$$\tau(\lambda) = \int_0^\infty \beta(\lambda, z)\, dz \tag{2.3}$$

The extinction coefficient in turn can be expressed in terms of the extinction efficiency or cross section for an individual particle, $\sigma(a, \lambda) = \pi a^2 Q_{ext}(2\pi a / \lambda, m)$ and $x = (\lambda a / 2\pi)$

$$\beta(\lambda, z) = \int_0^\infty \sigma(a, \lambda)\, n(z, a)\, da \tag{2.4}$$

With the Jung distribution, $n(z,a) = C\,a^{-(\nu+1)}$, C is a scaling constant directly proportional to the concentration, ν is a shaping factor between 2 and 4, $n(z,a)$ has a unit of $[cm^{-3}\ \mu m^{-1}]$, the optical thickness can be expressed in terms of these parameters,

$$\tau(\lambda) = \int_0^{\infty} \pi(\lambda/2\pi)^2 x^2 Q_{ext}(x,m) C(\lambda/2\pi)^{-\nu-1} (x)^{-\nu-1} (\lambda/2\pi) dx$$

$$\tau(\lambda) = C\pi(\lambda/2\pi)^{-\nu+2} \int_0^{\infty} Q_{ext}(x,m) C(x)^{-\nu+1} dx \tag{2.5}$$

For non-absorbing particles and $2 < \nu < 6$, the integral converges to a constant [9].

Comparing the wavelength dependence of the optical depth with Angstrom exponent k for the particles, $\tau(\lambda) = const \times (\lambda)^{-k}$ (2.6)

$$\Rightarrow \ \nu = k + 2 \tag{2.7}$$

That is to say that with an assumed size distribution, a knowledge of the Angstrom exponents can determine the number of particles per unit area per unit radius interval in a vertical column of the atmosphere i.e. the actual size distribution assumed to take the general form of the power law.

The actually lower integration limit of the integration is not zero but defined by the radius down to which the optical interaction with the particle is still efficient. For measurement wavelengths longer than $355nm$, the minimum particle size is around $50nm$. The upper limit is finite and set by the concentrations that are too low for particles

to have any significant contribution to the signal. For typical particle size distributions in the troposphere, this upper limit is below $10\mu m$ [8].

Size distributions determined from extinction spectra are not unique. It depends of the range of radii used in the integration, the initial guess of the distribution and number of iterations [9].

The sun photometer is one of those radiometers that operate on transmitted sunlight. The principle of sensing has just been quantitatively outlined. It is seen that these ground based radiometers only deliver column integrated quantities without distinction of vertical layers of particulates.

Figure 2.1: Automatic Sun Tracking Photometer CE 318

2.1.1 Principles of operation [15]

The quantities that can be measured in a cloudless sky by the use of solar radiation as a source are the direct radiation flux and the diffuse intensity as a function of wavelengths. The approach of the CIMEL sun photometer is to acquire aureole and sky radiance observations with a large range of scattering angles from the sun through a constant aerosol profile to retrieve size distribution, phase function and aerosol optical depth.

For the direct sun measurements, the CIMEL uses the sun collimator with a field of view (FOV) of 1.2 degrees and aims at the sun to make extinction measurements in eight spectral bands selected by interference filters at wavelengths of 340, 380, 440, 500, 670, 870, 940 and 1020 nm, taking approximately 10 seconds. The 940 nm channel is used for column water abundance determination. Optical depth is calculated from spectral extinction of direct beam radiation at each wavelength based on the Beer-Bouguer Law. The instrument starts to operate at an air mass of 7 in the morning and ends at an air mass of 7 in the evening. Attenuation due to Rayleigh scattering, absorption by ozone, and gaseous pollutants is estimated and removed to isolate the aerosol optical depth (AOD). A sequence of three such measurements are taken 30 seconds apart creating a triplet observation per wavelength. The observable variation in a triplet is used to identify clouds in many cases from the usual larger time variation of clouds being greater than that of aerosols.

The sky radiance is acquired in four spectral bands , 440, 670, 870 and 1020 nm along the solar principal plane (PPL) up to nine times a day and along the solar

almucantar (ALM) up to six times a day at an optical air mass of 4, 3, 2 and 1.7 both morning and afternoon. The wavelengths are carefully selected outside the gas absorption bands in order to reduce the radiative transfer problem to a purely scattering problem [14].

For the ALM measurements, the CIMEL aims at the sun at constant elevation while varying the azimuthal angle using its sky collimator also with a FOV of 1.2 degrees, tracing out a conical surface. For the PPL measurements, the CIMEL aims at the sun and makes measurements in the vertical plane containing the sun, each angular distance from the sun equals the scattering angle regardless of the solar zenith angle. For the almucantar geometry, the scattering angle is related to the solar zenith angle and the azimuthal angle relative to the sun by $\cos\Theta = \cos^2\theta_0 + \sin^2\theta_0 \cos\phi$ [19]

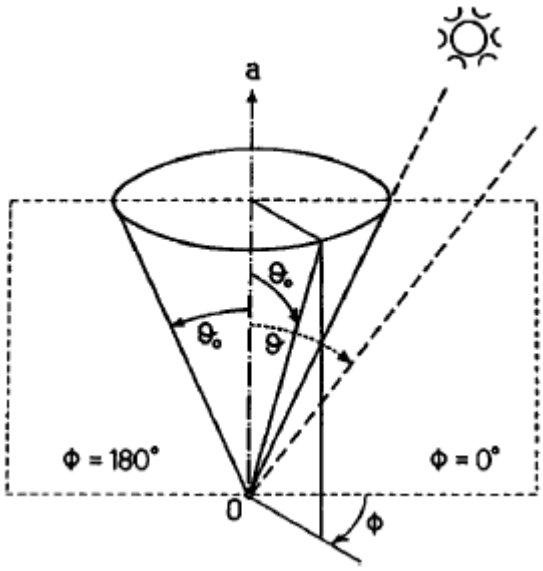

Figure 2.2: Geometry concerning the measurement of the intensity in solar almucantar and in the principal plane. Observer is at the origin.

Optical thickness in different wavelengths are measured by direct sun radiance. The direct flux $F = F_0 \exp(-\mu\tau)$ in $[Wm^{-2}\mu m^{-1}]$ where F_0 is the flux at upper atmosphere and μ is the optical air mass. The diffuse intensity is determined through the radiative transfer equation as follows [19],

$$E(\theta,\phi) = E(\Theta) = \mu\omega\tau P(\Theta) F \Delta\Omega + q(\Theta)$$

where ω is the single scattering albedo of the whole air mass, $P(\Theta)$ is the phase function, $\Delta\Omega$ is the solid view angle of the instrument and $q(\Theta)$ is the multiple scattering contribution.

The diffusely scattered radiance in solar almucantar is measured. For at least the single-scattering approximation, sky radiances in the almucantar are not sensitive to aerosol vertical variations. Vertical distribution of aerosol is assumed homogeneous in the almucantar inversion. From the calibrated radiances that vary with the azimuthal angles, the phase function is obtained. From simulated or measured direct flux and diffuse intensity, features other than the phase function can be retrieved. Sky radiance measurements are inverted with the Dubovik [16] and Nakajima inversions to provide aerosol properties of size distribution and phase function over the particle size range of 0.1 to 5 um. These properties are provided in total atmospheric column.

2.1.2 AERONET

The AERONET (**AE**rosol **RO**botic **NET**work) program is a federation of ground-based remote sensing aerosol networks established by NASA and PHOTONS (Univ. of

Lille 1, CNES, and CNRS-INSU) with numerous data products [26]. There are radiance products, synergy and climatology data. Derived inversion products include aerosol size distribution, complex index of refraction, volume and effective radius, absorption and extinction aerosol optical depth, single scattering albedo, asymmetry factor, phase functions, radiative forcing, spectral flux. The most important product for the lidar application is the optical depth measurement without which the lidar data inversion cannot be assured. The Angstrom coefficient is also evoked for an empirical determination of the scatterers size. Below are displays of optical depth. The error bars are calculated from the data triplet with each component acquired by the instrument once every 30 seconds, they become noticeable during cloud intervals due to its larger time variations than aerosols.

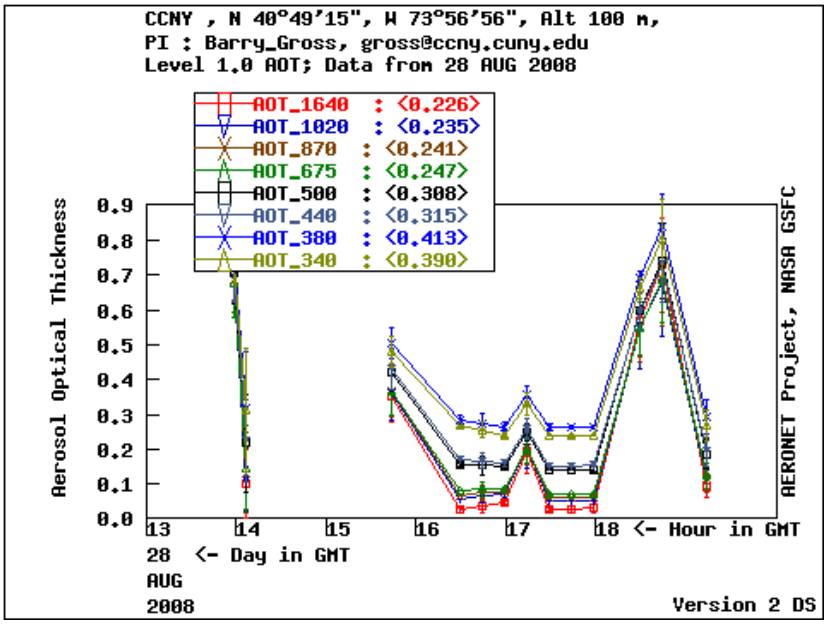

Figure 2.3: Unscreened AOD. Cloud appears just after 17hr

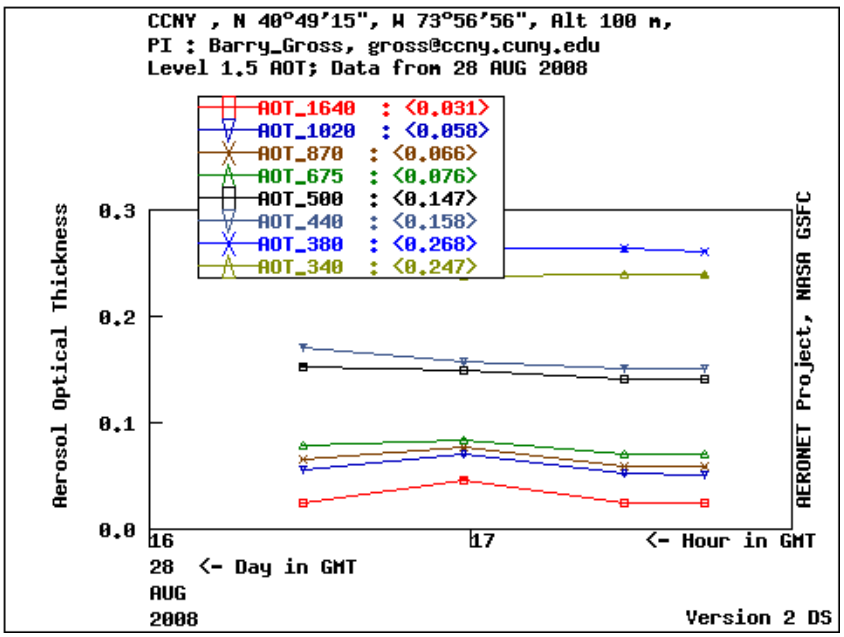

Figure 2.4: Cloud screened AOD. Cloud AOD just after 17hr has been screened out by the data triplet variation algorithm [18].

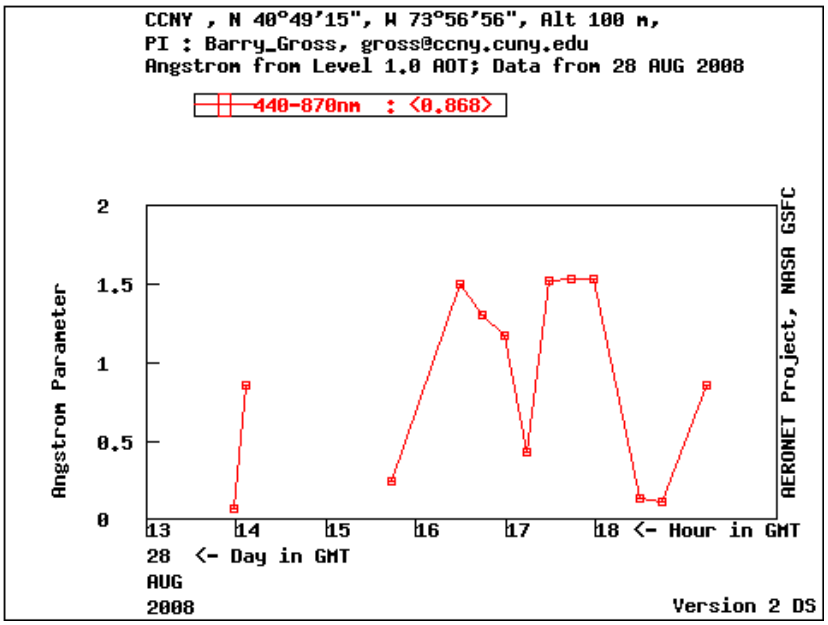

Figure 2.5: Angstrom coefficients plotted between 9 am to 3:30pm local time. Cloud intervals: 10:00am (14:00hr),11:30am (15:30hr),1:15pm(17:15hr) and 2:30pm (18:30hr)

The plot above shows how the Angstrom coefficients behave in the presence of cloud. Since cloud particles are large scatters, they have negligible size dependence and assume a zero coefficient. Angstrom coefficients are close to zero at 10am, 11:30am, 1:15pm and 2:30pm and are also identified on the following range scaled power lidar image coinciding with appearance of clouds.

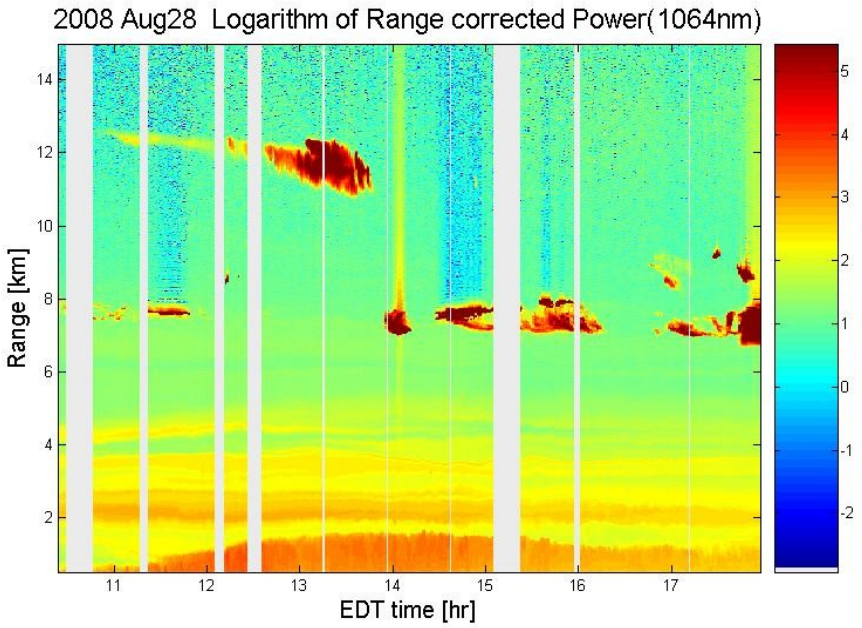

Figure 2.6: Lidar image, clouds occur at 11:30am, 1:15pm and 2:30pm at the minima of the Angstrom coefficients plot

2.1.3 Air quality

Regional air quality is dependent on the transport and mixing of trace gases and aerosol particles. It is generally accepted that major impact on local air quality is made by atmospheric transport, and it is well known that transport mainly occurs at elevated layers [23]. These processes occur on a variety of spatial scales, regional, continental and in the

atmospheric boundary layer. A clear understanding of transport on these scales will allow us to assess the air quality as they are impacted from local, regional, and distant sources. The sources, sinks, distribution and processes of aerosol particles all play a role in the regional air quality.

Better environmental assessments of air quality and long-range transport of pollution depends on the knowledge of the vertical distribution of aerosols as significant long-range transport occurs at elevated layers and precise arrival heights are needed to trace substances back to the source [23].

Model evaluation studies for aerosols are severely limited by a lack of data both aloft and at the surface. For instance, in order to reliably estimate $PM_{2.5}$ from optical depth, vertical structure of aerosol is necessary [22]. In order to improve regional forecast of air quality, a knowledge of the vertical distribution of pollutants is essential for understanding the transport at elevated heights and the process of down mixing into the planetary boundary layer (PBL) [23].

Air and space borne lidars can provide important information on the vertical and horizontal distribution of pollutants for forecast and model verification. On the regional scale, observations are already compared with air quality models [20].

Some of the essential questions to answer are [21]:

Under what conditions does local urban pollution have a significant impact on other areas in the region?

How do the heating and cooling cycle at the earth's surface affect horizontal transport?

How effective are transport and vertical mixing in dispersing pollution?

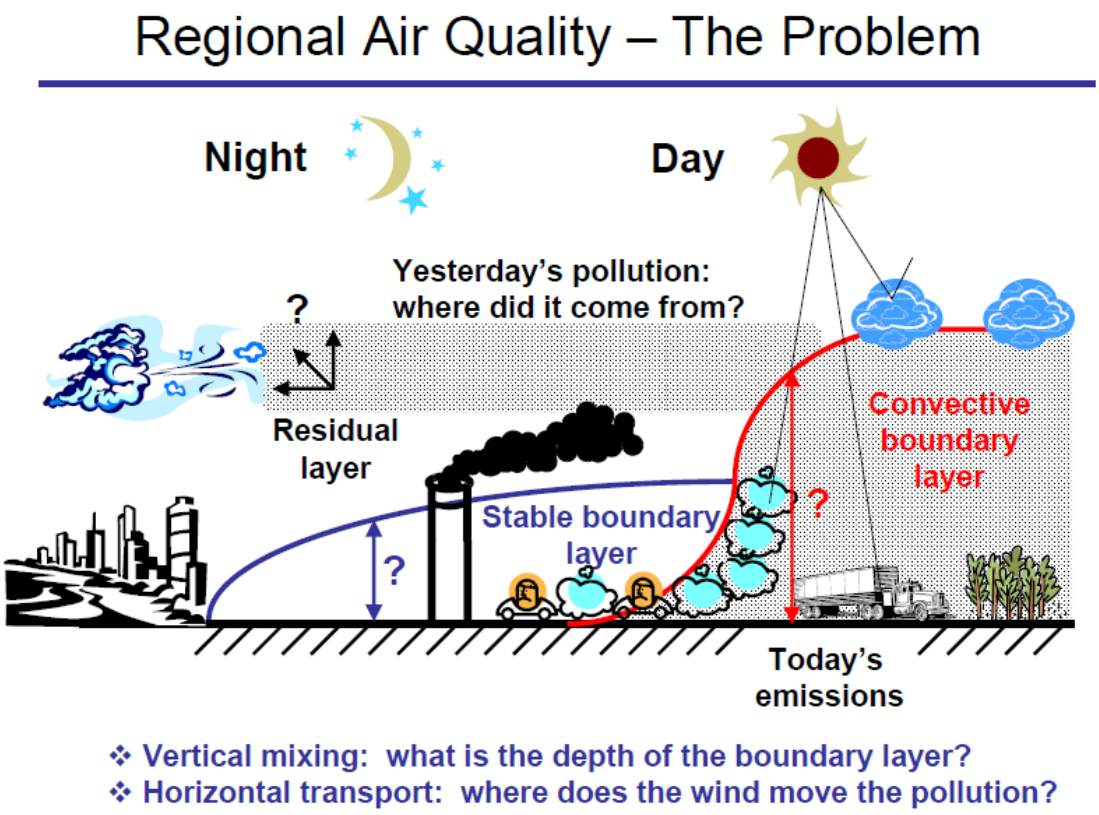

Figure 2.7: Regional air quality problem [24]

The dynamic nature of the PBL influences the concentration and residence time of pollutants in the atmosphere and hence air quality. Our ability to accurately predict air quality is limited by a lack of knowledge of the physical influences on PBL structure [25].

Radiative transfer in the atmosphere is solved in one dimension of the plane parallel atmosphere and in each column defined by the grid size of the model, e.g. the numerical weather prediction and general circulation models. The vertical layers of a model is its vertical resolution. Passive remote sensing only shows two dimensional features. It is too limited in vertical and temporal resolution and measures total column amounts to a few vertical range bins at best. Besides resolution, lidar permits the separation of molecular from backscatter signals.

2.2 CALIPSO

Lidar is a sounding instrument that detects the reflected or backscattered radiation to infer some properties of the target, the distance from which is calculated by the time of flight in the light path. By sampling at different time intervals that correspond to various distances, a profile of the properties along the path is formed. It no longer suffers from the drawback of passive sensing to detect radiation coming from targets that make up an entire column in its field of view. The range resolved nature of lidars allows the sensing of weak atmospheric signals in the presence of a strong background such as detecting aerosols above a land surface. Applications of lidar are numerous and are proved useful in atmospheric studies, vegetation canopy, oil spill detection and topographic uses, just to name a few. Many applications that require understanding of global scale such as climate, water and carbon cycles require observations from satellites.

CALIPSO was launched to a low earth sun-synchronous orbit at 705 km altitiude and an inclination of 98.2 degrees. Its missions are [6]:

1. improve estimate of aerosol forcing.

2. improve characterization of surface longwave radiative fluxes and atmospheric heating rates.

3. improve model parameterizations of cloud-climate feedbacks

Cloud and aerosol profiles help trace the sources of atmospheric pollution. By tracking movements of individual cloud elements we can also determine wind fields [1]. One of the reasons model predictions of climate warming vary from model to model lies in how the model specifies the vertical cloud distributions. CloudSat (launched in 2004) and Cloud-Aerosol and Infrared Pathfinder Satellite Observation (CALIPSO) are missions to accomplish these tasks. CloudSat launched before CALIPSO is part of the constellation of satellites known as A-train to observe precipitation and clouds from space. A-train consists of Aqua, CloudSat, CALIPSO, Parasol and Aura.

2.2.1 Major sensor hardware on CALIPSO

CALIOP(Cloud Aerosol Lidar with Orthogonal Polarization) on board of the CALIPSO is a nadir viewing two wavelength lidar instrument with a $1064nm$ channel and two polarization channels at $532nm$ to retrieve vertical profiles of aerosols and cloud properties. On board co-aligning with the lidar are also two passive instruments, a wide field of view camera (WFC) for scene registration on the daylight side of the orbit to facilitate joint CALIPSO/Aqua retrievals and to identify the presence of low cloud over the footprint of the French Imaging Infrared Radiometer (IIR). The IIR is a starer

providing calibrated radiances to optimize joint lidar/IIR retrievals of cirrus emissivity and particle size.

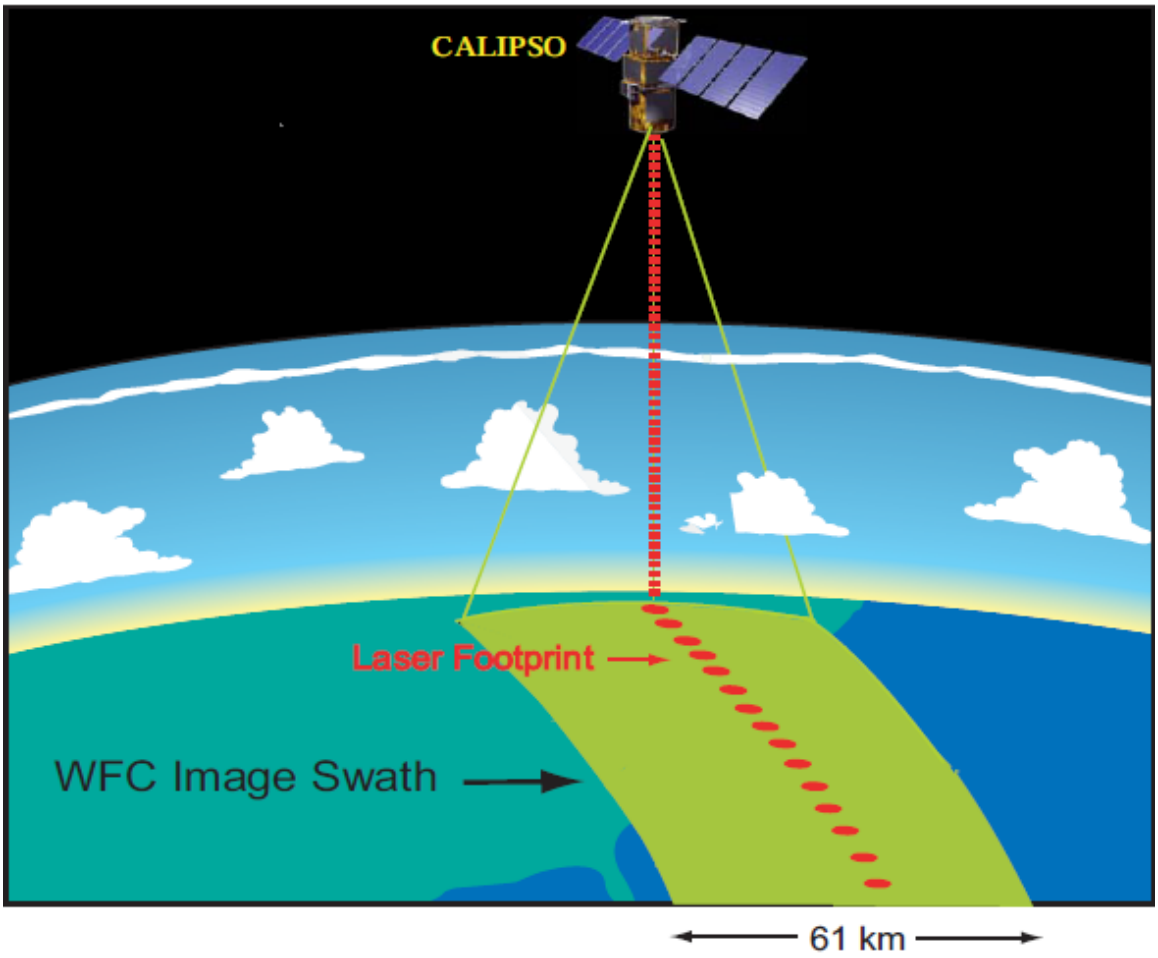

Figure 2.7: Wide Field Camera on board of CALIPSO serves scene registration

2.2.2 Promises of CALIPSO

Lidar provides better resolution, distinction of liquid and ice phase in the case of cloud, discrimination of aerosol into several types even over heterogenous surfaces. From the data collected by the polarization channels $532\|$ and $532\perp$, cloud phase is

established from the depolarization ratio. The overall capabilities of the mission are, layer detection, layer identification, and profile retrievals.

On level 1 of processing, calibration constants are determined and attenuated backscatter coefficients at 532 and 1064 nm are produced. The calibration of the $532nm$ parallel channel is carried out by molecular backscatter from the high altitude aerosol free region. The $532nm$ perpendicular channel is calibrated relative to it. The $1064nm$ channel is calibrated relative to the $532nm$ channel using the assumption that backscatter from cirrus clouds is wavelength independent [7].

Level 2 detects layers, classifies them by type, and retrieves extinctions. Each task is accomplished by an algorithm module: Selective Iterated Boundary Locator (SIBYL), Scene Classification Algorithm (SCA), and the Hybrid Extinction Retrieval Algorithms (HERA).

Since over averaging of detected profiles can destroy features, the scene processes have been designed to extract suitably averaged data from these profiles. SCA first identifies layers as either cloud or aerosol based primarily on the signal strength and spectral dependence; clouds should have no dependence. Cloud is further classified as water or ice cloud using the depolarization signal and temperature profile. Similarly, aerosol types are distinguished by geophysical location, backscatter intensity etc. Then values of lidar ratio are assigned and multiple scattering factor is selected for clouds before the profiles are finally determined.

REFERENCES

[1] Menzel, P.W.,"Cloud tracking with satellite imagery:Form the pioneering work of Ted Fujita to the present.", *Bull. Amer. Soc*.,82,33-47, 2001

[2] " The Cloud mission and the A-train.", *Bulletin of the American Meteorological Society*, Vol. 83, No. 12, December, 2002

[3] Takashi Fujii, Tetsuo Fukuchi, "Laser Remote Sensing", Taylor & Francis, 2005

[4] V. Kovalev et.al, "Elastic Lidar, Theory, practice, and analyses methods*",* John Wiley and sons, New Jersey USA, 2004

[5] Beat Schmid, Christian Matzler, *Member, IEEE,* Alain Heimo, and Niklaus Kampfer, *Member, IEEE,"* Retrieval of Optical Depth and Particle Size Distribution of Tropospheric and Stratospheric Aerosols by Means of Sun Photometry.", *IEEE Transactions On Geoscience And Remote Sensing*, Vol. 35, No. 1, January,pp172-182,1997

[6] CALIOP Algorithm Theoretical Basis Document, Part 1 : CALIOP Instrument, and Algorithms Overview, PC-SCI-202.Part1_v2-Overview, 2006

[7] Reagan, M. J., X.Wang, and M. J. Osborn, "Spaceborne lidar calibration from cirrus and molecular backscatter returns," *IEEE Trans. Geosci. Remote Sens.*, 40, 2285– 2290, 2002

[8] Claus Weitkamp,Lidar, "Ranged-Resolved Optical Remote Sensing of the Atmosphere", Springer, pp120, 2005

[9] Beat Schmid, Christian Matzler, Member*, IEEE,* Alain Heimo, and Niklaus Kampfer, Member, *IEEE,* "Retrieval of Optical Depth and Particle Size Distribution of Tropospheric and Stratospheric Aerosols by Means of Sun

Photometry.", *IEEE Transactions On Geoscience And Remote Sensing*, Vol. 35, No. 1, pp172-182, 1997

[10] Mark Vaughan, Stuart Young, David Winker, Kathleen Powell, Ali Omar, Zhaoyan Liu d, Yongxiang Hu c, and Chris Hostetler, "Fully automated analysis of space-based lidar data: an overview of the CALIPSO retrieval algorithms and data products", *Proc. of SPIE*, Vol. 5575, pp16-30, 2004

[11] Wendisch, M.,"Possibility of refractive index determination of atmospheric aerosol particles by ground-based solar extinction and scattering measurements.", Atmospheric Environment Vol.28, No.5, pp.785-792, 1994

[12] www.cimel.fr

[13] "Optical properties and size distribution of aerosols derived from simultaneous measurements with lidar, a sunphotometer, and an aureolemeter.", Tadahiro Hayasaka, Yasuhiko Meguro, Yasuhiro Sasano, and Tamio Takamura, .", *Applied Optics*, Vol 38, No 9, pp1630-1635, 1999

[14] Tonna,G., Kakajima T., "Aerosol features retrieved from solar aureole data: a simulation study concerning a turbid atmosphere.", *Applied Optics*, Vol 34, No 21, pp 4486-4499, 1995

[15] http://aeronet.gsfc.nasa.gov/new_web/system_descriptions_operation.html

[16] Dubovik, O. and M. D. King, "A flexible inversion algorithm for retrieval of aerosol optical properties from Sun and sky radiance measurements", *J. Geophys. Res.*, 105, 20,673-20,696, 2000.

[17] Dubovik, O., A. Smirnov, B.N. Holben, M.D. King, Y. J. Kaufman, T.F. Eck and I. Slutsker, Accuracy assessment of aerosol optical properties retrieval from

AERONET sun and sky radiance measurements, *J. Geophys. Res* ,105, 9791-9806, 2000.

[18] A. Smimov, B. N. Holben, T. F. Eck, O. Dubovik, and I. Slutsker, "Cloud Screening and Quality Control Algorithms for the AERONET Database", *Remote Sensing of Environment*, 73:337-349, 2000

[19] G. Tonna, T. Nakajima, and R. Rao, "Aerosol features retrieved from solar aureole data: a simulation study concerning a turbid atmosphere", *Applied Optics,* Vol. 34, No. 21, pp4486-4499, 1995

[20] "Aerosol sources, sinks, distributions and processes.",ESRL Chemical Sciences Division, 2008

[21] http://www.etl.noaa.gov/programs/2006/texaqs/

[22] Miam Chin, "Possibilities and challenges in using satellite aerosol data for air quality.", Tropospheric Working Group Report*:* Air Quality (AQ) from Space.

[23] Raymond Hoff, Fred Moshary, Sam Ahmed, Barry Gross, "CREST lidar network", CREST publication series, Vol.7, No.01-2009, 2009

[24] Allen B. White, "The meteorological aspects of regional air quality.", NOAA, Earth System Research Laboratory, 2006

[25] Walter F. Dabberdt, "Meteorological Research Needs for Improved Air Quality Forecasting.", *American Meteorological Society*, pp563-589, 2004

[26] http://aeronet.gsfc.nasa.gov/

Chapter 3 Multiwavelength lidars and retrievals

3.1 Lidar system at CCNY

A ground based multiwavelength Raman-Mie scattering lidar has been operating at New York City (NYC, 40.821°N/73.949°W), as part of Regional East Atmospheric Lidar Mesonet [15] . Our lidar system is monostatic, coaxial and direct detection. Monostatic means the transmitter is co-located with the receiver. Coaxial refers to the receiver axis coinciding with that of the transmtter laser beam, which points vertically through a hatch in the roof after being directed by a series of mirrors to align parallel with the receiver telescope.

The elastic lidar operates with a frequency of $1064nm$ in the near IR. This is the fundamental frequency in the laser cavity. The 2^{nd} and 3^{rd} harmonics are generated by the potassium dideuterium phosphate (KD*P) crystals outside of the oscillator. The short pulses are generated by a Q-switch. High power is needed to gather Raman signals in the daytime. A narrow field of view of the telescope with narrowband interference filters in front of the individual detectors for each channel reduces and rejects background skylight.

The interference filters for the Raman channels must provide a high degree of blocking at the laser wavelength, in our case $355nm$. Since the return for Raman channels are about 3 orders of magnitude less than the Rayleigh-Mie channels, the transmission at the laser wavelength should be about 10 times less than that at the Raman wavelength. An operation check for light rejection by the filters can be carried out when a

low cloud is present to establish if any elastic signal from the cloud is present in the Raman signal [13]

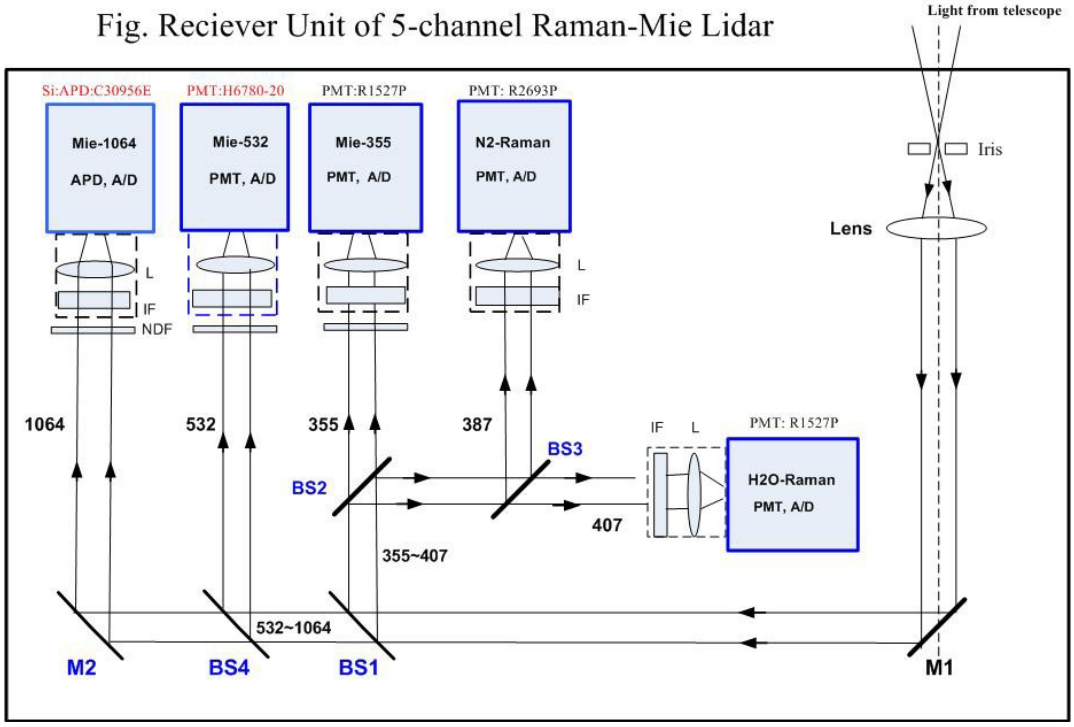

Figure 3.1: Schematics of lidar set up adopted from Leona Charles

3.1.1 Transmitter

Spectra Physics Quanta-Ray PRO-Series pulsed Neodymium-doped Yttrium Aluminum Garnet (Nd:YAG) laser.

Laser		Model Quanta-Ray Nd:YAG PRO 230, 30 Hz rep rate		
Wavelength (nm)	Energy $(mJ/p)^2$	Pulse width (ns)	Short term energy	Long Term Power
1064	950	8-12	± 2%	<3%
532	475	1-2<1064	± 3%	<5%
355	300	2-3<1064	± 4%	<6%

Table 3.1: Brief technical specifications of the transmitter

3.1.2 Receiver

The system uses various neutral density filters (ND) according to the intensity of the solar radiation at the time of measurement(0.1-3 mm).

Detectors	*Si:APD:C30956E* *PMT:H6780-20* *PMT:R1527P(2 pieces),A/D* *PMT:R2693P*
Beam Splitter, Lenses & Mirrors Neutral Density filters	*BS1: T532-1064 R355-407* *BS2: T1064 R 532* *BS3: T355 R 355-407* *BS4: T407 R387* *M1:* Aluminum coating, *M2: 1064* *L1:* Collimating mirror
Interference Filters	Barr Associates Inc, Central wavelength / Bandwidth /Peak transmission Mie channel:1064,532,355 / 0.3~1 nm / T>50% N_2-Raman: 386.7 / 0.3 nm / T=65% H_2O(vapor)-Raman: 407.5 / 0.5 nm / T=65%

Table 3.2: Brief technical specifications of the receiver

Simple receiver mirrors are still in use ages after their invention instead of elaborately thin-film coated lenses because they are easily fabricated with precision and do not suffer from chromatic aberrations. They serve the same purpose of focusing incoming light rays to a spot suitable for detection by bending them through reflection at the mirror or refraction at the lens. A lens can be thought of being made up of a series of prisms which are known to refract light with different degrees at different wavelengths. While a mirror is free of these aberrations, it does not focus all incident light rays at the same focal point either. Axial rays are brought to a different focus on the principal axis than the marginal rays at the edge. This gives rise to a circle of least confusion. A parabolic shaped mirror can correct this problem but it reduces the effective telescope

area slightly. This can be explained by considering that coma aberration is smaller with a spherical surface [14].

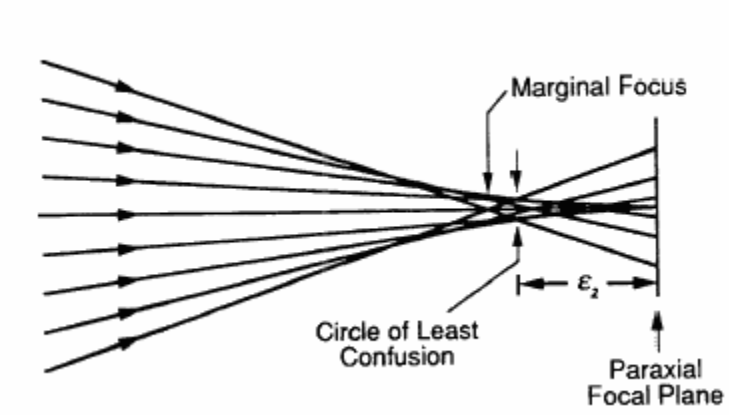

Figure3.2: Circle of least confusion

Two basic mirror configurations are popular with elastic lidar systems, the first one has a folded beam path so that the telescope body becomes shorter. However, fabrication of the primary mirror is also a more difficult process.

1. The Cassegrain telescope

Primary Mirror Secondary Mirror

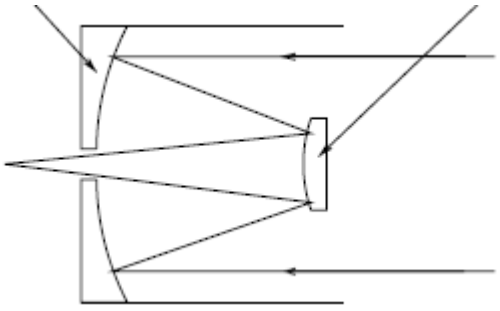

Figure 3.3: Cassegrain telescope

The second common configuration used has a simpler design. This is also the one deployed in our system with a parabolic surface for a primary mirror. The secondary mirror of our receiver is ellipitically shaped to keep a reflected beam circular as the incident.

2. The Newtonian telescope

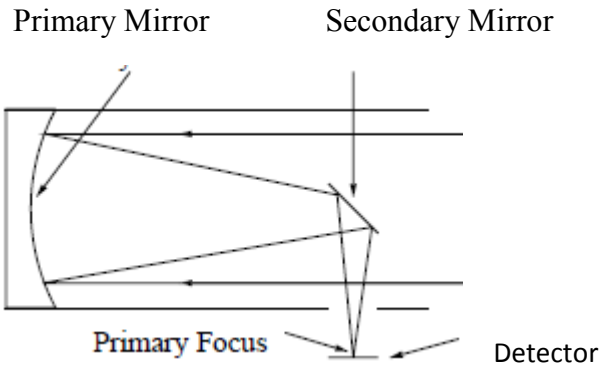

Figure3.4: Newtonian telescope

3.1.3 Data acquisition

Data acquisition is performed using a LICEL transient recorder (TR40-160) sampling at $40MHz$, which gives a spatial resolution of $3.75m$ from $T*c/2$, where T is the period of a sampling cycle, c is the speed of light in air which is the same as in vacuum for most practical purposes. A 12 bit A/D converter quantizes the maximum detector output of $500mV$ into 4096 levels, making each step size of about $0.122mV$

The low pulse repetition rate is normally set at a value so that the averaged profile acquired over a number of shots takes one minute and saved into a data format for further

processing. For example, in order to acquire 1800 shots in one minute, the repetition rate is set at 30.

The repetition rate must not be set too high in order to leave enough time for a previous shot to have returned from the expected remote range. A simple calculation shows that it takes about $0.16ms$ for light to cover $50km$, the maximum range for the power of our transmitter to have any echo to come back, a $30Hz$ repetition rate has a sufficiently long period to satisfy this constraint. By the same token, the sampler must not sample faster than the duration of a pulse, otherwise return from an adjacent range is not simply resolved. The photon counting mode is available for night time acquisitions.

3.1.4 Detection

Heterodyne detection has long been deployed for radio frequencies. Lidar optical detection is often categorized as either direct or heterodyne. Direct detection measures the return power and heterodyne the phase of the optical field in addition. Analog detectors are used for high levels of scattered light resulting from high laser pulse energy used for our day time data acquisition operations. Unlike photon counting in the low light level regime, analog detectors require more complicated calibration schemes. However, analog detectors offer a better dynamic range, over which a photon counting detector can improve by operating with high pulse repetition rate to accumulate counts over many pulses.

3.1.4.1 Photomultiplier tube (PMT) versus (Avalanche photodiode) APD

Comparing the two types of detectors [18], the APD is insensitive to magnetic field, more handily sized and robust, has better linearity, quantum efficiency and efficient operation in the near IR where the PMT cannot operate. Despite the fact that the APD has gains several orders of magnitude lower and a much higher dark noise at $1064nm$, APD is employed primarily for its quantum efficiency. The typical spectral response of the PMT R2693 used our 355nm channel is shown. It is seen that operation of the detector beyond some 600nm is impossible due to the vanishing detector efficiencies. An APD must be used for the 1064nm channel instead.

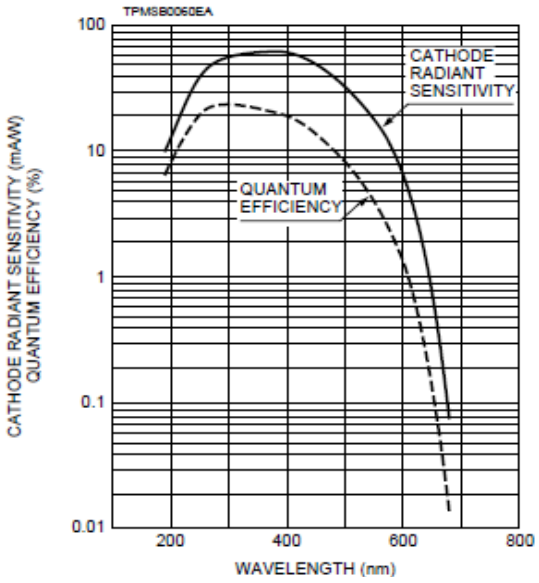

Figure 3.5: Efficiencies of the R2693 PMT [23]

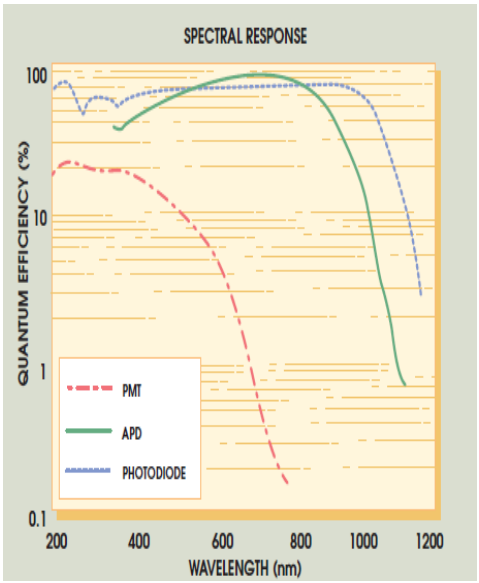

Figure 3.6: Spectral response of a PMT, APD and photodiode [24]

Quantum noise is caused by statistical fluctuations of the emission source or the interaction with the photodetector medium which is the photocathode for a PMT. It follows Poisson statistics,

$$p(n) = \frac{< n >^n}{n!} e^{-<n>} = \frac{< n >}{n} p(n-1) \tag{3.1}$$

which is the probability of observing n photons i.e. the expected number of arrivals $< n >$

Shot noise sources in optical receivers come from processes other than photon fluctuations, emissions described above are also part of the source. It is the dominant noise source when the signal to noise ratio (SNR) is high such as from lidar return at low altitudes [18]. Dark current is another source of it.

A PMT has reasonable quantum efficiency and very low dark noise while the APD has good dynamic range and quantum efficiency but the dark noise is much larger than that for the PMT. Thus, the 532 nm channel has a lower noise equivalent power.

It is not surprising that lidar return signals detected using a PMT [19] or an APD follow a Poisson distribution even though devices do not usually operate in their ideal behavior.

3.2 The need for multiwavelength lidar

The extinction and backscatter coefficients can be written as [10],

$$\alpha(\lambda) = \int n(r)\,\pi r^2\, Q_{ext}(\lambda, r, m)\; dr \tag{3.2}$$

$$Q_{ext}(\lambda, r, m) = \sigma_{ext}(\lambda, r, m) / \pi r^2 \tag{3.3}$$

$$\beta(\lambda) = \int n(r)\,\pi r^2 \left.\frac{dQ_{scat}(\lambda, r, m)}{d\Omega}\right|_{\Omega=\pi} dr \tag{3.4}$$

where $n(r)$ is the particle size distribution function.

$Q_{scat}(\lambda, r, m)$ the scattering efficiency is related to the scattering cross-section efficiency $\sigma_{scat}(\lambda, r, m)$ by $Q_{scat}(\lambda, r, m) = \sigma_{scat}(\lambda, r, m) / \pi r^2$ (3.5)

For a spherical particle shape, the scattering efficiency can be calculated for a known refractive index of the particle. The backscatter coefficient can be calculated by inverting the lidar return, leaving the size distribution function to be fitted into the equation for the scattering efficiency of the particle.

Expressing the scattering coefficient in a discrete size variable r_1,

$$\beta(\lambda_i) = \sum_{j=1} \Delta r\; n(r_j) \pi r_j^{\,2}\, \frac{\Delta Q_{scat}}{\Delta\Omega} \tag{3.6}$$

With as many wavelengths as the number of size intervals in the histogram which approximates the size distribution function $n(r)$, the histogram can be constructed. It is clear that in order to determine the real size distribution, as many wavelengths as possible should be used [11].

Often a power law is adopted to estimate the relative size of monodisperse particles scattering light at two different wavelengths in the same region, the Angstrom exponent.

$$k = \frac{\ln(\beta_2) - \ln(\beta_1)}{\ln(\lambda_1) - \ln(\lambda_2)} \tag{3.7}$$

It is sometimes applied to differentiate atmospheric features in tandem with another instrument. For example, "Ozone Monitoring Instrument (OMI) aboard NASA's Aura Satellite to study intercontinental dust transport and its regional impact on air quality. Our ground based lidar measurements are used to determine the plume Angstrom exponent, which, together with OMI UV absorbing aerosol index allows us to differentiate a plume as a dust event. So multiwavelength measurements give us insight into size of the particle [20]."

3.2.1 Particle parameters retrieval using multiwavelength lidar

In general optical data are related to the particle parameters by the Fredholm integral equations of the first kind where the parameters only appear in the integrand and the integration limits are fixed. Writing it in a more specific form with aerosol retrievals in mind,

$$g_i(\lambda) = \int_{r_{\min}}^{r_{\max}} K_i(r, m, \lambda) v(r)\, dr + \varepsilon_i^{\exp}(\lambda) \tag{3.8}$$

where $g_i(\lambda)$ are the optical data i.e. $\beta(\lambda)$, $\alpha(\lambda)$ etc., $K_i\left(r,m,\lambda\right)$ are the kernel function calculated from the efficiency for each i kind, and $\varepsilon_i^{\exp}(\lambda)$ is the experimental error.

The kernel function also depends on the shape of the particles. The particle parameter to be retrieved is the volume concentration $v(r)$ distribution. For spherical particles, the Kernel is obtained from the extinction or backscatter efficiency $Q_i(r,m,\lambda)$. Dividing the efficiency by the particle volume for numerical stability reason,

$$K_i\left(r,m,\lambda\right) = (3/4r)Q_i(r,m,\lambda) \tag{3.9}$$

In order to solve the ill-posed inverse problem, the volume concentration is approximated by a linear combination of some base triangle shaped functions, B-splines of first degree.

$$v(r) = \sum_j w_j B_j(r) + \varepsilon_i^{math}(r) \tag{3.10}$$

$\varepsilon_i^{math}(r)$ is error caused by approximations and w_i are the weight factors.

In order to determine the weight factors, this linear combination equation for the volume concentration is inserted into the Fredholm integral equation to yield,

$$g_i(\lambda) = \sum_j w_j A_{ij}(m,\lambda) + \varepsilon_i(r) \tag{3.11}$$

where $\varepsilon_i(r) = \varepsilon_i^{\exp}(r) + \varepsilon_i^{math}(r)$ (3.12)

$$A_{ij}(m,\lambda) = \int_{r_{\min}}^{r_{\max}} K_i\left(r,m,\lambda\right) B_j(r)\, dr \tag{3.13}$$

These weight matrix elements are essentially projections of the kernels onto the bases.

The number of base functions is determined by physical and mathematical constraints.

The optical data equation can be written in a vector-matrix form,

$$\mathbf{g} = \mathbf{A}\mathbf{w} + \boldsymbol{\varepsilon} \tag{3.14}$$

The minimization step defined with minimizing the Euclidian norm can be solved by regularizing the Lagrange multiplier in a penalty imposed by a smooth and positive solution of the weight factors.

$$\left\|\boldsymbol{\varepsilon}\right\|^2 = \left\|\mathbf{A}\mathbf{w} - \mathbf{g}\right\|^2 \tag{3.15}$$

"The retrieval of microphysical particle properties from lidar measurements belongs to the class of severely ill-posed problems. This definition arises from several features connected to lidar observations. Measurement errors are much larger than round-off errors. Incompleteness is given by the small number of wavelengths, as well as the fact that only backscatter and extinction information is available. The non-uniqueness of the solutions follows from the highly complex structure of tropospheric aerosols. They may be multimodal and of variable shapes. The complex refractive index of the particles may be wavelength or size dependent or both. Particle shape often deviates from sphericity. Accordingly different combinations of the target parameters may lead to a similar optical spectra within the measurement uncertainty [9]."

The retrieval of particle parameters is much more difficult than preparing the input optical data.

3.3 Data inversion

3.3.1 Optical data from lidar equation

Consider a laser pulse emitted at time t where t_1 is the rise time and t_2 the fall time i.e. $t_1 < t < t_2$. The temporal distribution of the backscattered radiation on the detector is not simply the product of the irradiance at the target and the backscatter coefficient but their convolution. It is because the received light does not originate from the time $t = ct/2$ alone but from the whole time interval $(t_1 \;\; t_2)$. In practice the convolution integral is eliminated by choosing short pulses during which the changes in the backscatter coefficient are not noticeable. The time bins of the digitizing equipment must be comparatively short too. In these limits, the lidar equation can be written as,

$$P(z) = C\frac{\beta_p(z) + \beta_m(z)}{z^2}\exp\left\{-2\int_0^z \alpha_p(z') + \alpha_m(z')\; dz'\right\} \tag{3.16}$$

where *p* represents particulates and *m* molecular components respectively.

$\alpha's$ are the extinction coefficients, and $\beta's$ are the backscatter coefficients.

C is the system constant that contains all the efficiency factors in the optical and electronic components that transmit the laser power and receive the backscattered light.

Absorption and scattering make up extinction of light. If the scatterers exhibit no absorption of the incident light, its extinction must be due to scattering alone into all directions of 4π solid angle. In the visible region, absorption by molecules is negligible and, given the small imaginary part of the refractive index, also small by aerosols. Therefore, a direct relationship between the two optical properties are expected. A linear relationship is assumed in order that the Bernoulli differential equation which follows from the lidar equation be solved. It is this linear relationship between the extinction coefficient and the backscatter coefficient that is called the lidar ratio, $S(\lambda,z)=\alpha(\lambda,z)/\beta(\lambda,z)$. Its inverse is the value of the scattering phase function at 180^0, assuming that there is no absorption.

The solution to the lidar equation for the backscatter coefficient is given by the Fernald equation [25, 26]. For the derivation of the equation, please refer to **A.3** of the Appendix.

$$\beta_p(z)=\frac{P(z)z^2\exp\left[2\left(S_m-S_p\right)\int_0^z\beta_m(z')\,dz'\right]}{C-2S_p\int_0^z P(z)z^2\exp\left[2\left(S_m-S_p\right)\int_0^z\beta_m(z')\,dz'\right]dz'}-\beta_m(z) \tag{3.17}$$

The value of C is normally not known for a lidar system so a boundary condition can be used instead in the lidar equation to substitute for it. Owing to the nonlinearity of the governing differential equation, Klett has shown through numerical calculations that setting the boundary condition at the far end is more stable than at the near end. Klett defined a range dependent function $C(z)$ relating the backscatter and extinction coefficients, $\beta(z)=C(z)\alpha^k(z)$. It is the reciprical of the lidar ratio when $k=1$.

Bissonette went on to show that the sensitivity of the lidar solution on the boundary value and $C(z)$ depends strongly on the inversion method [4].

Klett's far end solution for the two components atmosphere becomes [7],

$$\beta_P(z) = \frac{P(z)z^2 \exp\left[-2\left(S_m - S_p\right)\int_z^{z_c} \beta_m(z')dz'\right]}{CT_m^{\,2}(z_c)T_P^{\,2}(z_c) + 2S_p\int_z^{z_c} P(z)z^2 \exp\left[-2\left(S_m - S_p\right)\int_z^{z_c} \beta_m(z')dz'\right]dz} - \beta_m(z) \tag{3.18}$$

Since $C = P(z)z^2\left[\beta_m(z) + \beta_P(z)\right]^{-1} T_m^{\,-2}(z)T_P^{\,-2}(z)$ from the lidar equation,

when the boundary condition is set at the far range of the integration path,

$$\beta_P(z) = \frac{P(z)z^2 \exp\left[-2\left(S_m - S_p\right)\int_z^{z_c} \beta_m(z')dz'\right]}{\frac{P(z_c){z_c}^2}{\beta_m(z_c) + \beta_P(z_c)} + 2S\int_z^{z_c} P(z)z^2 \exp\left[-2\left(S_m - S_p\right)\int_z^{z_c} \beta_m(z')dz'\right]dz} - \beta_m(z) \tag{3.19}$$

At 532 nm the error in neglecting the aerosol contribution $\beta_p(z_c)$ to scattering in the troposphere above the mixed layer is often less than 1% to 5% [8].

3.3.1.1 Error in optical depth caused by error in baseline

In some lidar system the baseline is determined by recording the background signal before a shot is fired to acquire a profile. More commonly it is determined by

averaging the lidar return at a far range interval. The figure shows a return profile plagued with sky noise from such an interval.

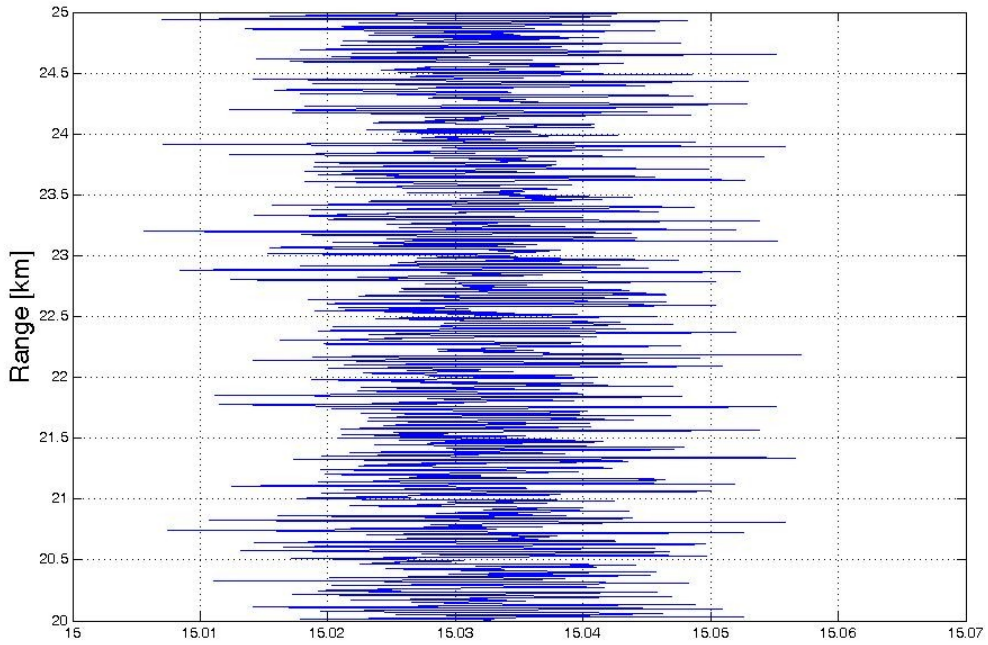

Figure 3.7: signal background interval to determine baseline

Next consider an error of magnitude b which is added or subtracted to the average lidar signal in the background interval, this causes an error in the calculated backscatter,

$$\beta + \Delta\beta = \frac{\left[b + P(z)\right] z^2 \exp\left[-2\left(S_R - S\right)\int_z^{z_c} \beta_R(z')dz'\right]}{\frac{\left[b + P(z_c)\right] z_c^{\,2}}{\beta_R(z_c)\left[1 + \frac{\beta_P(z_c)}{\beta_R(z_c)}\right]} + 2S\int_z^{z_c}\left[b + P(z)\right] z^2 \exp\left[-2\left(S_R - S\right)\int_z^{z_c} \beta_R(z')dz'\right]dz} \quad (3.20)$$

For algebraic manipulations, let $\beta = N/D$ for $b = 0$ i.e. when there is no baseline error. The calculated backscatter is then the error free numerator when $b = 0$ plus an error term determined by b, divided by the error free denominator plus an error term determined by b.

$$\beta + \Delta\beta = \frac{bz^2 \exp\left[-2\left(S_R - S\right)\int_z^{z_c} \beta_R(z')dz'\right] + N}{\frac{bz_c^{\,2}}{\beta_R(z_c)\left[1+\frac{\beta_P(z_c)}{\beta_R(z_c)}\right]} + 2S\int_z^{z_c} bz^2 \exp\left[-2\left(S_R - S\right)\int_z^{z_c} \beta_R(z')dz'\right]dz + D} \tag{3.21}$$

Let the ratio of two denominators be $y(z)$, one denominator in the Fernald expression for the constant error signal b, the other for the varied lidar returns as follows,

$$y(z) = \frac{\frac{bz_c^{\,2}}{\beta_R(z_c)\left[1+\frac{\beta_P(z_c)}{\beta_R(z_c)}\right]} + 2S\int_z^{z_c} bz^2 \exp\left[-2\left(S_R - S\right)\int_z^{z_c} \beta_R(z')dz'\right]dz}{\frac{p(z_c)z_c^{\,2}}{\beta_R(z_c)\left[1+\frac{\beta_P(z_c)}{\beta_R(z_c)}\right]} + 2S\int_z^{z_c} p(z)z^2 \exp\left[-2\left(S_R - S\right)\int_z^{z_c} \beta_R(z')dz'\right]dz} \tag{3.22}$$

This quantity is signal profile, error and altitude dependent and cannot be simplified analytically. An example of this for a typical atmosphere with an error of $b = 0.05$ is plotted below and assumes values between 0 and 1. The upper limit 1 at the far range is obtained when the baseline error is the same as the signal strength with a $SNR = 1$

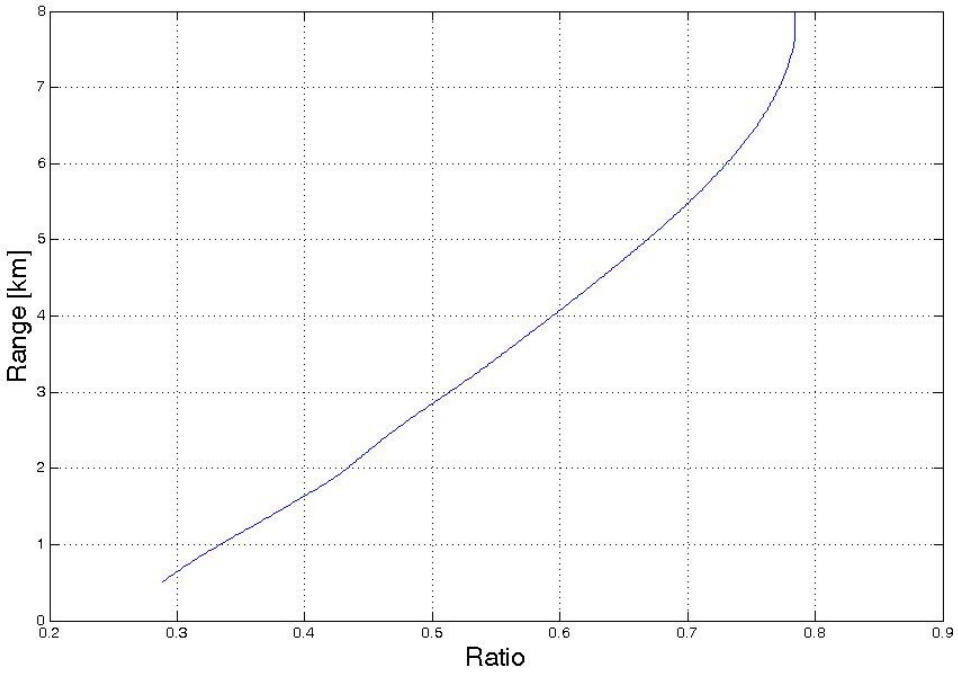

Figure 3.8: shows defined ratio $y(z)$

In terms of this defined ratio,

$$\beta + \Delta\beta = \frac{bz^2 \exp\left[-2\left(S_R - S\right)\int_z^{z_c} \beta_R(z')dz'\right] \Big/ D + N/D}{1 + y(z)} \tag{3.23}$$

Upon simplification,

$$\frac{\Delta\beta}{\beta} = \frac{b/p(z) - y(z)}{1 + y(z)} \tag{3.24}$$

The same profile is used to estimate the percentage error of the retrieved optical depths caused by the baseline errors.

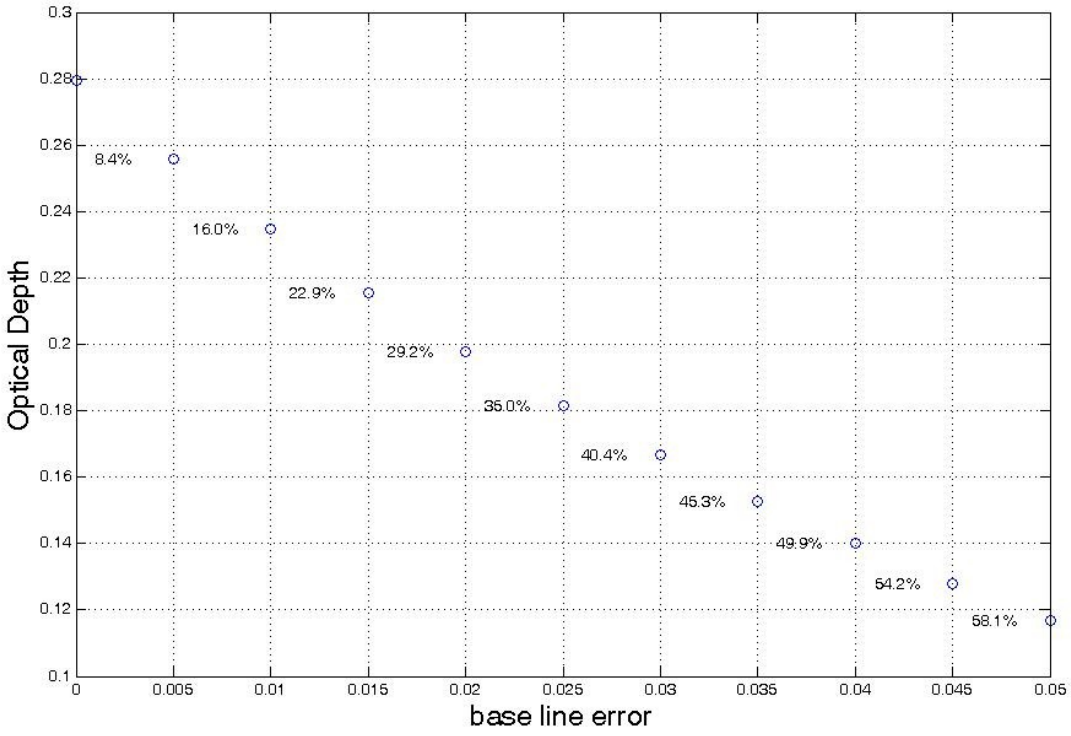

Figure 3.9: shows percentage error in optical depth caused by an error in the baseline for an atmosphere of optical depth 0.28

For the sky background in Figure (3.7) shown, $b \approx \pm 0.02$ which causes a percentage error of ~ for the atmosphere of $\tau = 0.28$ A decrease in the calculated optical depth with an increased baseline error seems contradictory to our expectation that larger signal return should result in larger backscatter and hence extinction and optical depth. This is not so because the increased baseline changes the boundary condition at the far end. The effect is an increase in the calibration constant in the denominator of the Fernald solution therefore decreasing the fraction N/D as defined previously.

3.3.1.2 Unknown lidar ratios

Now that an estimate of the boundary condition is assumed, what is lacking is the knowledge of an appropriate lidar ratio. But the choice is uncertain. The lidar ratio is highly dependent on the size distribution and refractive index. It is generally expected to take on a value between 0 and 90. It can be estimated for similar backscatter profiles of different wavelengths by taking into account that the backscatter coefficient has less sensitivity to the lidar ratio for a longer wavelength than a shorter [3].

The lidar ratio relates two parameters each of which depends on the refractive index and size distribution. For a more than one component atmosphere, each component refracts light differently and has its own distribution quite independent of the other. The combination of these two factors cannot be uniquely determined for inputs into calculations. After all, if these parameters are known, the extinction and scattering coefficients can be calculated by Mie theory, there would be no need for the lidar ratio. In the case of hygroscopic aerosols, even for a well mixed layer, a required knowledge of the humidity profile also complicates the accuracy of the results. Salemink et al. [2] found a linear increase of the lidar ratio from 25 to 70 sr between 40% and 80% relative humidity near the surface.

Aerosol type	**Lidar ratio**
Saharan dust	50-80 sr
Marine particles	20-35 sr
Less absorbing urban particles	35-70 sr
Absorbing particles from biomass burning	70-100 sr

Table 3.3: Typical lidar ratio for different aerosol types at532nm [22]

The large variation range of lidar ratios makes it practically impossible to calculate trustworthy extinction and backscatter profiles from the elastic lidar equation. The optical depth and the integrated backscatter inverted by sunphotometer data only give a columnar average. The usual lidar ratios only make the first guesses while the true ratio profile remains unknown.

In essence, two quantities cannot be determined by the measured lidar return alone, hence the need for an assumption of the lidar ratio to relate them. The lidar ratio can be said as a major drawback of the elastic lidar. The use of the Raman retrieval does not depend on the this ratio.

3.4 Raman lidar

3.4.1 Principle of Raman lidar

The physical origin of the Raman effect is the polarizability of a molecule changing in an incident electric field and coupled with its normal modes. In the classical description, the oscillating electric moment in one of its coordinate components is given by,

$$\mu = \varepsilon_0 \left\{ \alpha_0 \cos 2\pi \nu_0 t + \sum_k \left. \frac{\partial \alpha}{\partial Q_k} \right|_0 Q_k{}^0 \left[\frac{1}{2} \cos 2\pi \left(\nu_0 + \nu_k \right) t + \cos 2\pi \left(\nu_0 - \nu_k \right) t \right] \right\}$$

where Q_k is the amplitude of the k^{th} normal coordinate, ε_0 is the amplitude of the incident field, α_0 is the polarizability at equilibrium position.

What is noteworthy is the presence of the shifted frequencies $\nu_0 \pm \nu_k$ in the oscillating dipole along with the incident light at ν_0.

Classical mechanics is inadequate to treat the entire Raman scattering phenomenon, for instance, the intensities ratio of the Stokes to anti-Stokes line is given by an expression that is in contradiction with experimental findings [10].

$$\frac{I_{Stokes}}{I_{anti-Stokes}} = \left(\frac{\nu_0 - \nu_k}{\nu_0 + \nu_k} \right)^4$$

The phenomenon of inelastic scattering is not restricted to any gas. It occurs whenever its molecules are excited into some virtual states and exchange quanta with the incident light. Whether such an interaction occurs or not depends mainly on the symmetry of the molecule and its electronic configurations. There are usually a few selection rules to determine whether certain transitions are allowed or not with occasional exceptions. As long as the gas is Raman active with a sufficient concentration in the atmosphere, return measurements can be made using a lidar setup.

In Raman scattering, vibration and/or rotational quanta are exchanged between incident photons and the impinged molecules. As a result, the scattered photon undergoes a frequency shift after leaving the molecule by the amount $\pm\Delta\tilde{\nu}$. In the case of a positive amount of energy being absorbed from the beam which is red-shifted and has a decreased frequency of $\tilde{\nu}$ ~, one speaks of Stokes scattering. When the energy comes from vibrations or rotations of the molecule, the blue-shifted beam has an increased frequency of $\tilde{\nu}$ ~, one speaks of anti-Stokes scattering.

The shift is given by the relationship $\Delta\tilde{\nu}$ hc_0

For diatomic molecules such as N_2 and O_2 in our case of interest, the vibrational energy levels based on the model of a freely rotating harmonic oscillator are given by,

$$E_{vib,v} = hc_0\tilde{\nu}\ \ 2), \qquad v = 0,1,2,.... \tag{3.25}$$

where $\tilde{\nu}$ is the oscillator frequency and v is the vibrational quantum number.

For the rotational energy levels,

$$E_{rot,J,v} = hc_0\left[B_vJ(J+1) - D_vJ^2(J+1)^2\right], \qquad J = 0,1,2,... \tag{3.26}$$

J is the rotational quantum number belonging to a vibrational level, ν.

B_v is the specific rotational constant and D_v is the centrifugal distortion or stretching constant of the molecule. According to quantum mechanical principles, not all the transitions are valid, only those in compliance with the selection rule are allowed, which are,

$$\Delta\nu = 0,\pm1 \quad \text{and} \quad \Delta J = 0,\pm2, \quad \text{with} \quad \Delta J = J' - J'' \tag{3.27}$$

J' is the quantum number of the higher and J'' the lower energy level in the transition regardless of which level is initial or final.

The schematic depicts transitions between different vibration-rotation energy levels for the N_2 molecule. In the middle of the scheme is Rayleigh scattering, $\Delta\nu = 0$

and $\Delta J = 0$ On the left of the schematic is Stokes $\Delta \nu = +1$ vibration-rotation band, on the right the anti-Stokes $\Delta \nu = -1$ vibration-rotation band. The Q branch corresponds to the vibrational transitions with no change in rotational quantum number $\Delta J = 0$ and is not resolved in lidar applications. The $\Delta J = +2$ band of transitions was historically given a name of S branch and $\Delta J = -2$ O branch. The branches to either side of the Rayleigh line are S because $J' > J''$ at the same vibrational level $\Delta \nu = 0$

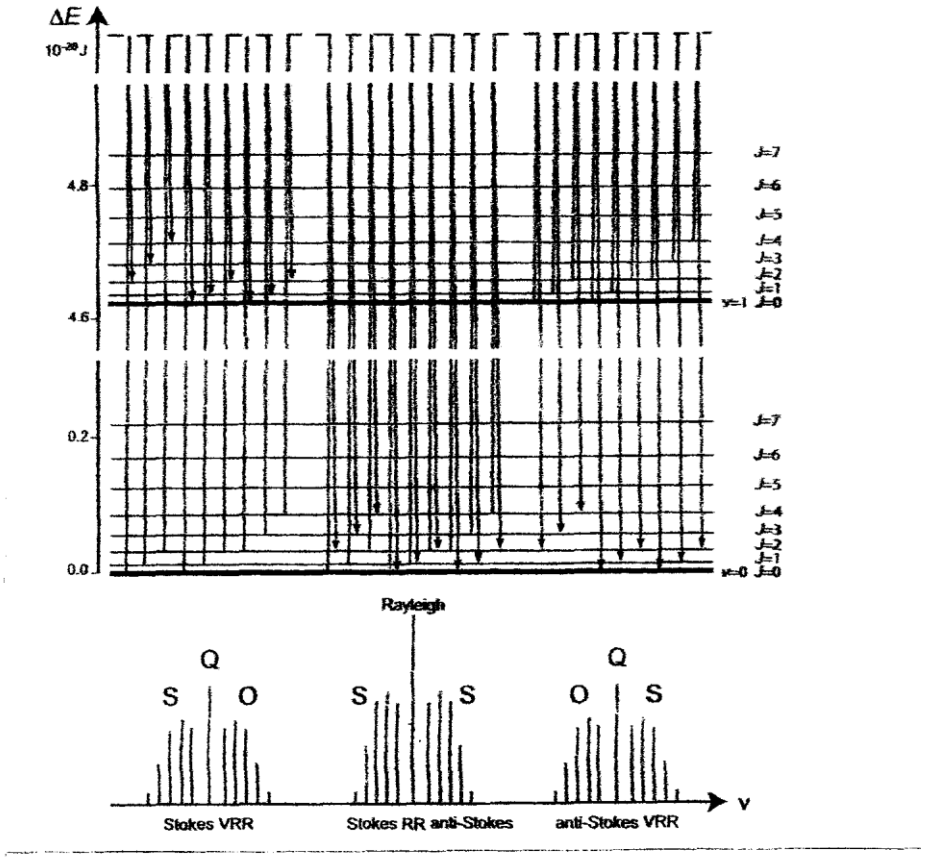

Figure 3.5: Upper: Vibration-rotation energy levels of the N_2 molecule. Lower: Raman transition lines or bands [27].

The vibrational rotational Stokes line $\Delta\nu = +1$ is shifted by the wavenumber $2330.7\,cm^{-1}$ at the laser wavelength of $354.7nm$ and the Raman vibrational spectrum of water vapor by approximately $3652\,cm^{-1}$. The center of nitrogen Raman spectrum is thus $\approx$ 386.7 nm. It makes the water vapor Raman signal center at $407.5\,nm$ [13]. Incidentally, the return signal at $354.7nm$ consists of Rayleigh, Mie and rotational Raman backscattering.

For the inelastic backscatter nitrogen Raman signal, the following equation is derived to retrieve the attenuation coefficients profile of aerosols.

$$P_{\lambda_R}(z) = K_{\lambda_R}\frac{O(z)}{z^2}N_R(z)\frac{d\sigma_{\lambda_R}(\pi)}{d\Omega} \times \exp\left\{-\int_{z_{\min}}^{z_{\max}} \alpha_{\lambda_0}{}^{mol}(z') + \alpha_{\lambda_0}{}^{aer}(z') + \alpha_{\lambda_R}{}^{mol}(z') + \alpha_{\lambda_R}{}^{aer}(z')\,dz'\right\} \tag{3.28}$$

$P_{\lambda_R}(z)$ is the power received from range z at the Raman wavelength λ_R [21].

K_{λ_R} --system constant $O(z)$ --overlap function

$\frac{d\sigma_{\lambda_R}(\pi)}{d\Omega}$ --range-independent differential Raman cross section in the backward direction

$N_R(z)$ --nitrogen molecular number density

The α 's are the attenuation coefficients for aerosols or molecules at the specified wavelengths, for instance, $\alpha_{\lambda_0}{}^{mol}$ for nitrogen at laser wavelength.

3.4.2 Extinction coefficient

The extinction coefficient can be derived by differentiation of the equation (3.28) with respect to range and assuming an Angstrom coefficient of $k = 1$ for aerosol particles and water droplets sized comparable with the measurement wavelength,

$$\frac{\alpha_{\lambda_0}^{aer}}{\alpha_{\lambda_R}^{aer}} = \left(\frac{\lambda_R}{\lambda_0} \right)^k \tag{3.29}$$

$$\alpha_{\lambda_0}^{aer}(z) = \frac{\dfrac{d}{dz}\left[\ln \dfrac{N_R(z)}{P_{\lambda_R}(z) z^2} \right] - \alpha_{\lambda_0}^{mol}(z) - \alpha_{\lambda_R}^{mol}(z)}{1 + \left(\dfrac{\lambda_0}{\lambda_R} \right)^k} \tag{3.30}$$

The molecular number density $N_R(z)$ is easily calculated from the ideal gas law $p = NkT$ where the pressure and temperature profiles are given by atmospheric sounding or calculated using a standard model of the atmosphere.

This equation is better put into other forms more suitable for numerical calculations. Not only is the derivative of the ratio in the previous equation difficult to evaluate accurately, it also goes against the rules of statistics to evaluate it by a least square fit because the ratio of two Gaussian variables does not follow Gaussian statistics.

$$\alpha_{\lambda_0}^{aer}(z) = \frac{\dfrac{1}{N_R(z)} \dfrac{d\left[N_R(z) \right]}{dz} - \dfrac{1}{P_{\lambda_R}(z) z^2} \dfrac{d\left[P_{\lambda_R}(z) z^2 \right]}{dz} - \alpha_{\lambda_0}^{mol}(z) - \alpha_{\lambda_R}^{mol}(z)}{1 + \left(\dfrac{\lambda_0}{\lambda_R} \right)^k} \tag{3.31}$$

In this form, the concentration ratio of nitrogen in air is conveniently substituted by the mere concentration of air since the atmospheric gases are well mixed in the lower atmosphere. The optical depth is obtained by integrating the extinction equation. The advantage of this evaluation is not having to evaluate the derivative.

$$\tau^{aer} = \int_{z_2}^{z_1} \alpha_{\lambda_0}{}^{aer}(z')\, dz' = \frac{\ln\left[\frac{N_R(z)}{P_{\lambda_R}(z)z^2}\right]_{z_1}^{z_2} - \int_{z_2}^{z_1} \alpha_{\lambda_0}{}^{mol}(z') + \alpha_{\lambda_R}{}^{mol}(z')\, dz'}{1+\left(\frac{\lambda_0}{\lambda_R}\right)^k} \qquad (3.32)$$

For a higher accuracy of the solution, a least square fit is used to fit the data.

3.4.3 Backscatter coefficient

By forming the ratio of the power returns from the elastic and a Raman channel at two altitudes one of which is set at a reference range where the aerosol backscatter is much smaller compared to the molecular backscatter, the backscatter coefficient can be calculated.

Forming the ratio of the power returns : $\frac{P_{\lambda_0}(z)P_{\lambda_R}(z_{ref})}{P_{\lambda_0}(z_{ref})P_{\lambda_R}(z)}$

$$\beta_{\lambda_0}{}^{aer}(z)+\beta_{\lambda_0}{}^{mol}(z)=\left[\beta_{\lambda_0}{}^{aer}(z_{ref})+\beta_{\lambda_0}{}^{mol}(z_{ref})\right]\times\frac{P_{\lambda_R}(z_{ref})P_{\lambda_0}(z)N_R(z)}{P_{\lambda_0}(z_{ref})P_{\lambda_R}(z)N_R(z_{ref})}$$
$$\times\frac{\exp-\int_{z_{ref}}^{z}\alpha_{\lambda_R}{}^{aer}(z')+\alpha_{\lambda_R}{}^{aer}(z')\,dz'}{\exp-\int_{z_{ref}}^{z}\alpha_{\lambda_0}{}^{aer}(z')+\alpha_{\lambda_0}{}^{aer}(z')\,dz'} \tag{3.33}$$

With the nitrogen or water vapor Raman channel, the lidar ratio can be derived from the extinction and backscatter coefficients with the assumption of aerosol backscatter being much smaller compared to the molecular backscatter at the reference altitude.

In terms of the aerosol backscatter ratio, $R_{\lambda_0}(z)=\dfrac{\beta_{\lambda_0}{}^{aer}(z)+\beta_{\lambda_0}{}^{mol}(z)}{\beta_{\lambda_0}{}^{mol}(z)}$ (3.34)

and using the backscatter coefficient β relationship to the differential Raman backscatter cross section of a gas of molecules having a number density N [5],

$$\beta(z,\lambda_L,\lambda_R)=N(z)\frac{d\sigma(\lambda_L,\lambda_R,\pi)}{d\Omega} \tag{3.35}$$

A change of the subscript notation into a functional dependence is introduced here for ease of viewing whenever necessary. The backscatter coefficients in equation (3.33) becomes,

$$R(\lambda_0,z)=\frac{P(\lambda_0,z)}{P(\lambda_N,z)}R\left(\lambda_o,z_{ref}\right)\frac{P(\lambda_{N2},z_{ref})}{P(\lambda_0,z_{ref})}\frac{\exp\left\{-\int_{z}^{z_{ref}}[\alpha_p(\lambda_0,z')+\alpha_m(\lambda_0,z')]dz'\right\}}{\exp\left\{-\int_{z}^{z_{ref}}[\alpha_p(\lambda_N,z')+\alpha_m(\lambda_N,z')]dz'\right\}} \tag{3.36}$$

The ratio of the transmissions is often taken to be 1 as a result of a separation of two wavelengths not far apart from each other. For more accurate results, a correction factor

can be made by evaluating some model atmosphere with varying optical depths and one value chosen to represent the appropriate turbidity. The aerosol backscatter ratio can be assumed to be 1 in the upper atmosphere where the lidar return is found to be at minimum.

It is seen that neither a lidar ratio nor a calibration constant is needed to retrieve the extinction and backscatter profiles to overcome the problem of assuming these parameters for the Mie Lidar. The lidar ratio can be retrieved by forming the ratio of the two parameters derived by the Raman signal, equation (3.31) and equation (3.33).

Raman scattering cross sections are on the order of 10^3 smaller than those for molecular scattering [12]. It is the major drawback of Raman lidar. Processing low SNR Raman signal requires temporal and spatial averaging. The typical resolution of Raman measurement is 1 to 30 minutes and 50 to 300 meters in the lower atmosphere [9].

3.4.4 Water vapor Raman channel

Similar to the nitrogen Raman return, the water vapor return signal is described by the equation with $N_W(z)$ denoting the concentration of atmospheric water vapor.

$$P_{\lambda_R}(z) = K_{\lambda_R} \frac{O(z)}{z^2} N_W(z) \frac{d\sigma_{\lambda_R}(\pi)}{d\Omega} \times \exp\left\{-\int_{z_{\min}}^{z_{\max}} \alpha_{\lambda_0}{}^{mol}(z') + \alpha_{\lambda_0}{}^{aer}(z') + \alpha_{\lambda_R}{}^{mol}(z') + \alpha_{\lambda_R}{}^{aer}(z')\, dz'\right\} \tag{3.37}$$

3.4.4.1 Water mixing ratio

Dividing the water vapor return by the nitrogen return and rearranging the resulting equation, keeping in mind that the differential backscatter cross sections are range independent, with the simplified assumption that the overlaps are the same for the two returns, the ratio of the returns is [28],

$$\frac{M_W N_W(z)}{M_{air} M_{air}(z)} = C \times \frac{P(\lambda_W, z)}{P(\lambda_N, z)} \times \frac{\exp\left\{-\int_{z_0}^{z} \alpha(\lambda_N, z')\, dz'\right\}}{\exp\left\{-\int_{z_{r0}}^{z} \alpha(\lambda_W, z')\, dz'\right\}} \tag{3.38}$$

The constant C accounts for M_W / M_{air} of molecular masses, N_N / N_{air} number densities, backscatter cross sections ratio, transmission of detection efficiencies to the two lidar systems.

The exponential terms are the ratio of transmissions in the two Raman wavelengths which are close to each other and is often assumed to be 1. Recognizing that the ratio, $M_W N_W(z) / M_{air} M_{air}(z)$ mass of water vapor to mass of dry air is the water mixing ratio. The constant C for atmospheric water vapor can be calibrated against the water mixing profile accompanying radiosonde measurements.

Evaluation should be performed with a least-squares fit of the lidar data to a radiosonde water vapor measurement.

REFERENCES

[1] Yasumori Saito et al., “Experimental Discussion on Eye-Safe 1.54μm Photon Counting Lidar Using Avalanche Photodiode.”,*Optical Review,* Vol.11, No.6, 378-384, 2004

[2] Salemink, H., P. Schotanus, and J. B. Bergwerff, 1984, "Quantitative lidar at 532 nm for vertical extinction profiles in the lidar solution." *Appl. Phys.,* 34B**,** 187–189, 1984

[3] Yasuhiro Sasano and Edward V. Browell," Light scattering characteristics of various aerosol types derived from multiple wavelength lidar observations", *Applied optics* , Vol. 28, No. 9 , 1670-1679, 1989

[4] Luc R. Bissonnette, 1986, "Sensitivity analysis of lidar inversion algorithms.", Vol. 25, No. 13, *Applied Optics*, 2122-2125,1986

[5] Albert Ansmann, Maren Riebesell, and Claus Weitkamp, "Measurement of atmospheric aerosol extinction profiles with a Raman lidar.",*Optics Letters*,Vol. 15, No. 13, 747-748,1990

[6] D.N.Whiteman, "Application of statistical methods to the determination of slope in lidar data.", *Appl. Opt*. 38, 3360-3369, 1999

[7] James D. Klett.," Stable analutical inversion solution for processing lidar returns." *Applied Optics*, 20(2):211-220, 1981

[8] Stuart A. Young, "Analysis of lidar backscatter profiles in optically thin clouds.", Vol. 34, No. 30, *Applied Optics,* 7019-7031, 1995

[9] Claus Weitkamp,Lidar, "Ranged-Resolved Optical Remote Sensing of the Atmosphere.", Springer, pp265, 2005

[10] van der Hulst, H.C., "Light Scattering by Small Particles", Dover Publications, Inc., New York, 1957

[11] S. Chudzynski et al,"Multiwavelength lidar for measurements of atmospheric aerosol Optics and Lasers in Engineering.",37,91–99, 2001

[12] Vladimir A. Kovalev, William E. Eichinger,"Elastic Lidar, Theory, Practice, and Analysis Methods.", Wiley, pp397, 2004

[13] D. N. Whiteman, S. H. Melfi, and R. A. Ferrare,"Raman lidar system for the measurement of water vapor and aerosols in the Earth's atmosphere.", Vol. 31, No. 16, *Applied Optics,*pp3068-3082,1992

[14] Raffaele Velotta, Bruno Bartoli, Roberta Capobianco, Luca Fiorani, and Nicola Spinelli,"Analysis of the receiver response in lidar measurements", Vol. 37, No.30, *Applied Optics,* pp6999-7007,1998

[15] R. M. Hoff, et al., "Regional East Atmospheric Lidar Mesonet:REALM, in Lidar Remote Sensing in Atmospheric and Earth Sciences.", edited by L. Bissonette, G. Roy, and G. Valle´e, pp. 281– 284, Def. R&D Can. Valcartier, Val-Be´lair, Quebec, 2002

[16] Gregory R. Osche, " Optical Detection Theory for laser applications.", Wiley, 2002

[17] Takashi Fujii, Tetsuo Fukuchi, "laser Remote Sensing.", Taylor and Francis, 2005

[18] I. Balin et al.,"Simultaneous measurement of atmospheric temperature, humidity, and aerosol extinction and backscatter coefficients by a combined vibrational–pure-rotational Raman lidar.", *Appl. Phys. B* 79, 775–782 , 2004

[19] Zhaoyan Liu and Nobuo Sugimoto, "Simulation study for cloud detection with space lidars by use of analog detection photomultiplier tubes.", Applied Optics, Vol.41, No.9, 2002

[20] Leona Charles**,** "Thesis: Intra and Inter-Continental Aerosol Transport and Local and Regional Impacts.", 2008

[21] Albert Ansmann, Ulla Wandinger, Maren Riebesell, Claus Weitkamp, and Walfried Michaelis, "Independent measurement of extinction andbackscatter profiles in cirrus clouds by using a combined Raman elastic-backscatter lidar", Vol. 31, No. 33, *Applied Optics,* 1992

[22] Claus Weitkamp,Lidar, "Ranged-Resolved Optical Remote Sensing of the Atmosphere.", Springer", pp112, 2005

[23] Hamamasu, HAMAMATSU PHOTONICS K.K., Electron Tube Center http://kr.ic-on-line.cn/IOL_R2693P/pdfView/1300337.htm

[24] Hamamatsu Corp., "An Introduction to Detectors.", *The Photonics Design And Applications Handbook,* H112-H116, 1998

[25] Fredrick G. Fernald, Benjamin M. Herman and John A. Reagan, "Determination of aerosol height distribution by Lidar.", *Journal of Applied Meteorology*, pp482-489,1972

[26] Fredrick G. Fernald, "Analysis of atmospheric lidar observations: some comments.", *Applied Optics*, pp652-653, 1984

[27] Claus Weitkamp,Lidar, "Ranged-Resolved Optical Remote Sensing of the Atmosphere.", Springer", pp246, 2005

[28] Claus Weitkamp,Lidar, "Ranged-Resolved Optical Remote Sensing of the Atmosphere.", Springer", pp257, 2005

The nitrogen Raman channel is put to use to retrieve the lidar ratio and the optical depth of a low cloud. Two methods are used to obtain and compare the cloud optical depth. They are Raman retrieval method and Mie retrieval method.

4.1 Raman retrieval

To calculate the extinction coefficients,

$$\alpha_p(\lambda_0, z) = \frac{1}{1+(\lambda_N/\lambda_0)^{-k}} \left\{ \frac{d}{dz} \ln\left[\frac{N(z)}{P(\lambda_N, z) z^2} \right] - \alpha_m(\lambda_0, z)\left[1+(\lambda_N/\lambda_0)^{-4}\right] \right\} \quad (4.1)$$

The Angstrom coefficient k is taken to be 1.2 for aerosol and 0 for cloud [10, 11].

α_p is changed to α_C for the cloud. Integrating the Raman-retrieved extinction profile from cloud base z_b to top z_t gives the cloud optical depth,

$$\tau_C = \int_{z_b}^{z_t} \alpha_C(z)\, dz \quad (4.2)$$

This is the Raman method for the determination of the optical depth.

To calculate the backscatter coefficients, equation (3.36) is repeated for convenience,

$$R(\lambda_0, z) = \frac{\beta_p(\lambda_0, z) + \beta_m(\lambda_0, z)}{\beta_m(\lambda_0, z)}$$

$$= \frac{P(\lambda_0, z)}{P(\lambda_N, z)} R\left(\lambda_o, z_{ref}\right) \frac{P(\lambda_{N2}, z_{ref})}{P(\lambda_0, z_{ref})} \frac{\exp\left\{-\int_z^{z_{ref}} [\alpha_p(\lambda_0, z') + \alpha_m(\lambda_0, z')]dz'\right\}}{\exp\left\{-\int_z^{z_{ref}} [\alpha_p(\lambda_N, z') + \alpha_m(\lambda_N, z')]dz'\right\}} \tag{4.3}$$

4.2 Mie retrieval

This is essentially a method Young applied to retrieve the optical thickness for a thin cirrus cloud [1]. In this method, the normalized lidar return from the molecular profile for the atmosphere is calculated first,

$$P_m(\lambda_0, z) = \beta_m(\lambda_0, z) \times T_m^{\,2}(\lambda_0, z) / z^2 \tag{4.4}$$

Then lidar return from the region below cloud is regressed against the molecular profile to give,

$$m_{bot} = CT_a^{\,2}(z_0, z_1)\overline{R}_{bot}(z_1, z_2) \tag{4.5}$$

where $\overline{R}_{bot}$ is the average of the aerosol backscatter ratio in the regression region below cloud.

Similarly, lidar return from the region above cloud is regressed against the molecular profile to give,

$$m_{top} = CT_a^{\,2}(z_0, z_1)\overline{R}_{top}(z_3, z_4)T_c^{\,2} \tag{4.6}$$

where $\overline{R}_{top}$ is the average of the aerosol scattering ratio in the regression region above cloud.

The aerosol attenuation in each regressed window range is ignored. This window is variable dependent on cloud height, aerosol variability and SNR, but it has been found that regression windows between 0.1~0.2 km are suitable where aerosol scattering ratios generally vary little.

Clearly, the two equations are combined into one to give the optical depth of the layer lying between the two regions for the cloud,

$$\tau_C = \frac{1}{2}\left[\log\left(m_{bot}/m_{top}\right) - \log\left(\overline{R}_{bot}/\overline{R}_{top}\right)\right] \tag{4.7}$$

where $\log\left(\overline{R}_{bot}/\overline{R}_{top}\right)$ is called the aerosol correction factor and the cloud optical depth uncertainty is given by:

$$\delta\tau_C = \frac{1}{2}\sqrt{\left(\frac{\delta m_{bot}}{m_{bot}}\right)^2 + \left(\frac{\delta m_{top}}{m_{top}}\right)^2 + \left(\frac{\delta \overline{R}_{bot}}{\overline{R}_{bot}}\right)^2 + \left(\frac{\delta \overline{R}_{top}}{\overline{R}_{top}}\right)^2} \tag{4.8}$$

This Mie retrieval method is especially accurate for high and thin cirrus because nearly free-aerosol layers exist below and above the cloud layer so that aerosol influence can be ignored.

On the other hand, aerosol loading is usually high at lower altitudes, so it is necessary to estimate the ratio of the two aerosol scattering ratios $\overline{R}_{bot}/\overline{R}_{top}$ in the aerosol correction factor expression, $\log\left(\overline{R}_{bot}/\overline{R}_{top}\right)$. This ratio can be obtained from the

combined Raman-Mie signals in Eq. (4.3) and it is quite insensitive to the reference altitude z_{ref} and the lidar ratio. Due to poor signal penetration for the Raman channel above the cloud, it is preferable to perform this analysis in clear sky patches, assuming the vertical structure of the atmosphere is fairly stable over short periods in order to infer the aerosol scattering ratio $\overline{R}_{bot}/\overline{R}_{top}$ over the cloud period. This situation is readily available for periods of clouds with low optical thickness where clear sky patches are numerous. This is a unique advantage of using a Raman-Mie lidar together for the retrieval of the aerosol scattering ratio. A retrieval by the Mie lidar alone depends strongly on the lidar ratio and the reference value z_{ref} .

In either method, the cloud base and top must be located. A wavelet transform was applied to the Mie lidar return to determine them [2,3].

4.3 Result and discussion

4.3.1 Cloud profiles

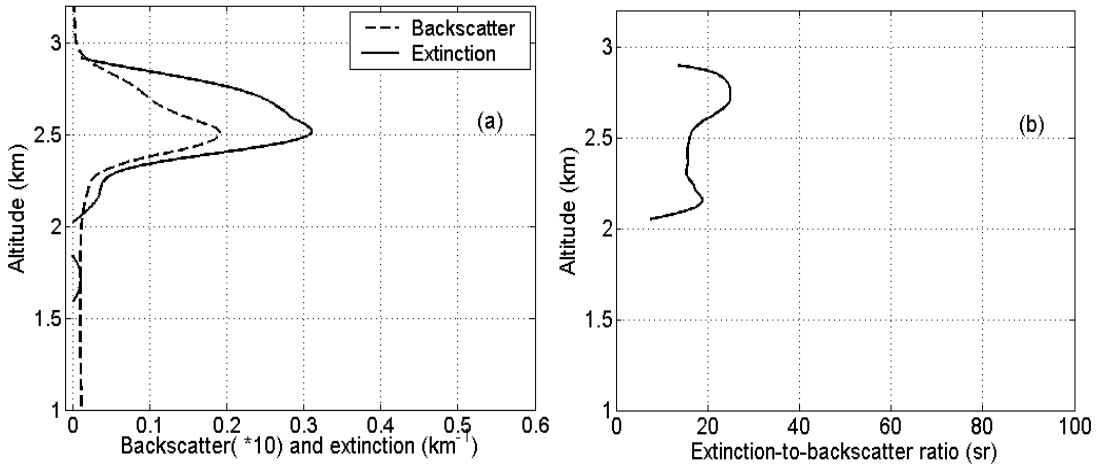

Figure 4.1: (a) Cloud backscatter, extinction coefficient and (b) their ratio at 355-nm on March 15, 2006

To illustrate the capability of the Raman Lidar to retrieve cloud properties in the day time, Figure 4.1 (a) and (b) each shows a representative profile of a cloud optical parameter obtained on March 15, 2006. A cloud layer clearly appears in the backscatter profile between 2~3 km. Raman processing allows us to calculate the profile of the lidar ratios. Their values are significantly smaller than those for aerosol with a mean of 18.6 sr at 355nm with a standard deviation of 3.9 sr. This value is comparable with previous observations and numerical analysis [4,5] where the extinction and backscattering coefficients are computed using a normalized gamma distribution of cloud droplet sizes. The calculated value of the lidar ratio based on this Lorentz Mie model is 18.9±0.4 sr at 355 nm [4].

4. 3.2 Determination of the cloud optical depth (COD) by regression of elastic returns

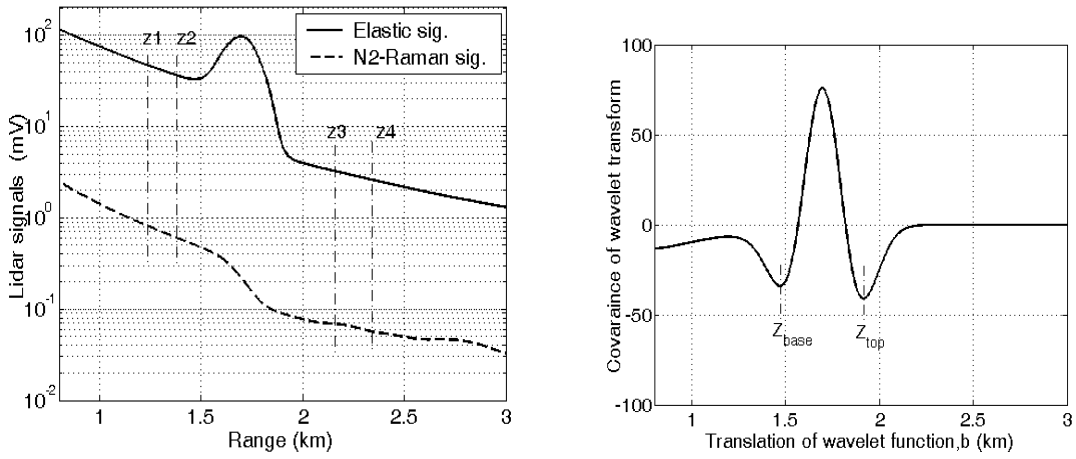

Figure 4.2: (a) Elastic- and N_2-Raman scattering signals, (b) covariance of wavelet transform on April 6, 2006

Figure 4.2 (a) shows the background noise subtracted elastic- and N_2-Raman scattering returns on April 6, 2006. A 10 minute data average is used to reduce the noise. Elastic returns indicate a cloud layer over 1.5~1.9-km altitude, while the N_2-Raman signal shows a large gradient caused by cloud attenuation in this range. In the figure, the range intervals used in the regression are also marked both below and above the cloud for subsequent Mie-retrieval of cloud optical depth. Figure 4.2 (b) plots the covariance of wavelet transform of elastic returns. Clearly, cloud base and top are well identified by the minimal values of covariance.

4.3.3.1 Retrieval with aerosol correction factor computed from the Raman Mie channel

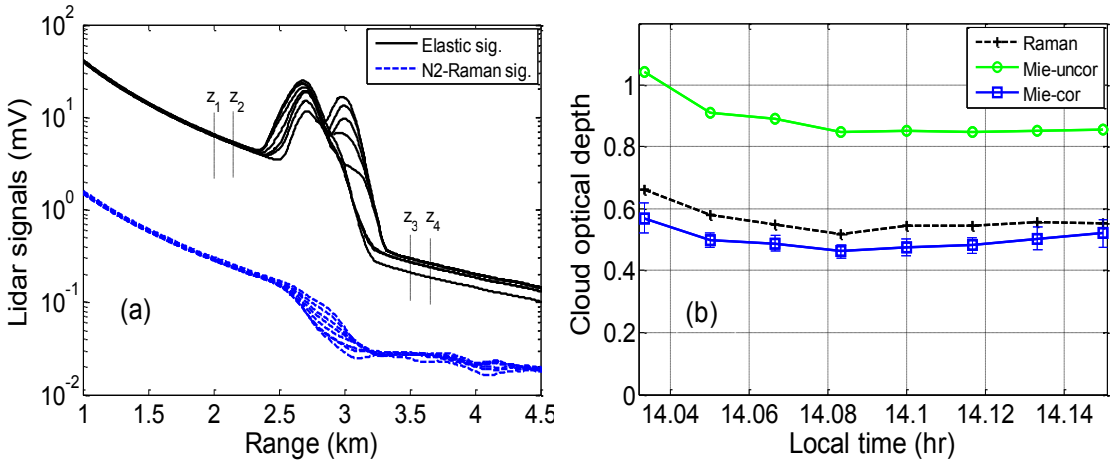

Figure 4.3: (a) Elastic and N_2-Raman scattering signals, (b) comparison of cloud optical depth retrieval on June 16, 2006. Raman: Raman retrieval; Mie-uncor: Mie retrieval without aerosol correction; Mie-cor: Mie retrieval with aerosol correction.

Figure 4.3 shows details in the regression calculation for the cloud optical depth on June 16, 2006 for different times. Eight vertical profiles are plotted in Figure 4.3 (a), which indicates a cloud in the range of 2.3~3.3 km. In these cases, high aerosol loading appears below the cloud with mean aerosol backscatter ratios ranging from 2.13~2.76 Aerosol loading above the cloud is found to vary with a scattering ratio in the range of 1.054~1.063 These values are obtained by the N_2 -Raman Mie signals applied to eq.(4.3)

Figure 4.4 (b) plots cloud optical depths derived independently using both Raman retrieval and elastic retrieval methods. It is seen clearly that without correction for the aerosol scattering ratio, a systematic and significant overestimate of optical depth is made using the Mie retrieval method (symbol 'o'). After suitably correcting for the aerosols, the Mie retrieval (symbol '□') shows a good agreement with that of Raman retrieval.

4.3.2.2 Comparison of retrievals with aerosol correction factor computed from both the Raman-Mie and elastic channel

To highlight the importance of this correction factor obtained by the Raman-Mie signals, especially below the cloud, the optical depth retrieval is computed again by a correction factor obtained from the elastic signal instead which assumes the knowledge of a lidar ratio. The result of this retrieval relative to the combined Raman-Mie approach to correct for the aerosol ratio is given in Figure 4.4 In this figure, 'Mie-uncor' refers to Mie retrieval without aerosol correction, 'Mie-Cor-1' refers to the case where only the elastic channel was used to retrieve the aerosol correction factor while 'Mie-Cor-2' refers

to the case where the combined Raman-Mie signals are used for the aerosol correction. Clearly, a significant improvement is obtained when both Raman and Mie channels are used together.

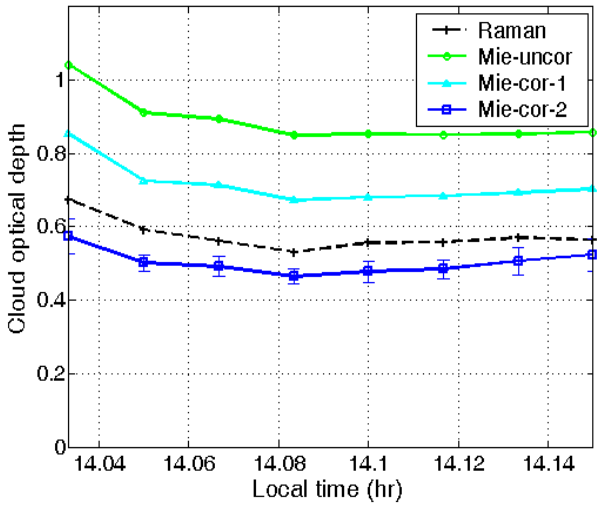

Figure 4.4: Comparison of cloud optical depth retrievals. Mie-uncor: Mie retrieval without aerosol correction; Mie-cor-1: Mie retrieval with aerosol correction from only the elastic returns; Mie-cor-2: Mie retrieval with aerosol correction from the combined Raman-elastic return.

A high optical depth of the cloud can present a difficulty. It will significantly attenuate the lidar signal, degrade the retrieval particularly when the N_2-Raman profile is used. In addition, the strong background signal noise in the daytime will significantly reduce the signal to noise ratio. These results are seen Figure 4.5 (a) which shows that for sufficiently high COD, unlike elastic return, the N_2-Raman signal degrades below the noise threshold prior to the cloud threshold. This results in a clear underestimation of COD using the Raman return technique for high COD as illustrated in Figure 4.5 (b). In this situation, an aerosol backscatter ratio profile in less cloudy conditions is derived from

the Raman-Mie returns for the aerosol correction in Mie-retrieval. It should be pointed out that if the degraded signal is still used to calculate extinction coefficient, the error may not always be biased low but can lead to noise induced overestimates of extinction.

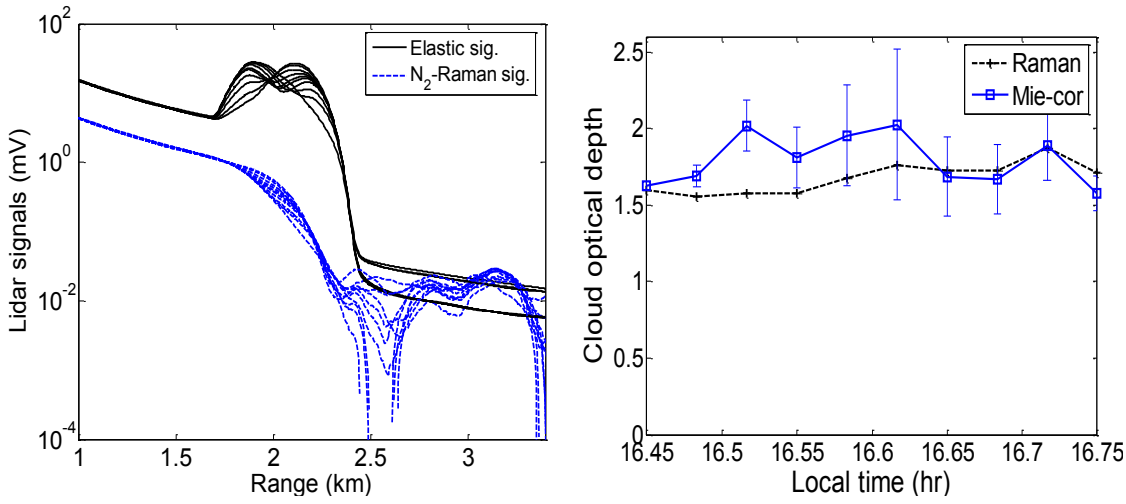

Figure 4.5: (a) N_2-Raman and elastic scattering signal penetration potential for relatively high COD illustrating the degradation of the Raman signal within cloud, (b) Resulting COD comparison

4.3.3 Comparisons of COD between Raman- and Mie-retrievals

A representative example (March 15, 2006) for a long time interval in which the COD undergoes significant change is shown in Figure 4.6 (a) to (d). A cloud between 1.8 to 3 km is demarked on the range scaled return. Complementary radiosonde data identified the cloud to be predominately water phased. As Figure 4.6 (b) shows, after aerosol contribution is eliminated, the two retrievals are nearly coincident with each other and the cloud optical depth at 355nm varies from 0.1 to 1.7 A good correlation between the retrievals is seen in Figure 4.6 (c) with R^2=0.959. However, discrepancies become

larger at higher CODs as expected. The mean and standard deviation of lidar ratios in the cloud are shown in Figure 4.6 (d) It is observed that lidar ratios mostly fluctuate about 20sr with a standard deviation of 6.3sr, indicative of the dominance of the water phase in the cloud.

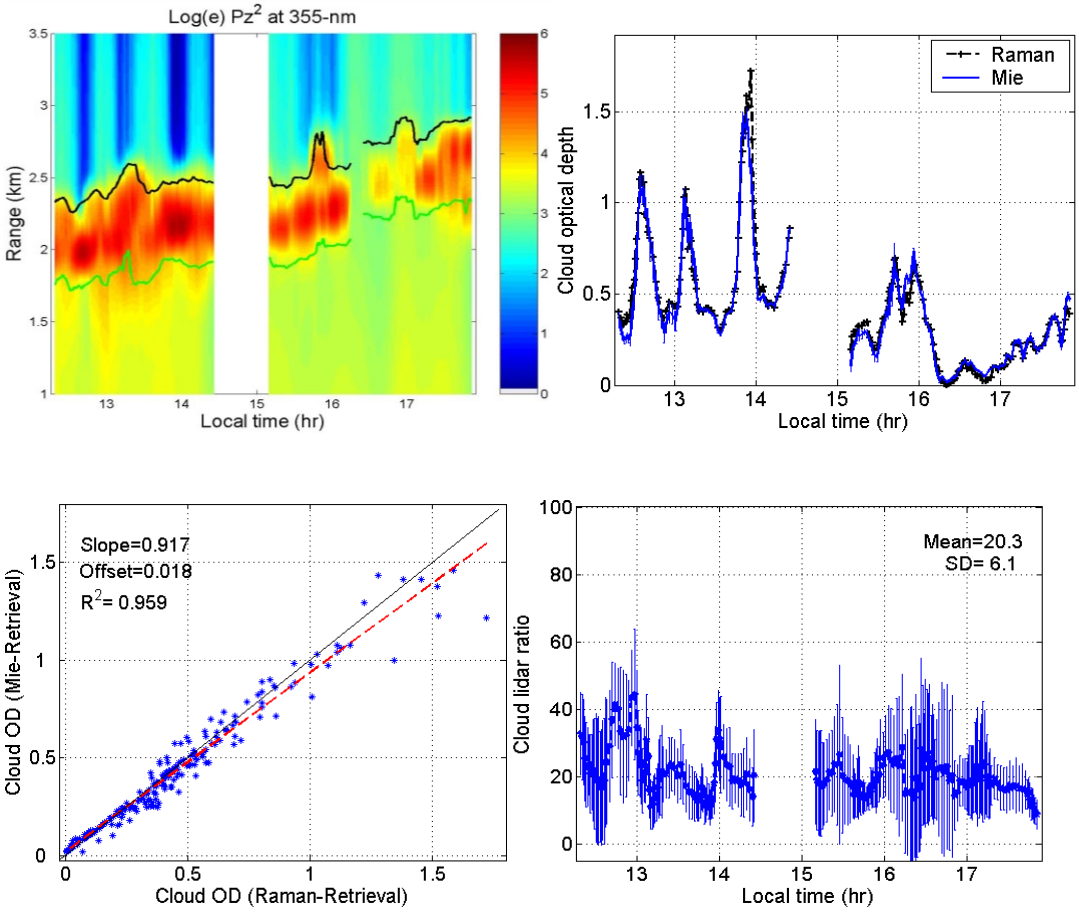

Figure 4.6: (a) Log range-square corrected elastic returns, (b) Raman and Mie retrieved cloud optical depths, (c) their correlation, and (d) average and standard deviation of lidar ratios in clouds on March 15, 2006

To assess this method over a larger data sample, a data set of 17 days with a total of 2042 data pairs are statistically analyzed. The results are shown in Figure 4.7(a) which

illustrates a strong correlation of R^2=0.94 with a regression slope close to 1.0 Clearly, data pairs begin to scatter at larger CODs. In Figure 4.7 (b), their mean values of the absolute differences are calculated as a function of COD. Over a wide range of COD (i.e. 0.3 to 1.5), fractional errors are on the order of 10% but the error gets larger as COD goes higher than 1.5

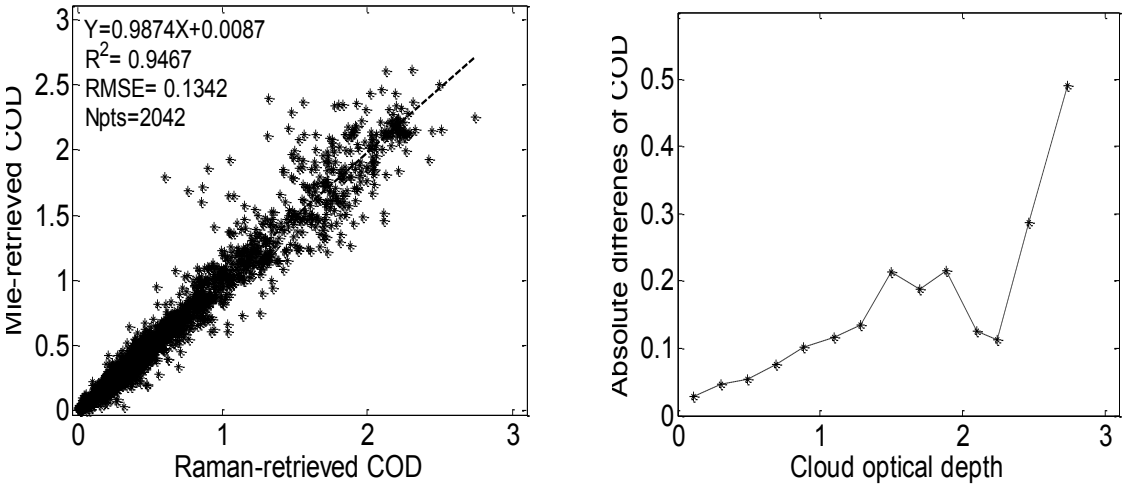

Figure 4.7: (a) Correlation and (b) absolute differences among Raman- and Mie-retrieved cloud optical depths

4.3.4 Varied lidar ratios of low cloud: implication for droplet size

A strong agreement of the COD retrieval provides an independent validation on the accuracy of both the extinction and backscatter vertical profiles within the cloud which allows us to estimate the cloud parameters of interest. Figure 4.8 plots a group of cloud optical parameters, including backscatter, extinction and lidar ratio over the cloud cross section. In this case, Raman retrieved-CODs vary over 0.1~0.3 Both N_2-Raman and elastic scattering returns can penetrate the cloud layer well so that the lidar-ratio can

be derived. If the cloud was dominated by ice crystals, a single channel lidar ratio would not be able to estimate the size properties. However, if the cloud is in the water phase, a water drop model based on a normalized Gamma size distribution of spherical particles [4,6] can be developed which allows us to roughly connect the lidar ratio to an effective droplet mean diameter. The model calculated lidar ratios versus water droplet effective diameters are shown in Figure 4.8 (b) with the mode width parameter μ given the value of 2. Clearly, lidar ratios show a strong dependence on the effective diameters for small cloud droplets (<3 μm), and then become fairly stable for droplet sizes of 3~20 μm with a value of 20 sr. This agrees with the lidar ratio obtained in the dense portions of the cloud, which confirms the basic assumption that the cloud is primarily in water phase. It also appears that the lidar ratio increases markedly towards the upper boundaries and this implies the presence of smaller droplets such as would be associated either with new condensation or evaporation of the droplets near the cloud edge. Additional improvements in the range of droplet size retrieval can be obtained if we include long wavelength backscatter as well as to be able to more accurately distinguish ice from water phase. In particular, Eberhard [6] has discussed a similar approach to determine the droplet size according to the lidar ratio at a long laser wavelength (~10.6μm). Further analysis is needed to explore this interesting phenomenon, which would be of great interest for the microphysical and dynamical processes of low clouds.

In order to ensure that all measurements were taken in the cloud interior in evaluating the lidar ratio, histograms of particle backscatter coefficients are plotted in Figure 4.8 (c) The dotted curve shows the data from 1.9 to 3.1 km which include aerosol

and cloud particles (see Figure 4.6 (a) for cloud range). A bimodal distribution is seen to represent the presence of aerosols and cloud. The solid curve is a histogram of backscatters over the 2.6~2.8 km range, which is definitely above the cloud threshold.

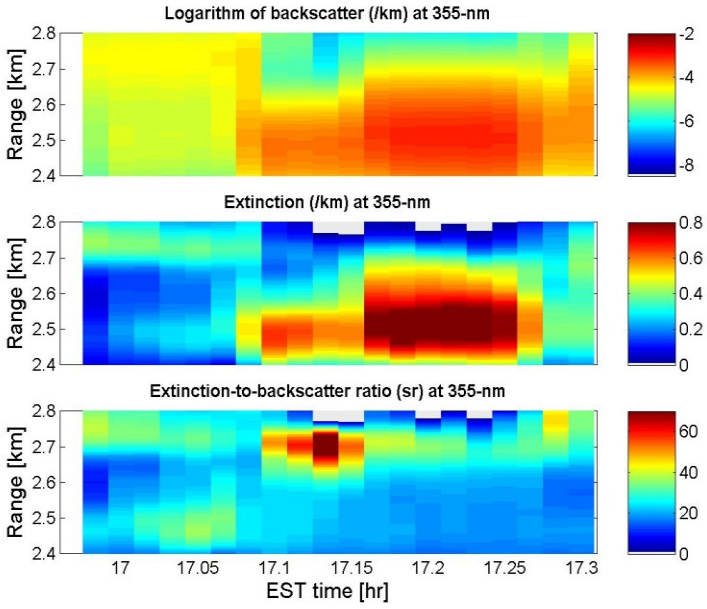

Figure 4.8: (a) Cloud backscatter, extinction and extinction-to-backscatter ratio on March 15, 2006

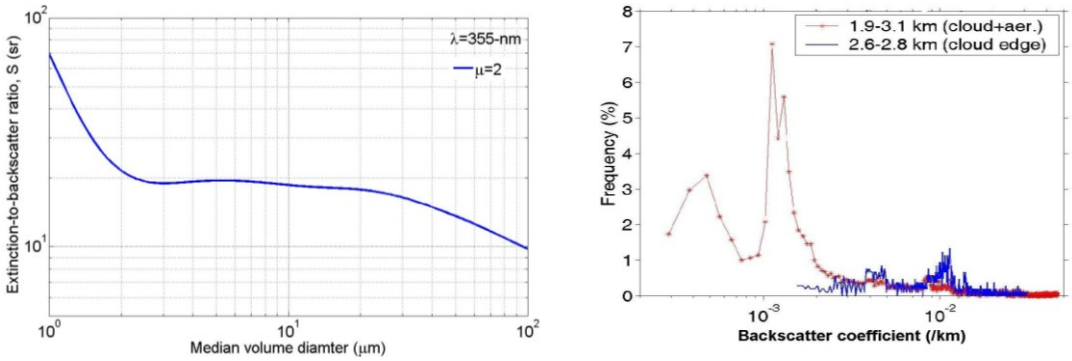

Figure 4.8: (b) Lidar ratio versus particle effective diameter
(c) Histogram of backscatter coefficients of aerosol and cloud on March15, 2006

Summary

The retrievals of low altitude optically thin clouds were analyzed using both the N_2-Raman and elastic scattering return approaches. It has been illustrated that the elastic return regression approach would overestimate cloud optical depths unless the aerosol correction term is accurately estimated. In particular, it has been shown that using the combined Raman-Mie returns obtained for nearby clear sky patches, we can better estimate the aerosol backscatter ratio profile which results in a significant improvement in the COD retrieval. Validation of the Raman retrieved COD with the retrieval using the combined Raman-Mie returns also enables us to assess the quality of our backscatter and extinction vertical profiles in the cloud. From these measurements it was possible to provide 3D profile maps of the lidar ratio. In particular, its statistics has a mean value near 20sr which was found to be consistent with a commonly used water phase cloud model. Within the water phase assumption, the lidar ratio profiles were used for preliminary sizing of effective cloud droplet sizes which allowed us to map areas within the cloud with small condensing droplets.

In a statistical comparison, the cloud optical depth retrieved from the Mie returns regression method with aerosol correction and that retrieved by the direct Raman method show excellent agreement, a strong correlation value of R^2=0.94 and a regressed linear slope of 0.98 is observed. In general, errors between the two methods are less than 10%. However, it was also shown that the direct Raman method becomes less accurate at high CODs since the N_2-Raman signals are attenuated by the cloud more severely than the elastic signal is. This is illustrated by the fact that discrepancies between the methods

grow larger when the cloud optical depth is greater than a certain value. Finally, multiple scattering effects on deriving cloud optical depth were calculated for the optical parameters relevant to this study, and indicate that corrections on the order of 18% must be made. This influence can be reduced largely by using a smaller receiver field of view (RFOV). Unfortunately, since both optical depth approaches are affected by multiple scattering effects, no independent correction of the multiple scattering can be made.

In summary, it was found that the Mie returns regression method provides a better COD measurement for larger cloud optical depths (>1.5 in this study) although the Raman extinction method works well for COD less than this value. This value of the COD is specific to the transmitted power and is not an absolute value for all cases. However, the Mie method depends critically on the ability to estimate aerosols beneath the cloud layer which can be accomplished best using a combined Raman-Mie lidar measurement. It is also expected that determination of the cloud phase and subsequently cloud droplet sizes within the water phase will also be significantly improved using a properly calibrated 1064nm backscatter lidar channel.

REFERENCES

[1] S. A. Young, "Analysis of lidar backscatter profiles in optical thin clouds," *Appl.Opt*. 34, 7019-7030, 1995

[2] Y. Morille, M. Haeffelin, P. Drobinski, J. Pelon, "STRAT: an automated algorithm to retrieve the vertical structure of the atmosphere from single channel lidar data," *J. Atmos. Oceanic. Technol*. 24, 761-775, 2007

[3] K. J. Davis, N. Gamageb, C. R. Hagelbergc, C. Kiemled, D. H. Lenschowe, P. P. Sullivane, "An objective method for deriving atmospheric structure from airborne lidar observations*," J. Atmos. Oceanic Technol*. 17, 1455–1468, 2000

[4] E. J. O'Connor, A.J. Illingworth and R.J. Hogan, "A technique for autocalibration of cloud lidar," *J. Atmos. Ocean. Tech*. 21(5), 777-778, 2004

[5] R. G. Pinnick, S. G. Jennings, P. Chýlek, C. Ham, and W. T. Grandy Jr., "Backscatter and extinction in water cloud," J. Geophys. Res. 88 (11), 6787-6796, 1983

[6] W. L. Eberhard, "CO_2 lidar technique for observing characteristic drop size in water cloud," *IEEE Trans. Geosci Remote Sensing*, 31 (1), 57-63, 1993

[7] E. W. Eloranta, "A practical model for the calculation of multiply scattered lidar returns," *Appl. Opt*. 37, 2464-2472,1998

[8] U. Wandinger, "Multiple-scattering influence on extinction and backscatter coefficient measurements with Raman and High-Spectral-Resolution Lidars," *Appl. Opt*. 37, 417-427, 1998

[9] R. J. Hogan, “Fast approximate calculation of multiply scattered lidar returns,” *Appl. Opt*. 45, 5984-5992, 2006

[10] A. Ansmann, U. Wandinger, M. Riebesell, C. Weitkamp, and W. Michaelis, “Independent measurement of extinction and backscatter profiles in cirrus clouds using a combined Raman elastic-backscatter lidar,” *Appl. Opt*. 31, 7113-7131, 1992

[11] R. A. Ferrare, S. H. Melfi, D. N. Whiteman, K. D. Evans, and R. Leifer, “Raman lidar measurements of aerosol extinction and backscattering. 1. Methods and comparisons,” *J. Geophys. Res*. 103, 19663–19672, 1998

Clouds are white in the visible region and scatter all wavelengths indiscriminately proportional to λ^0 while aerosol particles have a typical dependence of λ^{-1}. Therefore, clouds are more readily seen against aerosol and molecular scatterers by the near infrared channel. The sensitivity of the *1064nm* channel is limited by the inherent detector noise. Its signal to noise ratio is not as high as the $532nm$ channel so it is not used to retrieve atmospheric parameters.

5.1 Aerosol backscatter ratio

Because of the uncertainty caused by the wavelength dependence of the backscatter cross sections, the aerosol backscatter ratio depends on the wavelength of the incident beam. This ratio quantifies the aerosol to molecular backscattering,

$$R = 1 + \frac{\beta^{aer}}{\beta^{mol}} \tag{5.1}$$

$\frac{\beta^{aer}}{\beta^{mol}}$ is the aerosol to molecular backscatter ratio.

Forming the ratio of this quantity at the two wavelengths, 532nm and 1064nm,

$$\frac{R_{532} - 1}{R_{1064} - 1} = \frac{\beta_{532}^{aer}}{\beta_{532}^{mol}} \times \frac{\beta_{1064}^{mol}}{\beta_{1064}^{aer}} \tag{5.2}$$

Using the simple approximation of the wavelength dependence of atmospheric particulate scattering, the Angstrom coefficient defined by,

$$\beta = \frac{const}{\lambda^k} \tag{5.3}$$

k is a constant that takes on values between 0 and 4 according to the size of the scattering particle. For molecular scattering, $k = 4$

which is the limiting case of Rayleigh scattering responsible for a blue sky.

$$\frac{R_{532} - 1}{R_{1064} - 1} = \frac{\beta_{532}^{aer}}{\beta_{532}^{mol}} \times \frac{\beta_{1064}^{mol}}{\beta_{1064}^{aer}} = \frac{\beta_{532}^{aer}}{\beta_{1064}^{aer}} \times \frac{\beta_{1064}^{mol}}{\beta_{532}^{mol}} \tag{5.4}$$

$$= \left(\frac{1064}{532}\right)^u \times \left(\frac{532}{1064}\right)^4 = 2^{k-4} \tag{5.5}$$

For large fog and cloud particles, k is often assumed to be 0 which means that there is no wavelength dependence in the scattering process.

Rearranging the above equation,

$$16\left(R_{532} - 1\right) = R_{1064} - 1 \tag{5.6}$$

In literature R_{532} is often assumed to be 1.1 so that $16(0.1) = R_{1064} - 1$

$$1.6 = \frac{\beta_{1064}^{aer}}{\beta_{1064}^{mol}} \tag{5.7}$$

i.e. from the same scattering particles, a 10% uncertainty in aerosol scattering at 532nm corresponds to 160% uncertainty at 1064nm.

Even for aerosol particles smaller than cloud droplets, say $k = 1$, the uncertainty in aerosol backscatter at 1064nm is still calculated to be 80%

5.2 Cloud Properties

Some of the optical properties of cloud include transmission, lidar ratio, optical depth, depoloarization, multiple scattering effects and cloud heights. Cloud heights and the boundaries of a cloud vary according to definitions. The maximum return or alternatively the centroid can be defined as the height of the cloud [9].

$$z_{mid} = \int_{z_{base}}^{z_{top}} z' P(z') dz' \Big/ \int_{z_{base}}^{z_{top}} P(z') dz' \tag{5.8}$$

The problem of having to find the base and occasionally the top heights of a cloud is frequently encountered. For a dense optically thick cloud, the lidar signal is attenuated by particulates in the cloud before it emerges the cloud top with a negligible fraction of its incident power. Even the concept of a physical sharp boundary does not apply here as the laser beam does not emerge the 'cloud top' abruptly with a drastic drop in the signal level. When the boundary is less sharply defined as that for a cloud as the boundary of the planetary layer, thresholding the signal is difficult to identify the boundary especially when there are shot-to-shot power fluctuations. Instead the wavelets transform is applied

to locate the boundaries. It is multi-scale and can focus on larger spatial scales to minimize the influence of incoherent instrument noise.

The Haar function is defined by,

$$h\left(\frac{z-b}{a}\right)=\begin{cases}-1 & b-a/2\le z\le b\\ 1 & b\le z\le b+a/2\\ 0 & elsewhere\end{cases} \tag{5.9}$$

The convolution or localized transform of the function and the backscatter or returns profile $f(z)$ is called the covariance transform by Gamage and Hagelberg [10], where *a* is the dilation and *b* is the translation parameter.

$$W_f(a,b)=a^{-1}\int_{z_b}^{z_t} f(z)\,h\left(\frac{z-b}{a}\right)dz \tag{5.10}$$

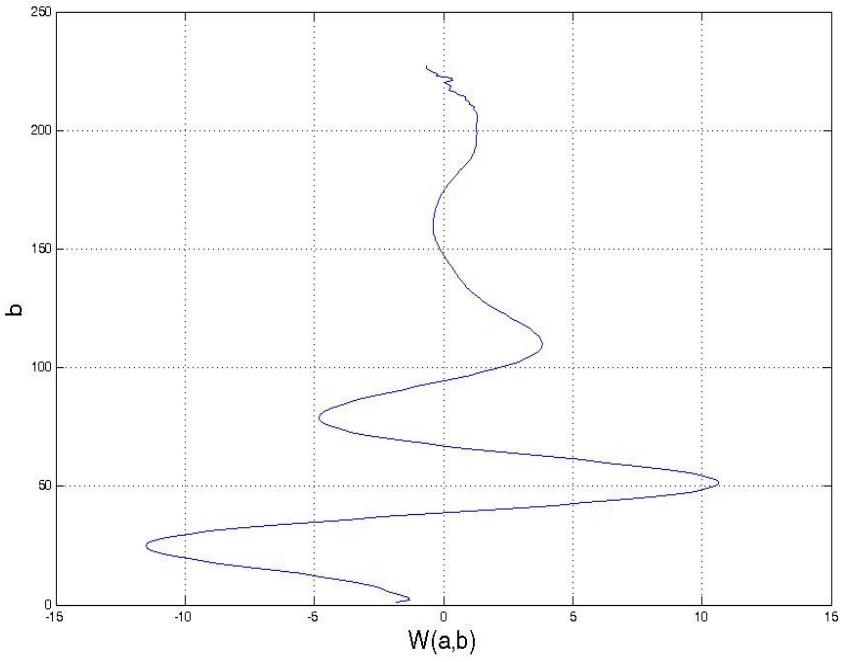

Figure 5.1: Profile of covariance transform for a specific value of 'a'

In its discrete form, this is equivalent to the wavelet coefficients,

$d_{jk} = \left\langle v(t) \,|\, \psi_{jk}(t) \right\rangle$ with a normalization factor and assumes a distinct value for a specific dilation a, indexed j

Various atmospheric structure boundaries can be located by examining the extrema. The variance of this covariance transform with the Haar function reveals the sharp boundary transition between the aerosol loaded region and the free troposphere above it.

$$D^2(a) = \int_{z_b}^{z_t} \left[W_f(a,b) \right]^2 db \tag{5.11}$$

$\left[W_f(a,b) \right]^2$ is similar to a power density spectrum. The total power is the filtered (convoluted) signal integrated over the translation variable at a particular dilation.

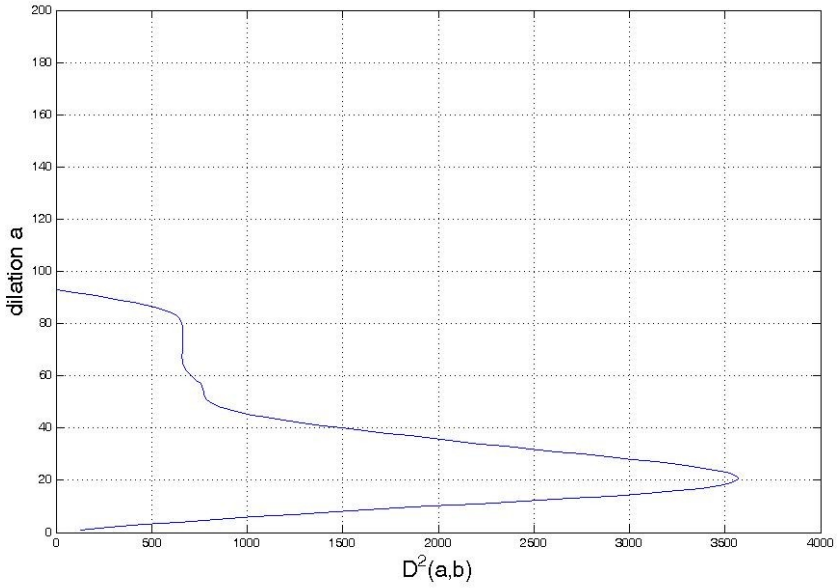

Figure 5.2: Variance of the covariance transform

The plot above is a one minute data profile from the following day (May31 2006) where the boundaries are marked by carrying out the transform procedure for the entire time series. The extrema in the covariance transforms corresponding to the boundaries shown.

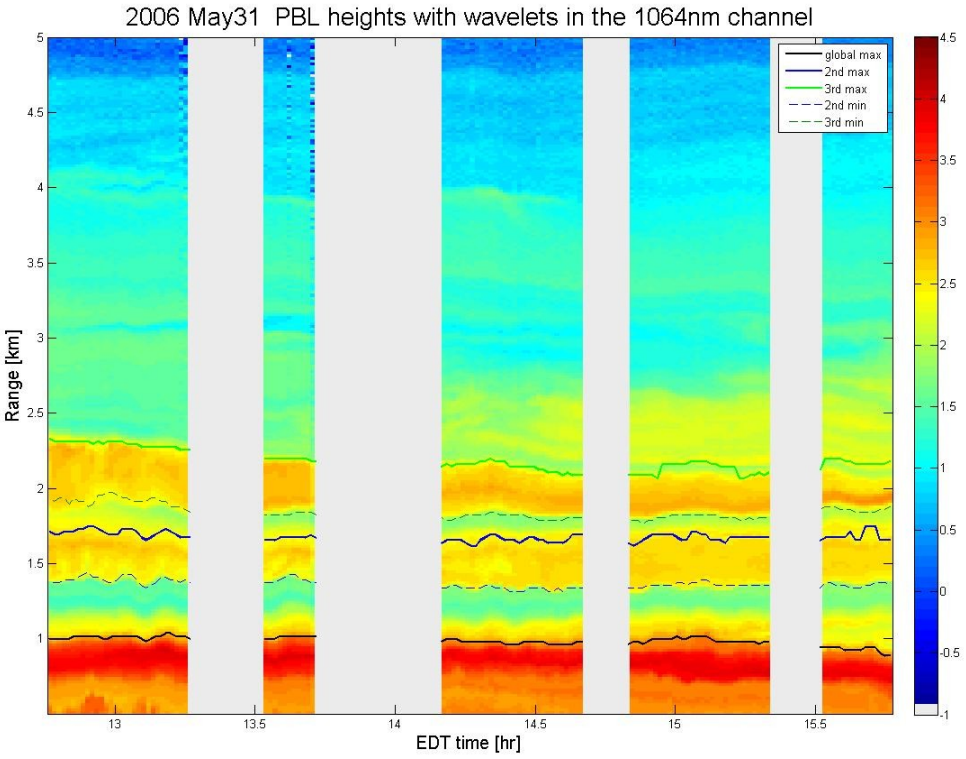

Figure 5.3: Planetary and aerosol layer boundaries

The region where the aerosol backscattering coefficient sharply decreases and the potential temperature lapse rate varies has been determined as the top of the PBL.

5.3 Mulitple scattering

The multiple scattering effect has been recognized for a long time. Since the early *1970's*, a variety of multiple scattering models for lidar has been developed. Measurements on the reflectance of clouds led Milton to believe that multiple scattering was responsible for its lower than expected value as obtained by Kattawar also in his theoretical calculation for the nearest scenario [5]. These calculations indicate an observable difference of the multiple scattering effect. Platt in his observations of various properties in cirrus clouds, emissivity, lidar ratio etc., concluded that the optical depth was reduced below the true value and modelled it as radiation being scattered out of the laser beam and returned to the receiver by secondary or higher order processes [4]. For this he included a constant η in the evaluation of the observed backscatter to account for the discrepancy,

$$\beta_{obs}(\pi, z) = \beta_{true}(\pi, z) \exp\left[-\int_{z_0}^{z} 2\eta\sigma(z') \, dz' \right] \tag{5.12}$$

Eloranta derived an expression of the power incident on the receiver for unploarized light. It is based on the approximation that half of the total energy scattered by cloud droplets is deflected into a narrow diffraction peak, and with small angle approximations.

$$P = P_0 \frac{c\Delta t}{2} \omega_r \beta \frac{\mathrm{P}_1(\pi)}{4\pi} \exp(-2\tau) \left[1 + \tau + \frac{(\tau)^2}{2!} + ... \right] \tag{5.13}$$

Katsev et al. used the Fourier space solution of the radative transfer equation with quasi small angle approximations to derive an analytical solution of the multiple scattering lidar problem [1]. The mathematics in it is laborious. In the Monte Carlo methods, a more convenient alternative represents the radiance function in the transfer equation by a large number of trajectories. The average from many such realizations of trajectories result in the desirable quantity such as the radiant flux entering a receiver in this application. Since radiative transfer processes are stochastic in nature, most quantities in transfer theory can be interpreted as probabilities. An example of this is the extinction coefficient, the reciprocal of which is the photon mean free path. In this application, the probabilities in defining the trajectories must be known.

1. the probability of scattering, α_s / α (5.14)

2. the probability of scattering from direction $\vec{n}$ to $\vec{n}$ within the solid angle $d\vec{n}$

$$prob\left(\vec{n} \rightarrow \vec{n}\right) d\vec{n} = p(t, \vec{x}, \vec{n}, \vec{n}) d\vec{n} \tag{5.15}$$

3. the probability that the free path length occurs between l and dl at position $\vec{x}$ in the new direction $\vec{n}$ of a photon before the next event occurs,

$$prob(l)\,dl = \alpha\left(t, \vec{x} + l\vec{n}\right) \exp\left[-\int_0^l \alpha\left(t, \vec{x} + s\vec{n}\right) ds\right] dl \tag{5.16}$$

The main advantages of the Monte Carlo method are possible separation of contributions by scattering order and few approximations are required. However, the probability of

photons scattered back in the receiver is very small due to the large forward scattering peak in the phase function. Sophisticated numerical techniques of variance reduction are used but proved insufficient due to the very small fields of view of receivers in lidar applications [2]

5.3.1 Calculation of multiple scattering

Along with the approximate expression above for the lidar return, Eloranta also derived in more exact form return expressions for polarized light from double scattered contribution in a homogeneous cloud of spherical particles [6]. Later a more general phenomenological approached was adopted for unpolarized light to arrive at a practical model of multiple scattering [3]. Expression for the two lowest orders of multiple scattering are given here.

$$\frac{P_2(R)}{P_1(R)} = \frac{\mathrm{P}_2(\pi,R)}{\mathrm{P}_1(\pi,R)}\left[1-\exp\left(-\frac{\rho_t^{\,2}}{\rho_l^{\,2}}\right)\right]^{-1}\left\{\tau-\int_{-d}^{d}\beta_s(x_1)\exp\left(-\frac{\rho_t^{\,2}R^2}{x_1^{\,2}\Theta_s^{\,2}(x_1)+\rho_l^{\,2}R^2}\right)dx_1\right\} \quad (5.17)$$

$$\begin{aligned}\frac{P_3(R)}{P_1(R)} &= \frac{\mathrm{P}_3(\pi,R)}{\mathrm{P}_1(\pi,R)}\left[1-\exp\left(-\frac{\rho_t^{\,2}}{\rho_l^{\,2}}\right)\right]^{-1} \\ &\times\left\{\tau-\int_{-d}^{d}\beta_s(x_1)\int_{x_1}^{d}\beta_s(x_2)\exp\left(-\frac{\rho_t^{\,2}R^2}{x_1^{\,2}\Theta_s^{\,2}(x_1)+x_2^{\,2}\Theta_s^{\,2}(x_2)+\rho_l^{\,2}R^2}\right)dx_1\,dx_2\right\}\end{aligned} \quad (5.18)$$

$P_n(R)$ is the signal intensity return from range R due to nth order scattering.

$\mathrm{P}_n(\pi,R)/\mathrm{P}_1(\pi,R)$ is the ratio of the phase function of the nth order scattering to that of a singly scattering in the backscatter direction.

With a more detailed knowledge of various fractions, $F(R)$ of multiple scattered photons, a correction of the optical depth can be incorporated into the lidar equation of single scattering. This is a range dependent correction factor while Platt's multiple scattering constant η can be thought of as an effective value for the entire range.

$$P_T(R) = C\frac{1}{R^2}\beta(R)\exp\left\{-2\left[1-\sum_n F(R)\right]\int_0^R \sigma(r)dr\right\} \tag{5.19}$$

Using this model and the code that accomplished it, the optical thickness of a dense cloud is calculated. Its thickness appears to be less when all light detected is interpreted as scattered back by singly scattered photons. Here is the influence of the scattering medium itself on the smaller perceived extinction value because of the large particles (compared with the wavelength) in the cloud. Together with a narrow field of view of most ground lidars, the backscattered signal detected constitutes primarily contributions from strong particle forward scattering, be it before or after the backscatter detection. This description of multiple scattering is consistent with the strong forward peak in the phase function for large scatterers. The receiver field of view (RFOV) is a part of the measurement geometry that also influences what value of extinction coefficient is measured. The larger the illuminated volume of scatterers, the larger is the multiple scattering effect. This is why the multiple scattering effect is more prominent for the space borne lidar than for the ground lidar because of its much larger distance from the volume of scatterers.

Often multiple scattering cannot be neglected when the field of view of the laser beam in the illuminated disk area is larger than the photons mean free path . As a matter of fact, this fact has been exploited in recent years to retrieve particle information on extinction, size, liquid water content etc. by multiple fields of view lidars, for instance by Bissonnette and Spinhirne [7].

Below shows the lower profile with larger optical depths which represent the true values through the cloud. However, the accuracy of the calculation depends strongly on inputs to the program, for instance, the profile resolution, model droplet size etc.

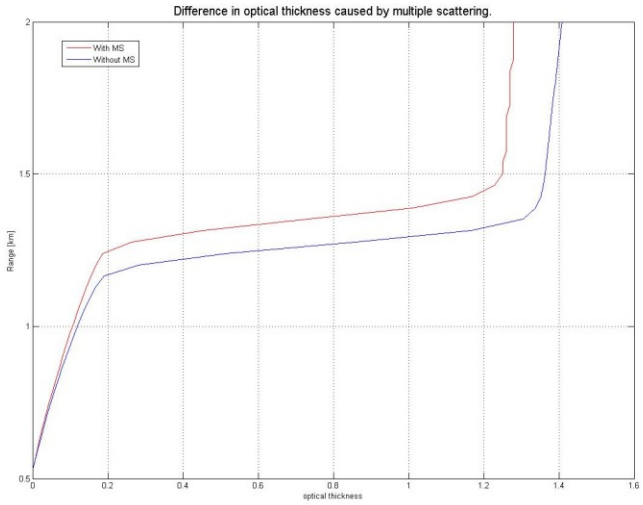

Figure 5.4: Optical depth difference caused by multiple scatttering in cloud.

Here is a table of multiple scattering values calculated by the same model.

Table 5.1. Percentage of multiple scattering influences on Raman-retrieved COD

	Re=3.5μm	5 μm	7.4 μm*	10 μm
	FOV=1.5 mrad			
COD=0.5	6.50%	10.40%	16.20%	21.60%
COD=1.2	7.80%	12.00%	18.00%	23.40%
	FOV=0.8 mrad			
COD=1.2	3.20%	5.20%	8.70%	12.30%

R: effective radius of cloud droplet; COD: cloud optical depth
*: MODIS retrieval value

REFERENCES

[1] I.L. Katsev, E.P.Zege, A.S. Prikhach, et al, *J. Opt. Soc. Am*., 14, 1338,1997

[2] Claus Weitkamp,"Lidar, Ranged-Resolved Optical Remote Sensing of the Atmosphere.", p61, 2005

[3] Edwin W. Eloranta, "Practical model for the calculation of multiply scattered lidar returns.", *Applied Optics*,Vol. 37,No. 12, 2464-2472,1998

[4] C.M.R.Platt, "Lidar and Radiometric Observations of Cirrus Clouds.",Volume 30, pp1191-1204,1973

[5] J. E. Milton, R. C. Anderson, and E. V. Browell, "Lidar Reflectance of Fair-Weather Cumulus Clouds at 0.903 μ", *Applied Optics*,Vol. 11, No. 3,pp697-698, 1972

[6] Edwin W. Eloranta, "Thesis: Calculation of Doubly scattered Lidar Returns. ", University of Wisconsin, 1972.

[7] Luc R. Bissonnette, Gilles Roy, Laurent Poutier, Stewart G. Cober, and George A. Isaac, "Multiple-scattering lidar retrieval method: tests on Monte Carlo simulations and comparisons with *in situ* measurements." *Applied Optics*,Vol. 41, No. 30, pp6307-6324, 2002

[8] Kenji Kawano, Tsutomu Kitoh,"Introduction to Optical Waveguide Analysis." Wiley, 2001

[9] Zongming Tao, M. Patrick McCormick, Dong Wu,, Zhaoyan Liu, and Mark A. Vaughan, "Measurements of cirrus cloud backscatter color ratio with a two-wavelength lidar.", 1478, *Applied Optics*,Vol. 47, No. 10,1478-1485,2008

[10] Gamage, N. and C. Hagelberg, "Detection and analysis of microfronts and associated coherent events using localized transforms.", J. *Atmos. Sci.*, 50, 750-756, 1993

Chapter 6: Calibration of lidar at 1064-nm channel using clouds and the ceilometer

Lidar calibration at the 1064nm channel is explored by using the low level water phase cloud and high cirrus cloud. Based on a known constant of the lidar ratio for the optically thick water cloud, the lidar calibration constant is estimated by integrating lidar returns from the cloud. By using wavelength independence of backscatter in cirrus cloud, the lidar constant is analyzed with the two wavelength signals ratio at 532nm and 1064nm after correcting for aerosol transmittance from the sunphotometer measurements.

The calibration constant is also determined by regressing lidar signals with calibrated ceilometer data in the low PBL. The results of the calibration constant by both methods are applied to calculate the aerosol optical depths and compared with those measured by the sunphotometer. The Angstrom exponents are calculated for two cases from the aerosol backscatter profiles at 1064nm and 532nm. Simulation results are included and the values of the calibration constant are tabulated.

6.1 INTRODUCTION

Calibration is important for the elastic scattering lidar, especially at the 1064-nm channel to quantify the aerosol backscatter or extinction coefficient profile. Conventional calibration method by normalizing lidar return signal to the molecular value in the upper troposphere [1, 2, 3] is difficult to apply to the *1064nm* channel because of the weak molecular interactions and small signal to noise ratio over there. As demonstrated by a simple calculation in the last chapter, reference value of aerosol backscatter ratio i.e. the

ratio of total backscatter to molecular backscatter, at *1064nm* usually has a much larger uncertainty than the ones at visible-UV wavelengths, *532-355 nm*. Therefore an arbitrary assumption of the aerosol backscatter ratio at *1064nm* as a far end boundary condition in the mid-upper troposphere will bring upon large errors in the aerosol retrieval. On the other hand, calculations involving the weak molecular scattering at the *1064nm* channel are often simplified by ignoring it; and the weak aerosol backscatter too in a clear sky. Once the elastic scattering lidar is calibrated, the aerosol backscatter coefficients can be estimated directly and from the lidar return. No complex inversion and corresponding assumptions are needed such as a constant of lidar ratio and a far end boundary or reference value for aerosols.

Lidar calibration methods with the horizontal or slant measurements have been analyzed, but they need to assume a homogenous atmosphere in the horizontal direction or have knowledge of independently measured scattering coefficients [4,5,6]. These approaches are not realistic to a vertically pointing lidar. A hard target with known reflectance has been applied to calibrate the lidar, however many additional measurements have to be made [7,8,9]. Even measurements of lidar efficiency with the conventional hard target method were consistently higher by a factor of two more or less than the ones with the aerosol calibration technique [8]. On the other hand, clouds can be applied to calibrate lidars. Optically thick water clouds are thought to be suitable for lidar calibration based on its known constant of the lidar ratio [10,11,1,13]. For a space borne lidar, the 1064nm channel is calibrated relative to the *532nm* total backscatter signal using cirrus clouds as targets while the *532nm* channel is calibrated with the molecular atmosphere in the stratosphere [14,15]. But the latter is difficult for the ground based

lidar in the daytime because lidar returns cannot reach the stratosphere and atmospheric attenuation needs to be corrected.

6.2 METHOLODGY AND MEASUREMENT

The lidar equation with only one atmospheric component considered, for instance, the other being negligible, is given by,

$$P(z) = \frac{C \times \beta_a(z) \times \exp(-2\tau_a(z))}{z^2}$$

$$= C \times \frac{\beta_a(z)}{z^2} \times \exp\left[-2\int_{z_0}^{z} \alpha_a(z')\,dz'\right] \qquad (6.1)$$

For a detailed discussion of and solutions to the lidar equation, the reader is referred to section 3 in Chapter 3.

6.2. 1. Calibration with low level water clouds

For the water phase cloud, the lidar ratio, namely extinction to backscatter ratio, is calculated with a normalized gamma size distribution of cloud droplets using Mie scattering theory. Figure (6.1) shows lidar ratios versus volume median diameters of droplets at wavelength *1064nm*. A constant of lidar ratio $S_c = \alpha_c(z)/\beta_c(z) \approx 18sr$ is shown over the wide range of droplet diameters (5~40 μm). In order to derive a relationship between the lidar return and the calibration constant, integrate the lidar equation through the cloud region to give,

$$\frac{1}{C}\int_{z_b}^{z_t}\left[P(z)z^2\right]dz=\int_{z_b}^{z_t}\left[\beta_c(z)\exp(-2\tau_c(z)\right]dz=\left[1-\exp(-2\tau_c\eta)\right]/(2S_c\eta) \tag{6.2}$$

Where, z_b and z_t are cloud base and top, respectively; η is the multiple scattering factor. Finally, lidar constant C can re-written as:

$$C=\int_{z_b}^{z_t}\left[P(z)z^2\right]dz*(2S_c\eta)/\left[1-\exp(-2\tau_c\eta)\right] \tag{6.3}$$

If the cloud optical depth is large enough, then the denominator $\left[1-\exp(-2\tau_c\eta)\right]$ is close to 1.0. Thus, the lidar constant C can be estimated from Eq. (6.3) with a constant lidar ratio and a multiple scattering factor (η≈0.9 here). This method has been applied to ceilometers [10]. The uncertainties will be discussed later.

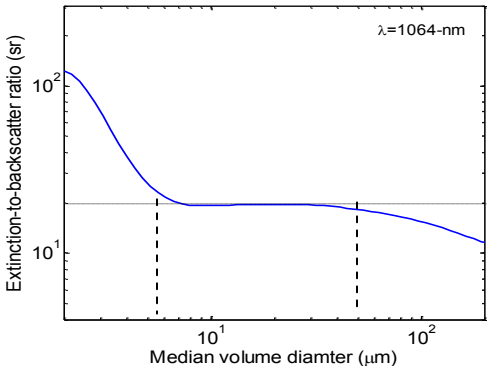

Figure 6.1: Water cloud extinction-to-backscatter ratio verses droplet median diameter.

6.2.2 Calibration with high cirrus clouds

From Eq.(6.1), the lidar system constant can be written as:

$$C=P(z)\times z^2 / T^2_m(z) / T^2_a(z) /\beta_m(z) / R(z) \tag{6.4}$$

where R(z) is the aerosol scattering raio defined as $R(z)= [\beta_a(z)+ \beta_m(z)]/ \beta_m(z)$. The first step is to use the sun photometer measured AOD to calibrate the lidar constant for the *532nm* channel. If we assume $R(z_{ref})=1.01$ at *532nm* in the upper troposphere and estimate the aerosol transmittance $T^2_p(Z_{ref})=\exp(-2*\tau)$ with the sun photometer measured aerosol optical depth (AOD or τ), then the lidar constant C_{532} can be calculated from Eq. (6.4). In order to verify C_{532}, conversely, we apply C_{532} to other lidar data time series and get the lidar derived τ, and then compare them to the sun photometer measured τ. This approach was applied in the micro-pulse lidar observation [16]. The calibration constant at 532 nm in this approach is not supposed to be very sensitive to R_c. Linear error propagation from $R(z_{ref})$ to C_{532} can be seen from Eq.(6.4) However, it is not an easy task to directly apply the first step to the *1064nm* channel because of its SNR at Z_{ref} is usually much lower and $R(z_{ref})$ has a large uncertainty, resulting in a large error in C_{1064}. As shown in the previous chapter for one particular value of the backscatter ratio *1.1*, when $R_{ref}(532)$ varies from 1.01 to 1.1, $R_{ref}(1064)$ will vary from 1.08 to 1.6 (aerosol angstrom exponent=1.0). That means, when $R_{ref}(532)$ varies by ~9 %, then $R_{ref}(1064)$ will vary by ~48%. So, the uncertainty of R_{ref} would affect the calibration accuracy much more severely at 1064 nm than 532 nm channel. The second step is to use the backscatter wavelength independence of cirrus cloud to estimate the lidar system constant at 1064nm. The ratio of lidar signals at *532nm* and *1064nm* in the cirrus cloud can be written as:

$$\frac{P(1064,z_c)}{P(532,z_c)} = \frac{C_{1064}\times\left[\beta_c(1064,z_c)+\beta_m(1064,z_c)\right]\times T^2{}_m(1064,z_0,z_c)\times T^2{}_a(1064,z_0,z_b)\times T^2{}_c(1064,z_b,z_c)}{C_{532}\times\left[\beta_c(532,z_c)+\beta_m(532,z_c)\right]\times T^2{}_m(532,z_0,z_c)\times T^2{}_a(532,z_0,z_b)\times T^2{}_c(532,z_b,z_c)}$$

$$= \frac{C_{1064}\times\left[\beta_c(1064,z_c)+\beta_m(1064,z_c)\right]}{C_{532}\times\left[\beta_c(532,z_c)+\beta_m(532,z_c)\right]}\times K_m(z_0,z_c)\times K_a(z_0,z_b)\times K_c(z_b,z_c) \qquad (6.5)$$

K_m, K_a and K_c are the two-wavelength transmittance ratios of molecule, aerosol and cloud, respectively. In the cirrus cloud at altitude z_c, if we assume $\beta_c(1064,z_c) \cong \beta_c(532,z_c)$, $\beta_c(1064,z_c) >> \beta_m(1064,z_c)$, $\beta_c(532,z_c) >> \beta_m(532,z_c)$, and $K_c(z_b, z_c) \cong 1$; then C_{1064} becomes:

$$C_{1064} = \frac{P(1064,z_c)}{P(532,z_c)} \times C_{532} / K_m(z_0,z_c) / K_a(z_0,z_b) \qquad (6.6)$$

Molecular transmittance ratio K_m can be calculated from the radiosonde measured temperature and pressure profiles, and the aerosol transmittance ratio K_a will be estimated from the sun photometer measured AOD in the adjacent clear sky patch. A quite similar approach is applied to the space borne lidar, CALIPSO, in which C_{532} is calibrated by matching lidar return signals with the pure molecular values over 30~35 km altitudes in the stratosphere at night time, and then the *1064nm* channel is calibrated relative to the *532nm* total backscatter signal using cirrus clouds as targets [14, 15].

6.3 Applying the methods

6.3.1 Low cloud method

Illustration of two cases of calibration with low cloud. First case:

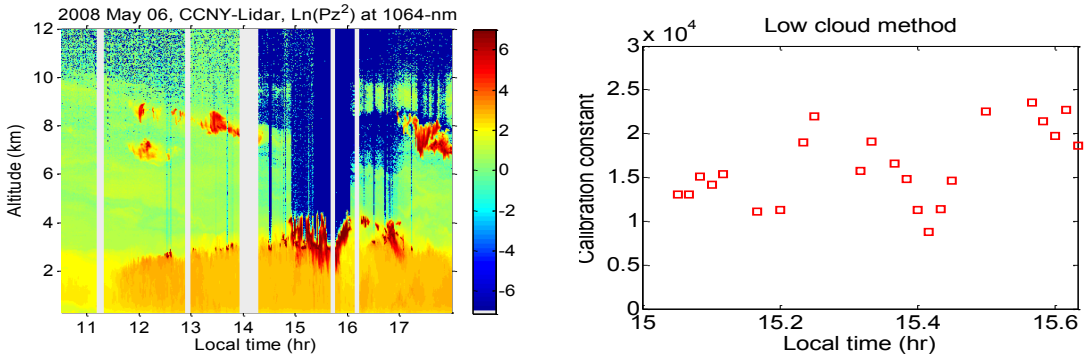

Figure 6.2: (a) Range-corrected lidar returns on May 6 2008, (b) Calibration constant using the low water cloud.

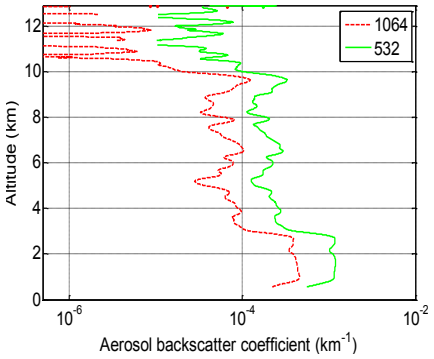

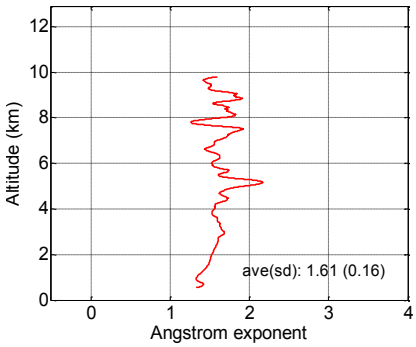

Figure 6.3: (a) Estimate of aerosol backscatter with lidar constant and (b) Angstrom exponent.

Second case:

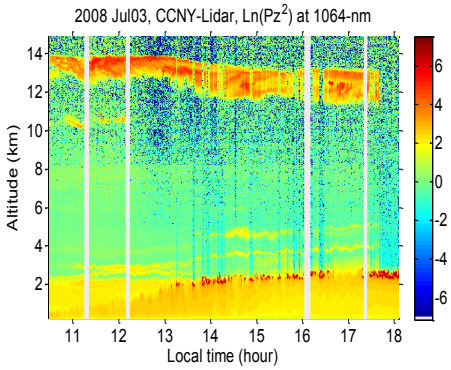

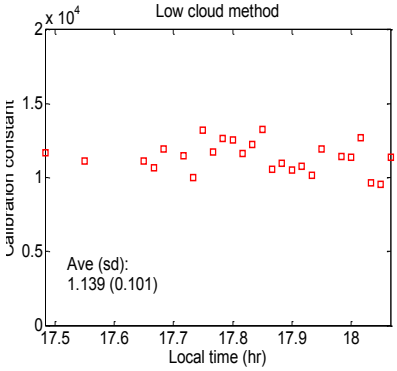

Figure 6.4: (a) Range scaled lidar returns on July3 2008, (b) low water cloud

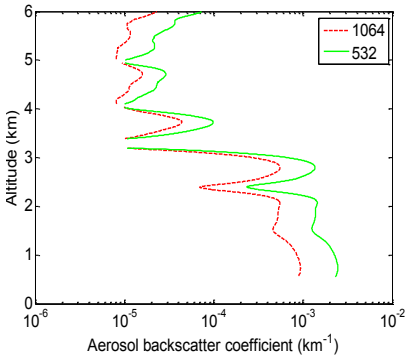

Figure 6.4: (c) Aerosol backscatter

Correctness of the calibration constant was tested by applying it directly to estimate the aerosol backscatter at *1064nm* and the Angstrom exponent. Figures 6.3 (a) and (b) illustrate aerosol backscatter and Angstrom exponent profiles, respectively. Quite similar fine structures of aerosol backscatter for the two wavelengths at *1064nm* and *532nm* are shown in Figure 6.3 (a) Angstrom exponents are calculated with two-wavelength backscatter coefficients at *1064nm* and *532nm* and have a column average value of *1.61*, which shows a reasonable agreement with a sun photometer measured column Angstrom exponent of *1.23* Ignoring aerosol transmittance will result in an underestimate of the *1064nm* backscatter and an overestimate of the Angstrom exponent. According to the sun photometer measured aerosol optical depths ($\tau(1020)=0.106$), the maximum error of backscatter is less than *20%*

In the second case, figure 6.4 (a) shows the range scaled lidar signal. The calibration constant was once again obtained by applying O'Conner's algorithm to the low level cloud. Figure 6.4 (b) shows the result. The aerosol backscatter profile obtained by using this result is also plotted in Figure 6.4 (c) along with that for the 532*nm* channel. They show quite a similar profile structure for the two wavelengths. The average Angstrom coefficient from the backscatter at the two wavelength is *1.2* , which is consistent with the sunphotometer measured column value of *1.29*

6.3.2 High cloud method

The method outlined above was used to obtained the calibration constant by applying Eq. (6.6) to the lidar return from the cirrus cloud. Plotted are the results of the

calibration constant C_{1064} varying with time. The period of fluctuation is often different for different time intervals. It may indicate some periodic nature of fluctuations with some physical properties in the cloud.

6.3.2.1 Results of Calibration by cloud

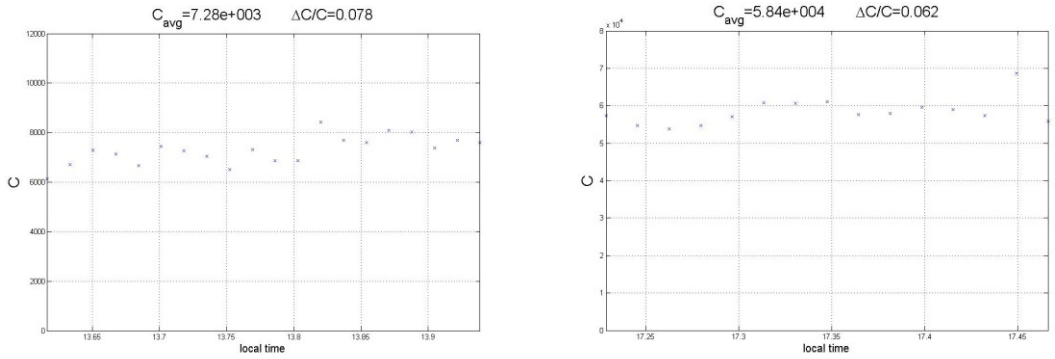

Figure 6.5: Calibration constants determined by high cloud method
(a) Apr10, 2008 (b) Apr16, 2008

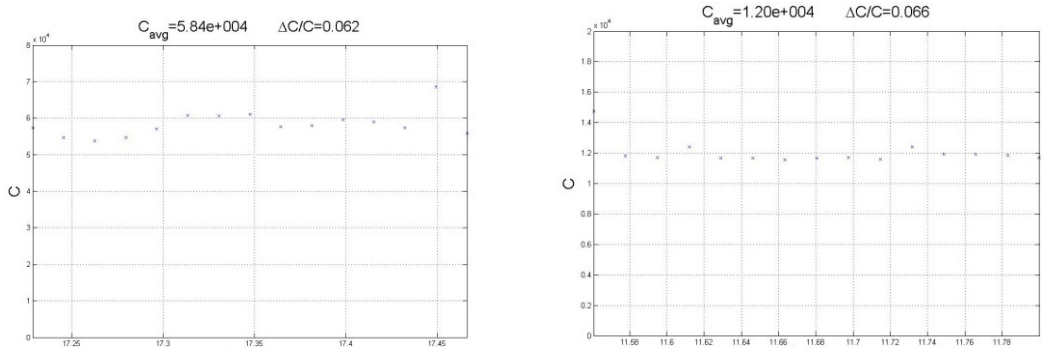

Figure 6.5: Calibration constants determined by high cloud method
(c) Apr18, 2008 (d) Apr 23, 2008

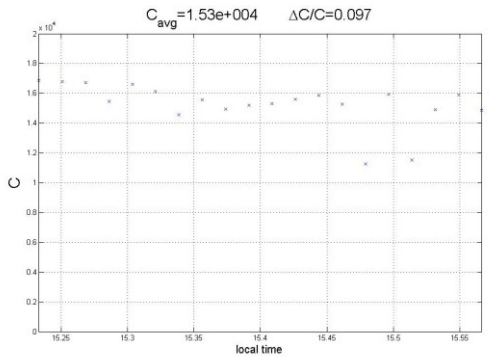

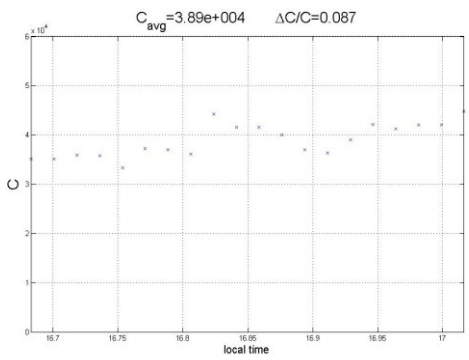

Figure 6.5: Calibration constants determined by high cloud method
(e) May 7, 2008 (f) May 13, 2008

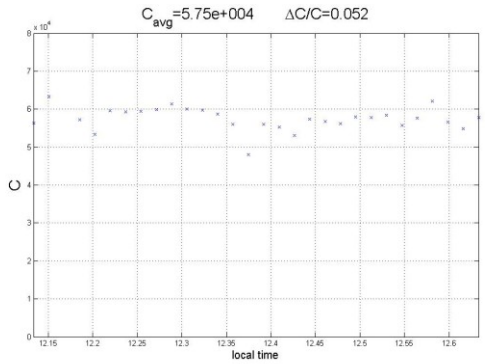

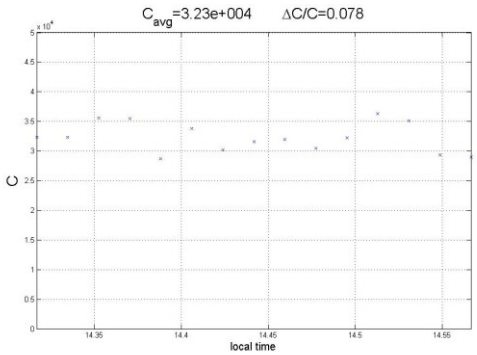

Figure 6.5: Calibration constants determined by high cloud method
(g) May 14, 2008 (h) May 29, 2008

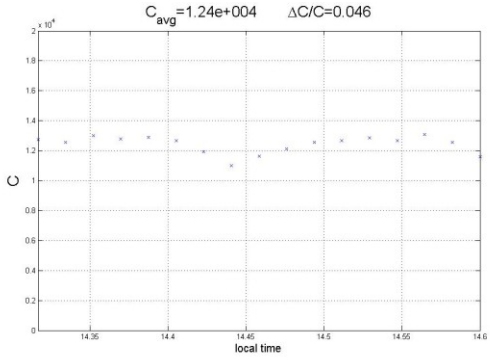

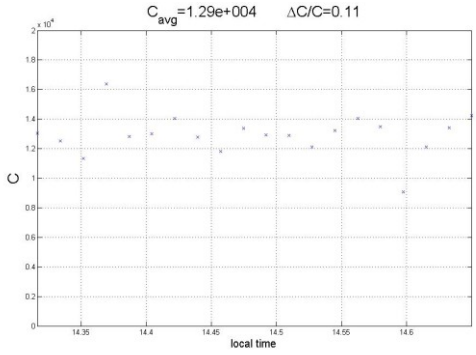

Figure 6.5: Calibration constants determined by high cloud method
(i) May 5, 2008; Upper cirrus (j) May 5, 2008; Lower cirrus

6.3.3 Ceilometer method

A regression of lidar return against ceilometer data between $500m$ and $1000m$ is carried out for each day. The resulting slope gives a value of calibration constant C. Since the ceilometer data is noisy, a running average of $10\,\text{min}$ was used. Data was chosen below $1000m$ for better SNR and above $500m$ to be in the complete overlap range of the lidar instrument.

6.3.3.1 Results of Calibration by ceilometer

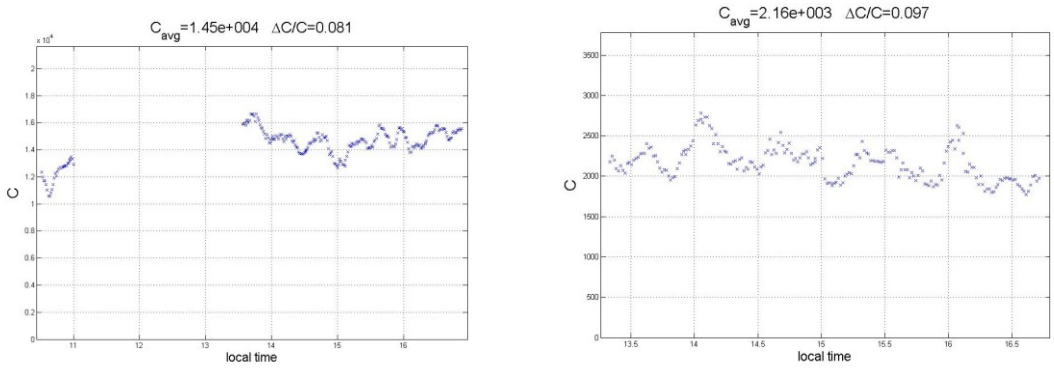

Figure 6.6: Calibration constants determined by ceilometer method
(a) Apr 2, 2008 (b) Apr 14, 2008

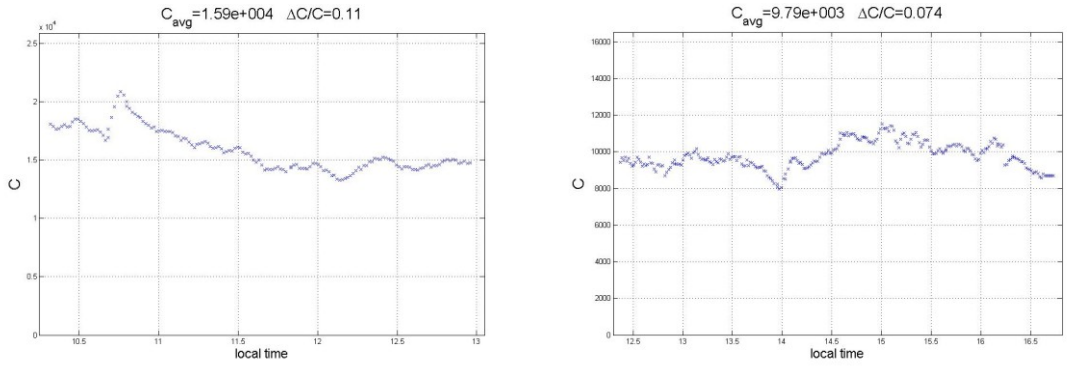

Figure 6.6: Calibration constants determined by ceilometer method
(c) Apr 23, 2008 (d) Apr 24, 2008

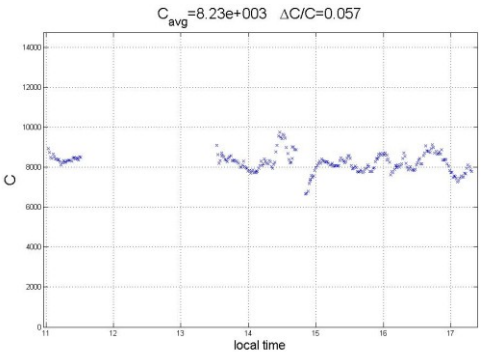

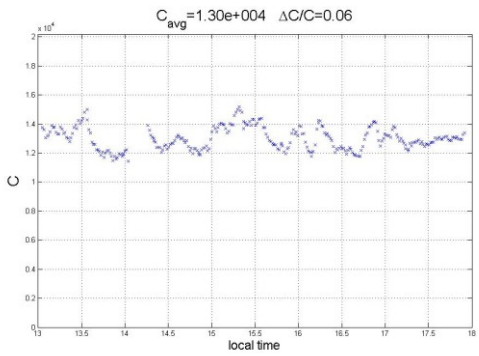

Figure 6.6: Calibration constants determined by ceilometer method
(e) Apr 30, 2008 (f) May 6, 2008

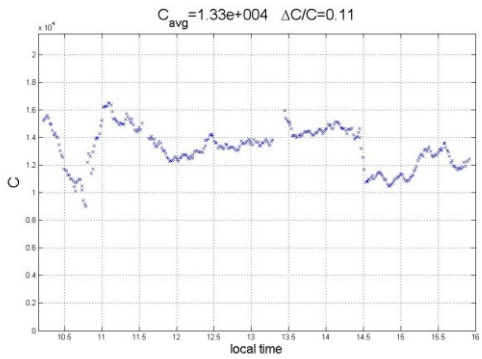

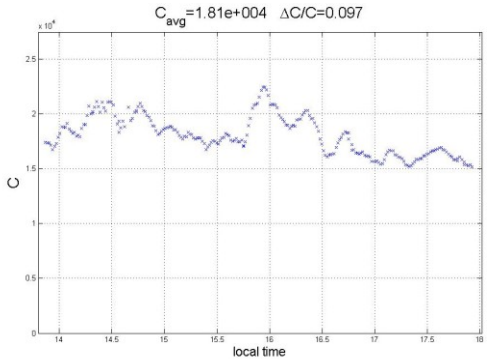

Figure 6.6: Calibration constants determined by ceilometer method
(g) May 7, 2008 (h) May 29, 2008

6.4 Comparison with sun photometer AOD

The calibration constants obtained by the cloud and ceilometer methods are applied to the lidar data to evaluate the aerosol optical depths. A lidar ratio of $40\,sr$ was used for aerosol. A lidar ratio range of 35 to 68 sr was calculated at *1053nm* [28] and of $40\,sr$ for the volcanic stratospheric aerosols. Even though volcanic stratospheric aerosols

are not expected above our location, a value slightly less than $50\,sr$ for the $532nm$ channel is expected. It fits the AODs well in practically all cases when the calibration constant is determined correctly. For the cirrus cloud, a still slightly less value of $30\,sr$ is used [29]. When the calculated AODs diverge, it is either due to too high a value for the cloud was used, or numerical instability when applying the forward integration in the inversion method. For cirrus cloud, it has been found to vary over a range of less than 10 to larger than 100 sr [28]. Liu also demonstrated that an incorrect lidar ratio can cause large retrieval errors especially for thick aerosol and cloud. Lidar ratios vary over different types of particulates as well as the lidar range. Even though a lot of studies are being conducted to compute them, there are still much uncertainty associated with them.

6.4.1 Results verified by measured optical depth

The solid lines indicate AODs evaluated by the calibration constants obtained by the ceilometer method and the dotted lines indicate those obtained by the cloud method. Sun photometer measured AOD values are represented by red circles.

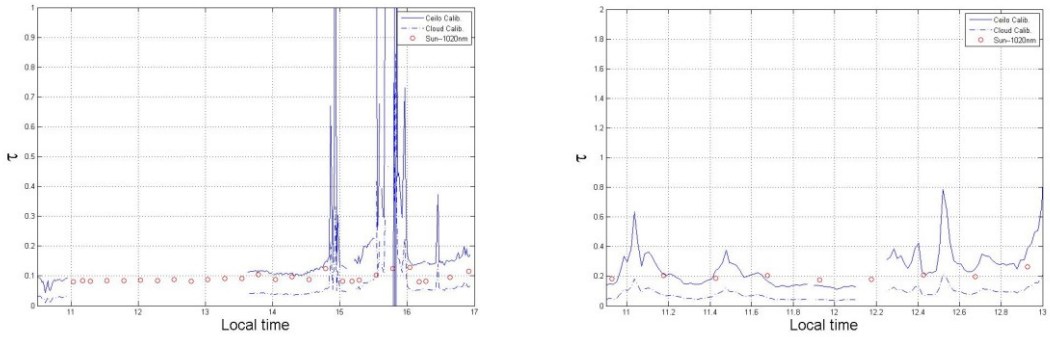

Figure 6.6: Optical depths evaluated by two methods of calibration
(a) Apr 2, 2008 (b) Apr 10, 2008

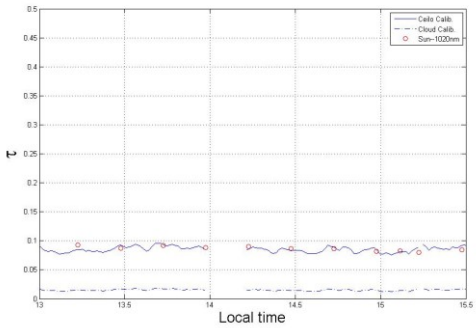

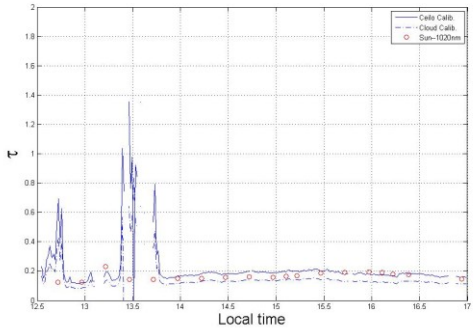

Figure 6.7: Optical depths evaluated by two methods of calibration
(c) Apr 16, 2008 (d) Apr 18, 2008

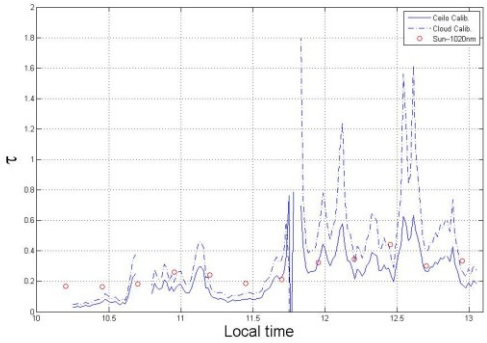

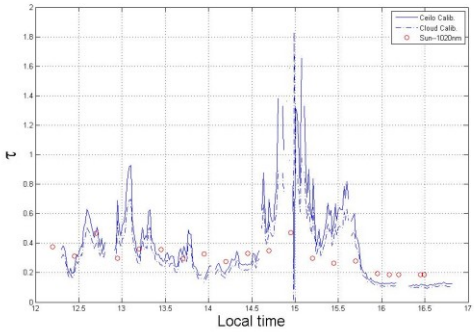

Figure 6.7: Optical depths evaluated by two methods of calibration
(e) Apr 23, 2008 (f) Apr 24, 2008

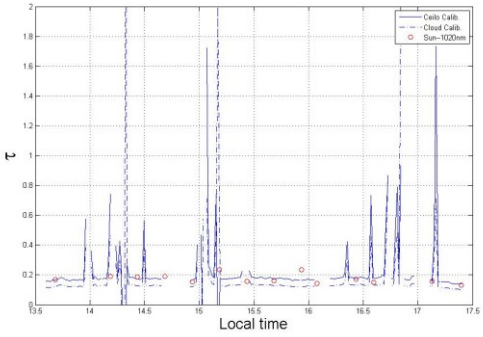

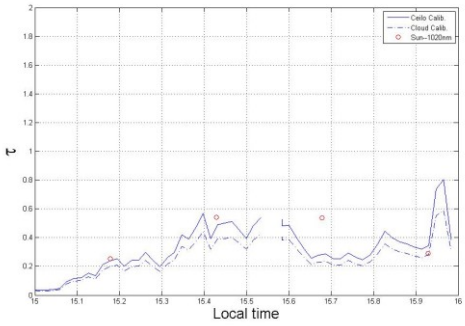

Figure 6.7: Optical depths evaluated by two methods of calibration
(g) Apr 30, 2008 (h) May 7, 2008

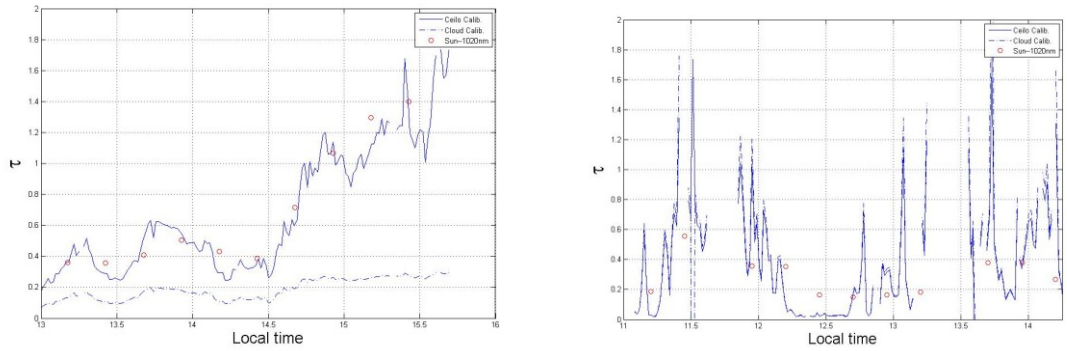

Figure 6.7: Optical depths evaluated by two methods of calibration
(i) May 14, 2008 (j) May 30, 2008

6.5 Tabulated results

Results are entered into the following table and not all of them have been graphically displayed in the above section.

	C_{1064}	$\Delta C_{1064} / C_{1064}$	C_{532}	C_{1064}	$\Delta C_{1064} / C_{1064}$
Methods	Cloud			Ceilometer	
Dates	$\times 10^4$	%	$\times 10^3$	$\times 10^4$	%
4/2/2008	2.8621	10.09	4.8	1.445	8.13
4/3/2008	3.8744	8.44	4.8	2.7084	20.88
4/10/2008	0.7285	7.79	2.1	0.38069	41.12
4/14/2008 Low cloud	2.1521	10.4	N/A	0.21648	9.72
4/16/2008	5.8406	6.23	1.65	1.9262	48.95
4/18/2008	4.3125	6.53	1.9	3.3848	41.14
4/23/2008	1.2025	6.65	2.3	1.587	11.12
4/24/2008	1.093	2.66	2.03	0.97868	7.43
4/30/2008 Low cloud	1.0388	5.1	N/A	0.823	5.7
5/5/2008	1.243	4.63	1.9	1.1776	13.58
5/6/2008	1.5441	21.02	2.1	1.3003	6.02
5/7/2008	1.526	9.74	1.7	1.327	11.13
5/13/2008	3.887	8.7	8	1.6866	29.68
5/14/2008	5.7462	5.2	12.5	2.6955	28.07
5/29/2008	3.2292	7.8	11.5	1.8064	9.67
5/30/2008	2.5016	12.77	8	2.6012	21.43

Table 6.1 Calibration constants

6.6 Discussion

The low cloud method has a major drawback of having to correct for the its finite optical depth. Since the method relies on its thickness for extinction, no sun photometer can make this correction. The Raman signal is also attenuated one way by aerosol and has a small cross section at the Raman wavelength and its return often requires a good deal of averaging. After all, its channel wavelength is not the same as the Mie $1064nm$ channel that needs to be calibrated so that the optical thickness correction by the Raman channel is not realistic. It is therefore not surprising that the calibration constant determined by the low cloud has a large deviation from the mean. Mutiple scattering is another correction factor that needs to be considered for thick clouds. It depends on droplet radii and the receiver field of view. Multiple scattering errors of measured extinction coefficients are typically of the order of 50% at the bases of both water and ice clouds and decrease with increasing penetration depth to below 20% [21]. Saturation of the detector by strong return from the low cloud is another factor that needs to be monitored during data acquisition. As a solution a neutral density filter can be set in front of the detector. Besides saturation, an uncertainty stems from the cloud phase whether it is water, mixed or ice phase which will affect the value of the lidar ratio. The temperature profile measured by radiosonde or predicted by models can help determine it. Another more involved solution is a depolarized channel to help distinguish the phase.

The calibration constants evaluated by the high cloud method are larger than those evaluated by the ceilometer method except for two dates, May30 2008 and Apri23 2008 where the are smaller by more or less 10%. The constants evaluated by the high cloud

method are not only larger, they are also too large to give a good match of the AODs measured by the sun photometer as a glance of the optical depth plots will confirm this; the dotted lines are AODs by the cloud method. There are four possible sources of calculation error in the calibration equation, repeated here for convenience.

$$\frac{P(1064,z_c)}{P(532,z_c)}=\frac{C_{1064}\times\left[\beta_c(1064,z_c)+\beta_m(1064,z_c)\right]\times T^2{}_m(1064,z_0,z_c)\times T^2{}_a(1064,z_0,z_b)\times T^2{}_c(1064,z_b,z_c)}{C_{532}\times\left[\beta_c(532,z_c)+\beta_m(532,z_c)\right]\times T^2{}_m(532,z_0,z_c)\times T^2{}_a(532,z_0,z_b)\times T^2{}_c(532,z_b,z_c)}$$

$$=\frac{C_{1064}\times\left[\beta_c(1064,z_c)+\beta_m(1064,z_c)\right]}{C_{532}\times\left[\beta_c(532,z_c)+\beta_m(532,z_c)\right]}\times K_m(z_0,z_c)\times K_a(z_0,z_b)\times K_c(z_b,z_c) \qquad (6.5)$$

The four possible errors are the calibration constant for the $532nm$ channel C_{532}, the signal ratio obtained from the cloud $X/Y=P(1064,z_c)/P(532,z_c)$,the color ratio $\chi=\beta_{1064}/\beta_{532}$ in cloud and the transmission ratio from the reference range z_c through the cloud $T^2(1064,z_b,z_c)/T^2(532,z_b,z_c)$.

6.6.1 Possible errors

I. C_{532} is determined by matching the sun photometer AOD. The typical optical thickness for a clear patch on a day with high cirrus is no larger than 0.2. Indeed, this example is taken from one of the calibration dates. The calibration constant C_{532} that gives an optical thickness of 0.2 for that day is 4.8×10^3. For a 100% mismatch or misidentification of the optical thickness of 0.1 to happen, C_{532} only changes by about 8% to 5.2×10^3. The plot shows this behavior.

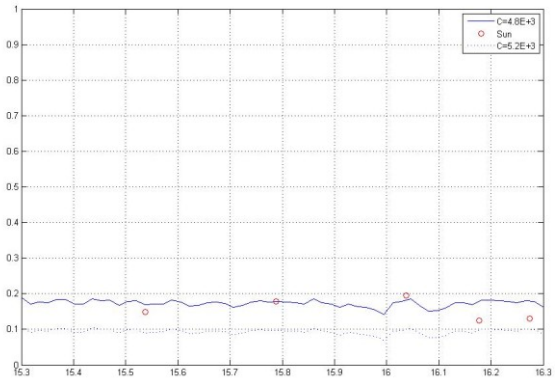

Figure 6.8 Variation of C_{532} with AOD

Often the calibration constant determined by the cloud method is much larger than within 10% error of the value required to match the sun photometer AOD. Sometimes they are twice too large. So it does not seem C_{532} is the biggest source of error.

II. The signal ratio $X/Y = P(1064, z_c)/P(532, z_c)$ as determined by the lidar returns from the cloud range is often consistent, unambiguous, and independent of locations in the cloud, as long as the signal return is within the cloud ranges, which has a large SNR due to large backscattering. To illustrate this, the signal ratio is evaluated at two separate locations, one situated in an upper level cloud, the other in a lower level during the same data acquisition interval. Their values are 8.8 and 8.6 respectively.

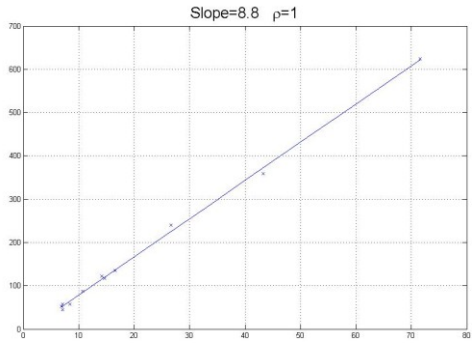

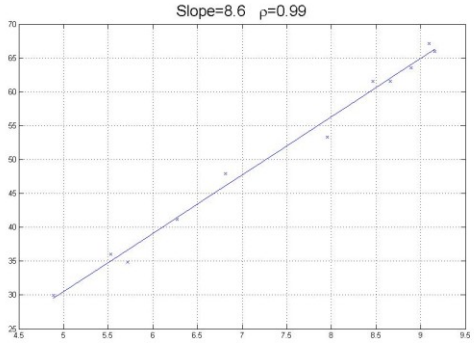

Figure 6.9: Signal ratios
(a) in upper level cirrus
X/Y=5.8

Date: May 5 2008
(b) in lower level cirrus
X/Y=5.6

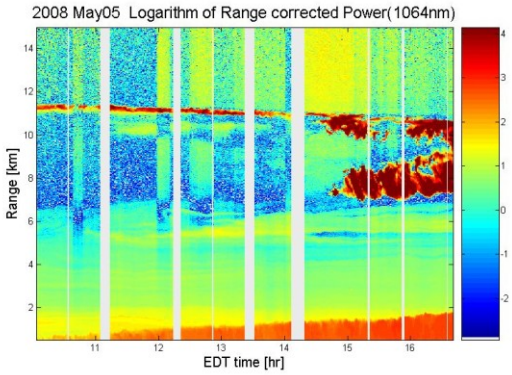

Figure 6.9: (c) upper and lower level cirrus

III. The color ratio $\chi = \beta_{1064} / \beta_{532}$

Mie theory of scattering asserts no wavelength dependence for large particles but it does not suggest a constant backscatter ratio value of unity for all large particles regardless of wavelength. A study reports a even wider spread of the cirrus color ratios with the wavelength pair $355nm$ and $532nm$ [24]. Statistic analysis has indicated that averaged color ratio of cirrus cloud was 0.88±0.12 [26].

For a thin cirrus cloud, the ratio can be inferred from the Young's method

[Young 1995] through association with the transmission. However, for an optically thick cloud, the signal return from above is too weak to apply this method so that an alternative approach introduced by Tao is used [26].

First, define the attenuated backscatter, the subscripts 1 and 2 represent particulates and molecular respectively, and z_c is the reference range at which the total backscatter is assumed to be $1.01\beta_2(z_c)$ at $532nm$ and $1.06\beta_2(z_c)$ at $1064nm$ corresponding to an aerosol backscatter color ratio of 0.375 [23]

i.e. $\chi = (R_{1064} - 1)/\left[16(R_{532} - 1)\right]$

$$\beta'(z) = \left[\beta_1 + \beta_2\right] \exp\left(-2\int_{z_c}^{z} \alpha_1(z') + \alpha_2(z')\, dz' \right) = X(z)/C' \tag{6.7}$$

where $X(z)$ is the range scaled lidar signal,

$$C' = C \exp\left(-2\int_{0}^{z_c} \alpha_1(z') + \alpha_2(z')\, dz' \right) = \frac{X(z_c)}{R(z_c)\beta_2(z_c)} \tag{6.8}$$

$$\chi(z) \approx \frac{\beta'_{1064}(z) - \beta_{2,1064}(z)}{\beta'_{532}(z)/T_{2,532}(z) - \beta_{2,532}(z)} \tag{6.9}$$

where the molecular transmission from z_c to z for $1064nm$ is close to 1 and is ignored.

In view of the color ratio being not identically equal to 1, the transmission ratio at the two wavelengths in cloud would not be identically equal

to 1 as it should have a dependence on the color ratio. The color ratio and its histogram evaluated for a cloud in the above data set is shown.

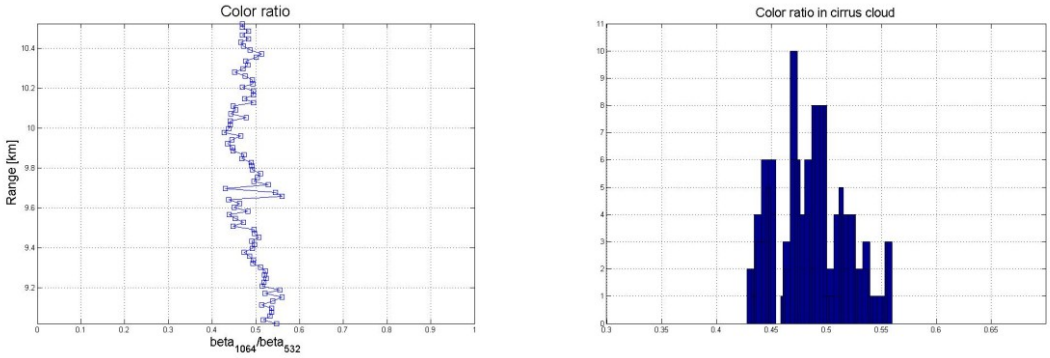

$\chi = \beta_{1064} / \beta_{532}$ $\chi = \beta_{1064} / \beta_{532}$

Figure 6.10: Color ratio (a) plot (b) histogram

It is seen that the color ratio for the day evaluated has a mean value of about 0.5 This explains the large discrepancies between the calibration constant determined by the cloud method and that determined by the ceilometer method, for instance, 2.8621×10^{4} versus 1.445×10^{4} for Apr2, 2008. These results can only indicate that the color ratio is not necessarily unity as it has been often conveniently assumed. Its evaluation depends on accurate estimates of the normalization constants in both channels, and can be computed reliably only when there are no saturated data points in either channel [31]. However, for our purpose, consideration of the color ratio is really for determining the calibration constant at 1064 nm, not the other way round. It constitutes a vicious circle to engage in an accurate determination of the color ratio by using the normalization constants.

Summary

Two methods of calibration have been used and verified against the AOD values measured by the sun photometer. They are the cloud method and the ceilometer method. The low cloud method is not a very practical one due to the difficulty in obtaining its optical thickness for the correction factor. Mutiple scattering effect is also another factor difficult to estimate precisely. Nevertheless, with these difficulties the result leads to the correct averaged Angstrom coefficients.

The high cloud method shows a consistent signal return ratio from cloud $X/Y = P(1064, z_c)/P(532, z_c)$ in the same time interval and gives the least error of usually under 10%. However, the other sources of error such as the transferred calibration constant in the $532nm$ channel and above all the deviation of the color ratio from unity can result in huge errors in the calibration constant C_{1064}

The ceilometer operates on low SNR due to its low power design. The data fluctuate about the mean with large spreads of often tens of percents. However, in general its mean gives the correct calibration constant as verified by the sun photometer AODs. It does not depend on other corrections or parameters that are prone to various sources of error.

REFERENCES

[1] J. D. Klett, "Stable analytical inversion solution for processing lidar returns.", *Appl. Opt.,* 20(2), 211-220,1981

[2] F. G. Fernald, "Analysis of atmospheric lidar observations: some comments.", *Appl. Opt.*, 23, 652-653, 1984

[3] P. B. Russell, Thomas J. Swissler, M. Patrick McCormick, "Methodology for error analysis and simulation of lidar aerosol measurements.", *Appl. Opt.*, 18, 3783-3797,1979

[4] J. Zhang and Huanling Hu, "Lidar calibration, a new method.", *Appl. Opt.*, 36, 1235-1238,1997

[5] M. Pahlow, V.A. Kovalev, M.Parlange, "Calibration method for mutiangle lidar measurements.", *Appl. Opt.*, Vol.43, No.14, 2948-2956, 2004

[6] J. Porter, B. Lienert, S. K. Sharma, "Using Horizontal and Slant Lidar Measurements to Obtain Aerosol Scattering Coefficients from a Coastal Lidar in Hawaii.",*Journal of atmospheric and Oceanic Technology*,17,1445-1454, 2000

[7] M. J. Kavaya,, R. T. Menzies, D. A. Haner, U. P. Oppenheim, P. H. Flamant, "Target reflectance measurements for calibration of lidar atmospheric backscatter data.", *Appl. Opt.*, 22, 2619-2628, 1983

[8] M. Jarzembski, V. Srivastava, and D. Chambers, "Lidar calibration technique using laboratory-generated aerosols.", *Appl. Opt.,* 35, 2096-2108,1996

[9] J. D. Spinhirne, S. Chudamani, J. F. Cavanaugh, J. L. Bufton, "Aerosol and cloud backscatter at 1.06, 1.54 and 0.53 microns by airborne hard-target calibrated Nd:YAG methane raman lidar.", *Appl. Opt.*,36, 3475–3490, 1997

[10] E. J. O'Connor, A.J. Illingworth and R.J. Hogan, "A technique for autocalibration of cloud lidar.", *J. Atmos. Ocean.Tech.* 21(5), 777-778, 2004

[11] J. Zhang et al., "A lidar calibration method by water cloud.", *Proceedings of ILRC*, Quebec City, 625-628, 2002

[12] Y. Hu, "Using Water Clouds for Lidar Calibration, in Laser Applilcations to Chemical, Security and Environmental Analysis.", *Technical Digest (Optical Society of America*), paper TuA4, 2006

[13] R. G. Pinnick, S. G. Jennings, P. Chýlek, C. Ham, W. T. Grandy Jr., "Backscatter and extinction in water cloud.", *J. Geophys. Res.,* 88 (11), 6787-6796,1983

[14] M. J. Reagan, X. Wang, M. J. Osborn, "Spaceborne lidar calibration from cirrus a nd molecular backscatter returns.", *IEEE Trans. Geosci. Remote Sens.*, 40, 2285–2290, 2002

[15] Chris A. Hostetler, Zhaoyan Liu, John Reagan, Mark Vaughan, David Winker, et al., "CALIOP Algorithm, Theoretical Basis Document Calibration and Level 1 Data Products, PC-SCI-201, Release 1.0 , Apr. (2006).", 2006

[16] E. J. Welton, K. J. Voss, P. K. Quinn, P. J. Flatau, K. Markowicz, J. R. Campbell, J. D. Spinhirne, H. R. Gordon, and J. E. Johnson, "Measurements of aerosol vertical profiles and optical properties during INDOEX 1999 using micropulse lidars.", *J. Geophys. Res.*, 107(D19), 8019, 2002

[17] R. M. Hoff, et al., "Regional East Atmospheric Lidar Mesonet:REALM, in Lidar Remote Sensing in Atmospheric and Earth Sciences.",edited by L. Bissonette, G. Roy, and G. Valle´e, pp. 281– 284, *Def. R&D Can. Valcartier*, Val-Be´lair, Quebec , 2002

[18] B. N. Holben, T. F. Eck, I. Slutsker, et al., "AERONET-A federated instrument network and data archive for aerosol characterization.", *Remote Sens. Environ.*, 66, 1~16, 1998

[19] C. Münkel, J. Räsänen, "New optical concept for commercial lidar ceilometers scanning the boundary layer.", *Proc. SPIE 5571*, pp. 364-374, 2004

[20] E. W. Eloranta, "A practical model for the calculation of multiply scattered lidar returns.", *Appl. Opt.* 37, 2464-2472, 1998

[21] U. Wandinger, "Multiple-scattering influence on extinction and backscatter coefficient measurements with Raman and High-Spectral-Resolution Lidars.", *Appl. Opt.,* 37, 417-427, 1998

[22] R. J. Hogan, "Fast approximate calculation of multiply scattered lidar returns.", *Appl. Opt.*, 45, 5984-5992, 2006

[23] Z. Tao, M. P. McCormick, D. Wu, Z. Liu, Mark A. Vaughan, "Measurements of cirrus cloud backscatter color ratio with a two-wavelength lidar.", *Appl. Opt.*, 47, 1478-1485. 2008

[24] M. A. Vaughan, Science Systems & Applications Inc. (SSAI), NASA Langley Research Center, Hampton, Va. 23681, "USA is preparing a manuscript to be called “Backscatter color ratios of cirrus clouds measured by the cloud physics lidar.”, 2008

[25] S. A. Young, “Analysis of lidar backscatter profiles in optical thin clouds,” *Appl. Opt.*34, 7019-7030, 1995

[26] Zongming Tao, M. Patrick McCormick, Dong Wu, Zhaoyan Liu, and Mark A. Vaughan, "Measurements of cirrus cloud backscatter color ratio with a two-wavelength lidar.", *Applied Optics*, Vol. 47, No. 10, 1478-1485, 2008

[27] P. B. Russell, T. J. Swissler, and M. P. McCormick, “Methodology for error analysis and simulation of lidar aerosol measurements,”*Appl. Opt*. 18, 3783–3797, 1979

[28] Zhaoyan Liu, Peter Voelger, and Nobuo Sugimoto, "Simulations of the observation of clouds and aerosolswith the Experimental Lidar in Space Equipment system.", *Applied Optics*, Vol. 39, No. 18, 3120-3137, 2000

[29] Wei-Nai Chen, Chih-Wei Chiang, and Jan-Bai Nee, "Lidar ratio and depolarization ratio for cirrus clouds.", *Applied Optics*, Vol. 41, No. 30, 6470-6476, 2002

[30] Ulla Wandinger, "Multiple-scattering influence on extinctionand backscatter-coefficient measurements with Raman and high-spectral-resolution lidars.",Vol. 37, No. 3, *Applied Optics*, 417-427, 1998

[31] Mark Vaughan, "PICASSO-CENA: Pathfinder Instruments For Cloud And Aerosol Spaceborne Observations. Algorithm Theoretical Basis Document (ATBD) White Papers.", *Science Applications International Corporation,*1999

Conclusion

Clouds offer a natural target for calibration of the lidar instrument. Its occurrence is frequent enough to warranty its practicality. A low cloud target for the purpose of calibration is optically thick and suffers the drawback of not being able to have its optical depth reliably determined and requires the correction factor of the multiple scattering effects which is not readily estimated accurately. The calibration constant so determined has a large uncertainty due to these two uncertainty correction factors.

The results determined by high cloud backscatter are more consistent regardless of the optical thickness of the target cirrus and the uncertainty is small, mostly several percents only. However, the mean is not necessarily accurate because of other multiplicative factors which are eventually determined by the aerosol optical thickness at the two wavelengths and the color ratio of the ice crystals in cirrus. The transference of the calibration constant at $532nm$ to the $1064nm$ channel is particularly not suitable for the ground based lidar due to the intervening aerosol column between it and the cirrus cloud. Theoretical calculations of scattering by ice crystals of all sizes and shapes are difficult. Reliance on a data base for computed color ratios requires identification of the cirrus type.

While all that collaboration of theory and practice may be necessary especially for the space borne lidar that relies on cirrus clouds for calibration on a routine basis, the calibration of our ground lidar at $1064nm$ has been achieved by the ceilometer co-located at the same site. The results are verified by the AODs measured by the sun photometer which has been reliably calibrated itself. Even though this method does give a correct

mean value of the calibration constant, the spread about the mean is often much larger than that obtained by the cirrus cloud method. Attempts to account for the variations in the lidar system which affect the calibration constant, such as those caused by misalignment or simply routine realignments, by evaluating the mean values over shorter periods of time result in values that do not verify with the measured AODs. In data processing, heavy averaging is often required for noisy data. The problem seems to lie exclusively in the low power design of the ceilometer that results in a low signal to noise ratio. Besides, this method relies on the calibration of a second instrument, the ceilometer. With these shortcomings of calibration by the ceilometer and the practical difficulties encountered in the calibration of a ground based lidar by clouds, calibration by the ceilometer is still the only reliable method to calibrate the ground based 1064*nm* channel.

A.1 Overlap function

A.1.1 How image is formed

An object with a field distribution $f(x,y)$ placed a distance d_1 from the telescope (or equivalently a lens) forms an image in the image plane.

The field distribution could represent the transmission function of the object such as a transparency filter. If a plane wave illuminates this object, then the field distribution immediately behind the object is $f(x,y)$. As the wave distribution progresses in space, it undergoes Fresnel diffraction,

$$\frac{1}{\lambda d_1} f(x,y) * \exp\left[-i\alpha(x^2+y^2)\right] \qquad * \text{ denotes convolution} \qquad \text{(A1.1)}$$

where $\alpha = \frac{k}{2d_1} = \frac{\pi}{\lambda d_1}$

The field distribution can be regarded as the input in the system to the free-space which has the impulse response of the exponential function. The entire mathematical operation is the well established Fresnel Transform.

The receiving mirror (lens) imparts a location dependent phase change of the field, obviously from a diverging to a converging wave after the mirror (lens) i.e.

from $$\exp\left(-ik\sqrt{x^2+y^2+d_1^{\,2}}\right) \approx e\exp\left[-ik\left(d_1 + \frac{x^2+y^2}{2d_1}\right)\right] \qquad \text{(A1.2)}$$

to $$\exp\left[ik\left(d_2+\frac{x^2+y^2}{2d_2}\right)\right]$$

Therefore, the effective multiplying factor of the mirror (lens) must be,

$$p_L=\exp\left[ik(d_1+d_2)\right]\exp\left\{\frac{ik}{2}\left(\frac{1}{d_1}+\frac{1}{d_2}\right)(x^2+y^2)\right\} \tag{A1.3}$$

Ignoring the first constant factor because it is independent of x and y and applying the thin lens equation

$$\frac{1}{d_1}+\frac{1}{d_2}=\frac{1}{f} \tag{A1.4}$$

$$p_L=\exp\left(ik\frac{x^2+y^2}{2f}\right) \tag{A1.5}$$

Therefore the field distribution immediately after the mirror (lens) is

$$\frac{1}{\lambda d_1}f(x,y)*\exp\left[-i\alpha(x^2+y^2)\right]\exp\left[i\beta(x^2+y^2)\right] \tag{A1.6}$$

where $\beta=\frac{k}{2f}=\frac{\pi}{\lambda f}$

Finally the field distribution at the image $g(x,y)$ is given by carrying out the remaining Fresnel Transform on the last expression as the wave immediately after leaving the mirror (lens) propagates through space towards its image plane a d_2 distance away.

$$g(x,y)=\frac{1}{\lambda d_1}f(x,y)*\exp\left[-i\alpha(x^2+y^2)\right]\exp\left[i\beta(x^2+y^2)\right]*\exp\left[-i\gamma(x^2+y^2)\right] \tag{A1.7}$$

where $\gamma = \frac{k}{2d_2} = \frac{\pi}{\lambda d_2}$

Explicitly,

$$g(x,y) = \frac{1}{\lambda^2 d_1 d_2} \iiint_{-\infty}^{\infty} f(\xi,\eta) \exp\left\{-i\alpha\left[(\xi' - \xi)^2 + (\eta' - \eta)^2\right]\right\} \times \exp\left[i\beta(\xi'^2 + \eta'^2)\right] \times \exp\left\{-i\gamma\left[(x - \xi')^2 + (y - \eta'^2)\right]\right\} d\xi d\eta d\xi' d\eta' \tag{A1.8}$$

Multiplying out the exponents and using the imaging relationship $\beta = \alpha + \gamma$,

$$g(x,y) = \frac{1}{\lambda^2 d_1 d_2} \exp\left[-i\gamma(x^2 + y^2)\right] \iint_{-\infty}^{\infty} d\xi d\eta f(\xi,\eta) \exp\left[-i\alpha(\xi^2 + \eta^2)\right] \times \iint_{-\infty}^{\infty} d\xi' d\eta' \exp\left\{2\pi i\left[\xi'\left(\frac{\xi}{\lambda d_1} + \frac{x}{\lambda d_2}\right) + \eta'\left(\frac{\eta}{\lambda d_1} + \frac{y}{\lambda d_2}\right)\right]\right\} \tag{A1.9}$$

The second double integral is the Dirac delta function [1],

$$\lambda^2 d_1^2 \delta\left(\xi + \frac{x}{M}\right)\delta\left(\eta + \frac{y}{M}\right) \tag{A1.10}$$

where $M = \frac{d_2}{d_1}$ is the magnification of the imaging system.

$$\Rightarrow\ g(x,y) = \frac{1}{M} f\left(-\frac{x}{M}, -\frac{y}{M}\right) \exp\left[-i\frac{\pi d_1}{\lambda d_2 f}(x^2 + y^2)\right] \tag{A1.11}$$

so that the intensity distribution is,

$$|g(x,y)| = \frac{1}{M^2}\left|f\left(-\frac{x}{M}, -\frac{y}{M}\right)\right|^2 \tag{A1.12}$$

It can be seen that the intensity distribution at the image is the same as that of the object except for its inverted position with the negative sign, and its size is modified by a magnification factor M.

This interpretation of the transform integrals rests on the assumption that the pupil function is unity in the integration limits. This is normally not so in practice for the finite area of the receiving telescope with aberrations. However, a geometric description of the imaging system suffices when the dimensions we are dealing with such as the image and detector sizes are much larger than the wavelength used, otherwise the integrals have to be simulated for the system.

Fr our system, we use the thin lens equation $\frac{1}{d_1}+\frac{1}{d_2}=\frac{1}{f}$

applied to an object disk area of a. Uniform b. Gaussian illumination from the source.
A very important quantity for the instrument is the field of view of the telescope which is D/f at its maximum which amounts to many degrees. For the reason of limiting sky noise, the field of view is reduced to a much smaller number by restricting the opening to 1 or 2 mm in diameter in a diaphragm placed at the entrance of the box that houses the detector. Let this diameter be d_D, then its field of view is d_D/f where f is the focal length of the telescope.

Each point on the detector receives radiation from a circle of radius r_0 in the target plane, r_0 being the radius of telescope mirror (lens). The image of a point becomes a circle of illumination with radius $r_c=\frac{r_0 f}{R}$ and is radially displaced a distance of

$r_f = \frac{rf}{R}$ from the telescope axis. These two formulas are obtained by applying the lens equation to a distant image from the mirror (lens). This circle of least confusion is given by the intersection of the image plane with the caustic surface which is described by the quadratic equation in one dimension, $\frac{2x^2}{r_0^2\left[1+\sqrt{1-\left(\frac{x}{r_0}\right)^2}\right]}$

A.1.2 Analytical approximations to overlap function

a. Uniform illumination

An illuminated area of disk with radius r at a distance R from the mirror forms an image with radius $w = \frac{f(R\theta_0 + D)}{2(R-f)}$ at a distance $x_i = \frac{Rf}{R-f}$ behind the mirror, where θ_0 is the full angular divergence of the neam. The object and image sizes are related by $w = \frac{r}{R}x_i$ If a represents the detector size, only the fraction $\left(\frac{a}{w}\right)^2$ of the total image area is intercepted by the detector, hence the overlap efficiency is

$$\xi_u(R) = \left[\frac{a(R-f)}{f(R\theta_0 + D)}\right]^2 \tag{A1.13}$$

In the limit $R \to \infty$ and $R\theta_0 \approx D$ at the far range, $\xi_u(R) = \left(\frac{aR}{fR\theta_0}\right)^2$

$$\xi_u(R) = \left(\frac{a}{f\theta_0} \right)^2 = 1 \qquad \text{(A1.14)}$$

since $\theta_0 = \frac{a}{f}$ is the angular field of view of the receiver.

b. Gaussian Illumination

The Gaussian is a radially symmetric distribution whose electric field and intensity variation is given by:

$$E(r) = E_0 \exp\left(-\frac{r^2}{w^2} \right) \qquad I(r) = I_0 \exp\left(-\frac{2r^2}{w^2} \right) \qquad \text{(A1.15)}$$

where w is the beam radius and I_0 is its intensity at the center. The power contained within a radius of the beam is easily integrated to be,

$$P(r) = P(\infty)\left[1 - \exp\left(-\frac{2r^2}{w^2} \right) \right] \qquad \text{(A1.16)}$$

As the beam propagates, its width expands and is analytically given by,

$$w^2(r) = {w_0}^2 \left[1 + \left(\frac{\lambda r}{\pi {w_0}^2} \right)^2 \right] \qquad \text{(A1.17)}$$

As the uniform illumination case shows, the fraction of an image intercepted by the detector is $\xi(R)$ which is also the fraction of the object that is intercepted by the

detector, since the size of an image is related to that of its object by a constant magnification at a particular R. Therefore, the overlap efficiency for Gaussian illumination is,

$$\xi(R) = \frac{1 - \exp\left[-\frac{\xi_u(R) r}{2w^2(R)}\right]}{1 - \exp\left[-\frac{r}{2w^2(R)}\right]} \tag{A1.18}$$

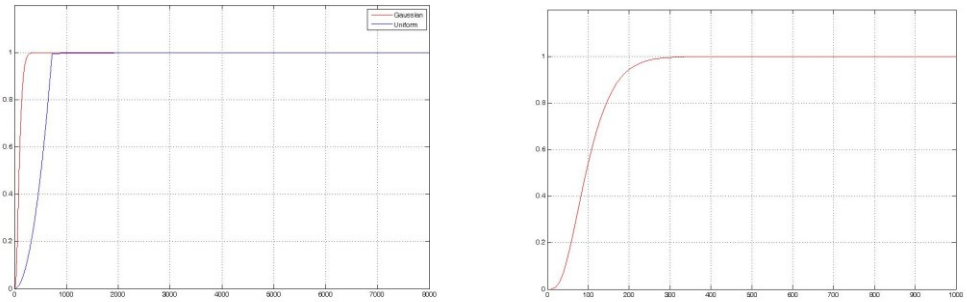

Figure A1.1: Overlap functions evaluated for (a) Uniform (b) Gaussian illumination

In the limit $R \to \infty$, $\xi_u(R) = 1$ and $\xi(R) = 1$ too which is to be expected if any overlap function is correctly computed since at far ranges, all light scattered back to the receiver is collected by the detector.

At the other limit near the receiver, most of the returned power is defocused and falls outside the detector area, hence the efficiency is considerably less than 1. The above formalism has ignored the central obstruction that sits in the return path of light where a specially shaped mirror redirects light to the detector. The reflecting mirror is elliptically shaped to keep the same cross sectional shape of the beam. This geometrically simpler system employs a coaxial configuration where the transmitting laser beam and the

receiver share the same axis. For the biaxial configuration where a separation between these two axes exists, a more careful examination of the geometry has to be done to follow a laser beam that is not visible in the field of view of the telescope below a certain minimum range and after that becomes gradually visible. There has been many papers written on the computation of the biaxial configuration and hardly any on the coaxial as the one we use.

Theoretical calculation of $\xi(z)$ is of course possible when the specification and the configuration of the optical elements are known. However, it is difficult to derive an $\xi(z)$ of use because of various factors which are extremely difficult to determine precisely and subject to changes such as light intensity distribution in the laser beam, transmittance of the interference filters dependent upon the incident angle.

It is already difficult to ensure the parallelism even for the simpler coaxial configuration between the transmitting laser beam and the optical axis of the receiving optics or to build the optical system to a predetermined configuration. Halldorsson and Langerholc also showed numerically that the geometrical form factor is very sensitive to misalignment in the optical system. So it is desirable to determine the geometrical form factor $\xi(z)$ by methods other than theoretical ones.

According to Halldorsson and Langerholc 1978 [7], the scattering area in the view of the telescope is given by,

$$A(z) = \left[S(D) - S(b)\right] / w^2(z) \qquad \text{(A1.19)}$$

where D is the telescope diameter b is the obstruction in the mirror plane, then

$$S(\rho) = \frac{1}{\pi}\int_0^{\phi_1 z+\rho} dr^2 A(\phi_1 z, \rho; r)\int_0^{2\pi} \exp - \frac{r^2+\delta^2-2r\delta\cos\theta}{\omega^2(z)} d\theta \qquad \text{(A1.20)}$$

$$= \frac{1}{\pi}\int_0^{\phi_1 z+\rho} dr^2 A(\phi_1 z, \rho; r) \exp\left[-\frac{r^2+\delta^2}{\omega^2(z)}\right] I_0\left[\frac{2r\delta}{\omega^2(z)}\right] \qquad \text{(A1.21)}$$

(I_0 is a standard Bessel function)

where ϕ_1 is the angular FOV of the mirror, ρ is the image radius at the lens, r is the radial distance of object.

With axial separation δ, $\qquad \delta(z) = \sqrt{(\delta+\phi_{\|}z)^2 + (\phi_{\perp}z)^2}$ (A1.22)

For our coaxial configuration $\delta = 0$, $\delta(z) = \sqrt{\phi_{\|}z)^2 + (\phi_{\perp}z)^2} = z\Delta\phi$ (A1.23)

Making the variable substitution $r = \phi z$ in the integral expression for $S(\rho)$ and inserting

$$\lim_{z\to\infty} A(\phi_1 z, \rho; \phi z) = \pi\rho^2\theta(\phi_1 - \phi) \qquad \text{(A1.24)}$$

where θ is the Heaviside (step) function.

$$\lim_{z\to\infty}\frac{S(\rho)}{\omega^2(z)} = \pi\rho^2\int_{\phi=0}^{\phi_1} \exp\left[-\frac{\phi^2+(\Delta\phi)^2}{\phi_0{}^2}\right] I_0\left(\frac{2\phi\Delta\phi}{\phi_0{}^2}\right) d\left(\frac{\phi}{\phi_0}\right)^2 \qquad \text{(A1.25)}$$

$$A(\infty) = A_{tel}\exp\left[-\left(\frac{\Delta\phi}{\phi_0}\right)^2\right]\int_{x=0}^{\phi_1/\phi_0}\exp(-x^2) I_0\left(\frac{x\Delta\phi}{\phi_0}\right) dx^2 \qquad \text{(A1.26)}$$

where the uncorrected receiver area $A_{tel} \equiv \pi(R^2 - b^2)$ (A1.27)

With perfect alignment, $A(\infty; \Delta\phi = 0) = A_{tel}\left[1 - \exp\left(-\frac{\phi_1}{\phi_0}\right)^2\right]$ (A1.28)

This has the same exponential form as the expression derived above (A1.19) from a much simpler consideration for the Gaussian illumination using geometric optics.

A.1.2 Numerical method to overlap function

A practical approach to determine the overlap function based on measured data was derived by Sasano [4]. In this method, a homogenous and clear atmosphere was assumed. A more realistic method by Ignatenko [5] assumes a moderately turbid atmosphere which is treated as statistically homogeneous if a large number of lidar return signals are averaged. The slope method is first applied to the data over the ranges where the overlap is essentially unity to obtain the extinction coefficient. It is then used in the lidar equation also for the range below unity overlap.

$$\ln\left[\xi(z)\right] = 2\bar{\alpha}(z - z') + \ln\left[\overline{P(z)z^2}\right] - \ln\left[\overline{P(z')z'^2}\right] \qquad \text{(A1.29)}$$

where the overscores denote averages and $\xi(z') = 1$

Simulations using this technique are done for three different wavelengths.

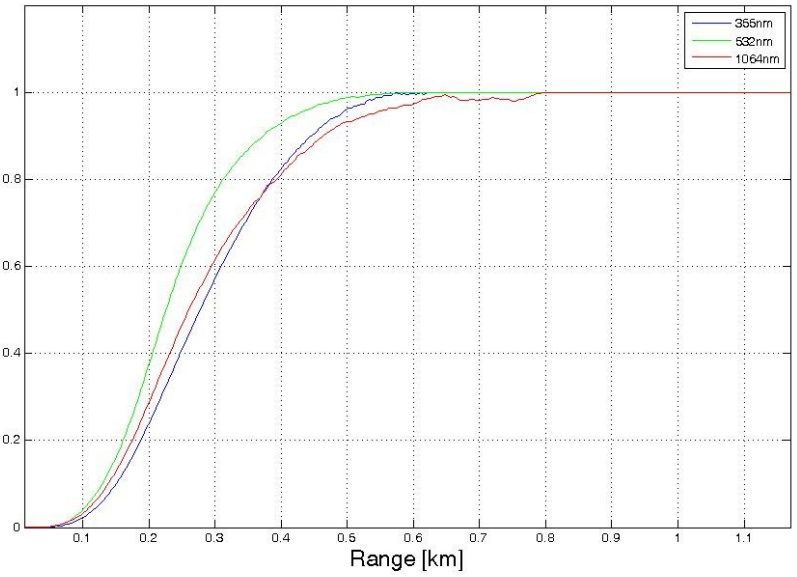

Figure A1.2: Empirical approach to evaluation of the overlap region

The analytical approach is also plotted for the same wavelengths.

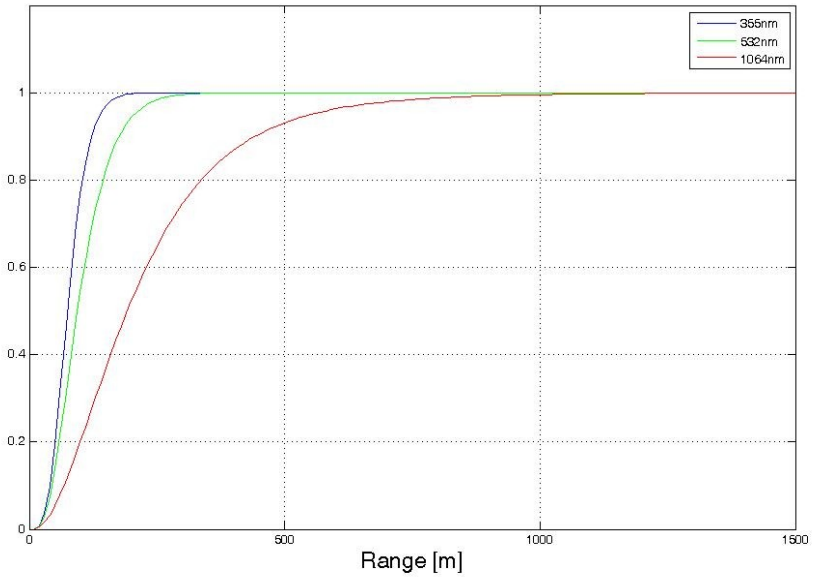

Figure A1.3: Analytical approach to the overlap function

A.1.3 Determination of overlap function by another instrument

Lidar return in the overlap region can be compared with that from the ceilometer that has a negligible overlap zone. The ceilometer is calibrated at 915nm, close to the 1064nm channel so that the whole attenuated backscatter profile practically from the surface up can be used in the lidar equation to calibrate the lidar return. Once th calibration constant is determined and the attenuated backscatter is known, the overlap function follows.

Shown are the range scaled lidar return and ceilometer return scaled by the lidar calibration constant beyond the overlap zone. Ceilometer data is very noisy so the returns are heavily smoothed for comparison.

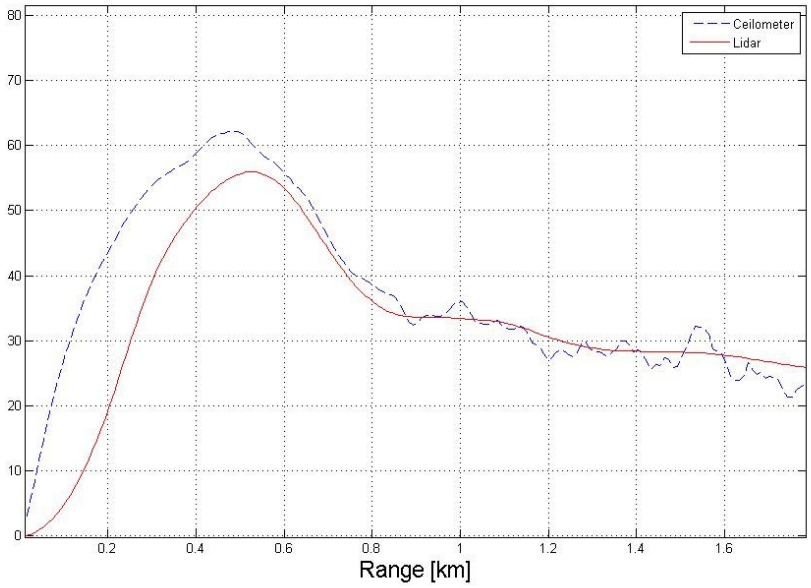

Figure A1.4: Smoothed lidar and ceilometer profiles.

Shown is the overlap efficiency determined by a comparison of the ceilometer return with the lidar return at 1064nm. It is noticed that the efficiency function approaches unity around 900 meters, in close agreement with the empirical and analytical curves shown previously, Figure (A1.2, A1.3). The ceilometer data above 1.5 km is too noisy to use to demonstrate the overlap function acquires a unity value beyond the overlap region.

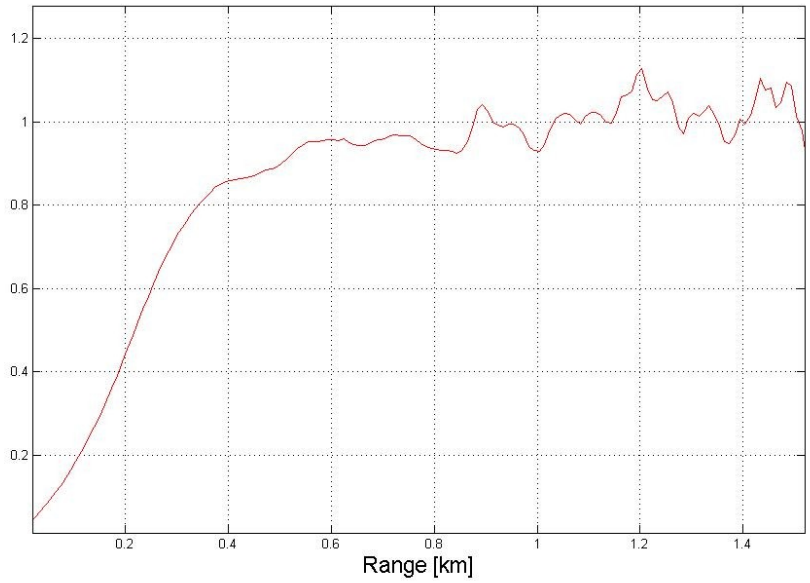

Figure A1.5: Overlap efficiency below 1.5 km

It can be seen that the longest wavelength channel has the longest incomplete overlap range while the shortest wavelength has the shortest overlap range. This is easily understood because the longer the wavelength, the larger the beam waist and hence the least intercepted by the same detector area for a shorter wavelength channel. However, this behavior is complicated by impure laser modes other than the Gaussian fundamental, alignment of the laser beam with each of its three wavelength channels independently adjusted so that the received signal may be misaligned to different degrees, not necessary in proportion to the Gaussian beam widths. Besides, the detectors are not placed at identical locations in relation to the focal plane and the obscuring effect of the secondary mirror at the center is not considered in our simple analytical model above. Over all, the overlap function is a complicated function of the geometry and optical properties such as the transmission and reflectivity of the lenses and mirrors, and electronic performance of the data acquisition unit such as amplification and noise, an absolute determination of the overlap function is quite difficult and the parameters needed to be measured accurately in order to determine the overlap function are numerous. After all, depending on the stability of the system such as the transmitting power, the overlap function fluctuates with it and is not a practical matter to rely on it for corrections. A more practical way to infer data in the incomplete overlap range would be the use of another instrument that has a much shorted incomplete overlap range as the case is with the ceilometer.

A.2 Error arisen from using the same lidar ratio in cloud

Consider the Fernald solution for the backscatter coefficients,

$$\beta_P(z) = \frac{P(z)z^2 \exp\left[-2\left(S_R - S\right)\int_z^{z_c} \beta_R(z')dz'\right]}{\frac{P(z_c){z_c}^2}{\beta_R(z_c)\left[1+\frac{\beta_P(z_c)}{\beta_R(z_c)}\right]} + 2S\int_z^{z_c} P(z)z^2 \exp\left[-2\left(S_R - S\right)\int_z^{z_c} \beta_R(z')dz'\right]dz} - \beta_R(z) \tag{A2.1}$$

Define the normalized total extinction coefficient,

$$y = \alpha^{aer}(z) + \frac{S(z)}{S^{mol}}\alpha^{mol}(z) \tag{A2.2}$$

which is the total backscatter multiplied by the aerosol lidar ratio S,

$$y = S\left(\beta^{aer} + \beta^{mol}\right) \tag{A2.3}$$

Defining the relevant parameters normalized by their respective true values,

$$\sigma = \frac{S}{\hat{S}} \qquad \xi = \frac{X}{\hat{X}} \qquad \eta = \frac{y}{\hat{y}} \qquad \delta = \frac{\alpha^{mol}}{\hat{\alpha}^{mol}} \tag{A2.4}$$

where $X = P(z)z^2$, the range scaled power.

The true value of X and α^{mol} may be different from the measured values and there may be a discrepancy of the model atmosphere from the real one, hence the need to consider their true values.

Inserting these quantities into the lidar equation and differentiate, then solve the resulting differential equation to give [6],

$$\eta(z) =$$

$$\exp\left[-2\int_{z_c}^{z}\left\{\hat{y}(z) + \left[\sigma(z)\delta(z) - 1\right]\frac{\hat{S}(z)}{S^{mol}}\hat{\alpha}^{mol}(z) - \left[\delta(z) - 1\right]\hat{\alpha}^{mol}(z)\right\}dz\right]\sigma(z)\xi(z)/\left(\sigma(z_c)\xi(z_c)\right) \tag{A2.5}$$

$$= \frac{\exp\left[-2\int_{z_c}^{z}\left\{\hat{y}(z)+\left[\sigma(z)\delta(z)-1\right]\frac{\hat{S}(z)}{S^{mol}}\hat{\alpha}^{mol}(z)-\left[\delta(z)-1\right]\hat{\alpha}^{mol}(z)\right\}dz\right]\sigma(z)\xi(z)/\left(\sigma(z_c)\xi(z_c)\right)}{\frac{1}{\eta(z_c)}-2\int_{z_c}^{z}\hat{y}(z)\exp\left[-2\int_{z_c}^{z}\left\{\hat{y}(z')+\left[\sigma(z')\delta(z')-1\right]\frac{\hat{S}(z')}{S^{mol}}\hat{\alpha}^{mol}(z')-\left[\delta(z')-1\right]\hat{\alpha}^{mol}(z')\right\}dz'\right]....} \quad \text{(A2.6)}$$

$$....\left]\sigma(z)\xi(z)/\left(\sigma(z_c)\xi(z_c)\right)dz\right.$$

In order to gain insights into the effect of aerosol lidar constant on the retrieved extinction coefficients from this precise expression, an approximation of a thin atmosphere is made, ie. low optical depth and the integral terms can be ignored to give,

$$\eta(z)=\eta(z_c)\frac{\sigma(z)}{\sigma(z_c)} \quad \text{(A2.6)}$$

Explicitly,

$$\frac{\alpha^{aer}(z)+\frac{S(z)}{S^{mol}}\alpha^{mol}(z)}{\hat{\alpha}^{aer}(z)+\frac{\hat{S}(z)}{S^{mol}}\hat{\alpha}^{mol}(z)}=\frac{\alpha^{mol}(z_c)+\frac{S(z_c)}{S^{mol}}\alpha^{mol}(z_c)}{\hat{\alpha}^{mol}(z_c)+\frac{\hat{S}(z_c)}{S^{mol}}\hat{\alpha}^{mol}(z_c)}\times\frac{S(z)\hat{S}(z_c)}{\hat{S}(z)S(z_c)} \quad \text{(A2.7)}$$

Assuming a small molecular extinction, this is particularly true in the aerosol loaded region below the PBL or clouds,

$$\frac{\alpha^{aer}(z)}{\hat{\alpha}^{aer}(z)}=\frac{\alpha^{aer}(z_c)}{\hat{\alpha}^{aer}(z_c)}\frac{S(z)\hat{S}(z_c)}{\hat{S}(z)S(z_c)} \quad \text{(A2.8)}$$

With this simplified form of the expression, it can be readily seen what happens to the retrieved coefficient $\alpha^{aer}(z)$ if a constant lidar ratio $S(z)$ other than the true variable value $\hat{S}(z)$ is used, the calculated aerosol extinction (and also backscatter) coefficient is inversely proportional to the true value,

$$\alpha^{aer}(z)=\frac{1}{\hat{S}(z)} \quad \text{(A2.9)}$$

Below is the result of model simulation to show this effect of using a single value of lidar ratio in two different layers that have different tru values. The higher extinction coefficient indicates a low cloud layer above an aerosol layer with lower extinction coefficient, the input step function profile. The lidar signals are constructed according to the lidar equation with a typical molecular profile. It is seen from the reconstructed profile of the coefficients to be deviated from the input profile as predicted by the inverse relationship given above. The true values used to construct the signals were 50 for the aerosol and 18 for the cloud layers. The reconstructed coefficients are too low and indeed becoming negative for the aerosol layer with a higher true value. On the contrary, the coefficients are too high for the cloud layer having a true lower value, precisely in a inverse proportion relationship.

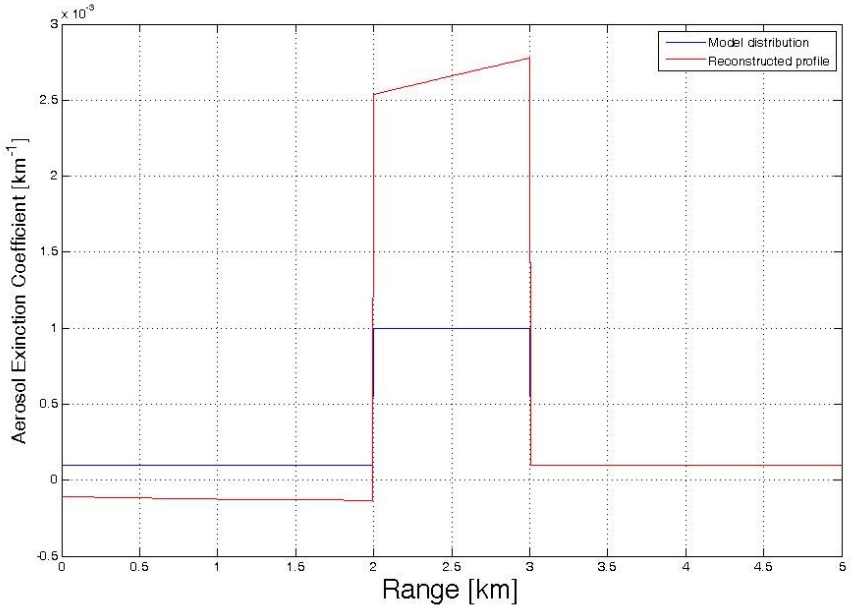

Figure A2.1: Simulated extinction profiles with the same and a different lidar ratio in cloud

This is depicted by the red reconstructed profile, which is the lower profile below 2km and upper profile above 2km. When a constant lidar ratio is used for both aerosol and cloud, the retrieved coefficients are thus too low and give the effect of a dark shadow below the cloud. It may first appear to be some atmospheric phenomena that take place at the edge of a cloud such as entrainment of aerosols into the cloud. However, it has been clearly shown to be a mathematical artifact.

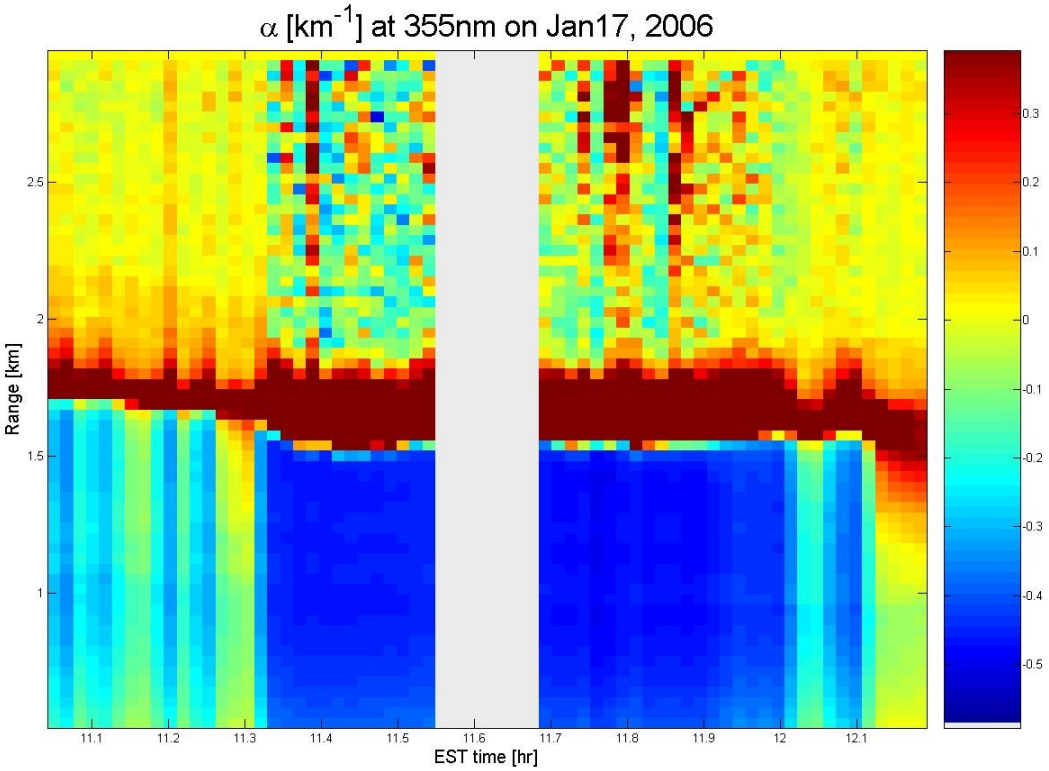

Figure A2.2: Image of the extinction coefficients calculated with the same lidar ratio in cloud

A.3 Derivation of Fernald equation

Consider the first order differential equation,

$$\frac{dy}{dx} + yP(x) = Q(x) \tag{A3.1}$$

Its solution can be obtained by the integration factor: $\exp\left[-\int_{x}^{x_0} P(x')dx'\right]$

Next, the lidar equation: $P(z) = C\,z^{-2}\beta(z)T^2(z)$ (A3.2)

where $T^2(z) = \exp\left[-2\int_0^z \sigma(z)dz\right] = \exp\left[-2S\int_0^z \beta(z)dz\right]$

$$\beta(z) = \frac{-1}{2ST^2(z)}\frac{dT^2(z)}{dz} \tag{A3.3}$$

For both Rayleigh (subscript R) and Mie (subscript P) scatterers,

$$P(z) = C\,z^{-2}\left[\beta_R(z) + \beta_P(z)\right]T_R{}^2(z)T_P{}^2(z) \tag{A3.4}$$

$$T_R{}^2(z) = \exp\left[-2\left(\frac{8\pi}{3}\right)\int_0^z \beta_R(z)dz\right] \tag{A3.5}$$

$$T_P{}^2(z) = \exp\left[-2S\int_0^z \beta_P(z)dz\right] \tag{A3.6}$$

Substituting the above expression (3) for $\beta_P(z)$ into the lidar equation (4),

$$P(z) = Cz^{-2}\left[\beta_R(z) - \frac{1}{2ST_P{}^2(z)}\frac{dT_P{}^2(z)}{dz}\right]T_R{}^2(z)T_P{}^2(z) \tag{A3.7}$$

Rearrange,

$$\frac{dT_P^{\,2}(z)}{dz} - 2S\beta_R(z)T_P^{\,2}(z) = -\frac{2SP(z)z^2}{CT^2{}_R(z)} \tag{A3.8}$$

Identify $-2S\beta_R(z)$ as $P(x)$ and $-\frac{2SP(z)z^2}{CT^2{}_R(z)}$ as $Q(x)$,

The integration factor is: $\exp\left[-2S\int_0^z \beta_R(z)dz\right]$

Multiply the differential equation (8) by the integration factor and integrate from 0 to z,

$$-T_P^{\,2}(0) + T_P^{\,2}(z)\exp\left[-2S\int_0^z \beta_R(z')dz'\right] = -\frac{2S}{C}\int_0^z \frac{P(z)z^2}{T_R^{\,2}(z)}\exp\left[-2S\int_0^z \beta_R(z')dz'\right]dz \tag{A3.9}$$

Rearrange,

$$T_P^{\,2}(z) = \exp\left[2S\int_0^z \beta_R(z')dz'\right]\left\{1 - \frac{2S}{C}\int_0^z \frac{P(z)z^2}{T_R^{\,2}(z)}\exp\left[-2S\int_0^z \beta_R(z')dz'\right]dz\right\} \tag{A3.10}$$

From the 2 components Lidar equation (4),

$$\beta_P(z) = \frac{P(z)z^2}{C}T_R^{\,-2}(z)T_P^{\,-2}(z) - \beta_R(z) \tag{A3.4a}$$

Substitute (A3.10) into (A3.4a)

$$\beta_P(z) = \frac{P(z)z^2}{C}\exp\left[2\left(\frac{8\pi}{3}\right)\int_0^z \beta_R(z')dz'\right]\exp\left[-2S\int_0^z \beta_R(z')dz'\right] \times\left\{1-\frac{2S}{C}\int_0^z \frac{P(z)z^2}{T_R{}^2(z)}\exp\left[-2S\int_0^z \beta_R(z')dz'\right]dz\right\}^{-1} - \beta_R(z) \quad \text{(A3.11)}$$

Identify $S_R = 8\pi/3$,

$$\beta_P(z) = \frac{P(z)z^2}{C}\exp\left[2\left(S_R - S\right)\int_0^z \beta_R(z')dz'\right] \times\left\{1-\frac{2S}{C}\int_0^z \frac{P(z)z^2}{T_R{}^2(z)}\exp\left[-2S\int_0^z \beta_R(z')dz'\right]dz\right\}^{-1} - \beta_R(z) \quad \text{(A3.12)}$$

Substitute $T_R^{-2}(z)$ by (5) into (12), (A3.13)

$$\beta_P(z) = \frac{P(z)z^2}{C}\exp\left[2\left(S_R - S\right)\int_0^z \beta_R(z')dz'\right] \times\left\{1-\frac{2S}{C}\int_0^z P(z)z^2\exp\left[2S_R\int_0^z \beta_R(z')dz'\right]\exp\left[-2S\int_0^z \beta_R(z')dz'\right]dz\right\}^{-1} - \beta_R(z)$$

Combining the exponential terms,

$$\beta_P(z) = \frac{P(z)z^2}{C}\exp\left[2\left(S_R - S\right)\int_0^z \beta_R(z')dz'\right] \times\left\{1-\frac{2S}{C}\int_0^z P(z)z^2\exp\left[2\left(S_R - S\right)\int_0^z \beta_R(z')dz'\right]dz\right\}^{-1} - \beta_R(z) \quad \text{(A3.14)}$$

$$\beta_P(z) = \frac{P(z)z^2 \exp\left[2\left(S_R - S\right)\int_0^z \beta_R(z')dz'\right]}{C - 2S\int_0^z P(z)z^2 \exp\left[2\left(S_R - S\right)\int_0^z \beta_R(z')dz'\right]dz} - \beta_R(z) \quad \text{(A3.15)}$$

Following exactly the same procedure as above for an integration carried out from z to a reference height at the far end z_c, the Fernald solution is arrived:

$$\beta_P(z) = \frac{P(z)z^2 \exp\left[-2\left(S_R - S\right)\int_z^{z_c} \beta_R(z')dz'\right]}{\frac{P(z_c){z_c}^2}{\beta_R(z_c) + \beta_P(z_c)} + 2S\int_z^{z_c} P(z)z^2 \exp\left[-2\left(S_R - S\right)\int_z^{z_c} \beta_R(z')dz'\right]dz} - \beta_R(z) \quad \text{(A3.16)}$$

REFERENCES

[1] A.K.Ghatak and K. Thyagarajan, "Contemporary optics.",*Plenum Press*, 1980

[2] Edwin W. Eloranta, "Thesis: Calculation of Doubly scattered Lidar Returns." University of Wisconsin, 1972.

[3] Edwin W. Eloranta, "Practical model for the calculation of multiply scattered lidar returns.", *Applied Optics*, Vol. 37, No. 12, 2464-2472, 1998

[4] Y. Sasano, H. Shimizu, N. Takeuchi, and M. Okuda,"Geometrical form factor in the laser radar equation: an experimental determination.", *Applied Optics*, Vol. 18, No. 23, pp3908-3910, 1979

[5] V. Kovalev et.al, "Elastic Lidar, Theory, practice, and analyses methods*",* John Wiley and sons, New Jersey USA, pp85, 2004

[6] Yasuhiro Sasano, Edward V. Browell, and Syed Ismail,"Error caused by using a constant extinction/backscattering ratio in the lidar solution.", *Applied Optics*, Vol. 24, No. 22, pp3929-3932, 1985

[7] T. Halldorsson and J. Langerhoic,"Geometrical form factors for the lidar function.", *Applied Optics*, Vol. 17, No. 2, pp240-244, 1978